

Calibrated Multi-Level Quantile Forecasting

Tiffany Ding, Isaac Gibbs, Ryan J. Tibshirani

University of California, Berkeley

Abstract

We present an online method for guaranteeing calibration of quantile forecasts at multiple quantile levels simultaneously. A sequence of α -level quantile forecasts is *calibrated* if the forecasts are larger than the target value at an α -fraction of time steps. We introduce a lightweight method called Multi-Level Quantile Tracker (MultiQT) that wraps around any existing point or quantile forecaster to produce corrected forecasts guaranteed to achieve calibration, even against adversarial distribution shifts, while ensuring that the forecasts are ordered — e.g., the 0.5-level quantile forecast is never larger than the 0.6-level forecast. Furthermore, the method comes with a no-regret guarantee that implies it will not worsen the performance of an existing forecaster, asymptotically, with respect to the quantile loss. In experiments, we find that MultiQT significantly improves the calibration of real forecasters in epidemic and energy forecasting problems.

1 Introduction

Probabilistic forecasts are often conveyed via quantiles. An α -level quantile forecast attempts to predict the value below which an outcome y_t falls with probability α . Consider a forecaster who, at each time t , outputs a vector of quantile forecasts

$$q_t = [q_t^{\alpha_1}, q_t^{\alpha_2}, \dots, q_t^{\alpha_{|\mathcal{A}|}}]$$

for quantile levels $\mathcal{A} = \{\alpha_1, \alpha_2, \dots, \alpha_{|\mathcal{A}|}\}$, where $0 < \alpha_1 < \alpha_2 < \dots < \alpha_{|\mathcal{A}|}$. Such forecasts inform decision-making in a wide range of applications, including public health (Doms et al., 2018; Lutz et al., 2019), inventory management (Cao and Shen, 2019), and energy grid operation (Hong and Fan, 2016). When decisions are made on the basis of forecasts that are *calibrated*, this can lead to a reliability guarantee. For example, if a retailer orders inventory based on a sequence of calibrated 0.95-level quantile forecasts of weekly demand, this guarantees that they run out of stock at most 5% of weeks.

Although a single ($|\mathcal{A}| = 1$) quantile is sometimes sufficient for decision-making, this is not true in general. When there are multiple downstream users, each with different risk tolerances and uses for the forecasts, it is necessary to provide forecasts at multiple ($|\mathcal{A}| \geq 2$) quantile levels. In this work, we seek to produce multi-level quantile forecasts that satisfy the following two useful properties:

1. (*Distribution-free*) *calibration*: Against any, possibly adversarial, sequence of true values y_1, y_2, \dots , the long-run empirical coverage of the level- α quantile forecasts approaches α — that is, defining $\text{cov}_t^\alpha = \mathbb{1}\{y_t \leq q_t^\alpha\}$, we want

$$\lim_{T \rightarrow \infty} \frac{1}{T} \sum_{t=1}^T \text{cov}_t^\alpha = \alpha \quad \text{for all } \alpha \in \mathcal{A}. \quad (1)$$

This property guarantees coherence between forecasts and realized values, even when the distribution of y_t changes over time.

2. *Distributional consistency (no crossings).* Forecasts should also be *ordered* across quantile levels:

$$q_t^{\alpha_1} \leq q_t^{\alpha_2} \leq \cdots \leq q_t^{\alpha_{|\mathcal{A}|}} \quad \text{for all } t. \quad (2)$$

Without this ordering, the vector of forecasts would not correspond to a valid probability distribution, making it difficult for decision makers to interpret or trust.

There are many methods for producing quantile forecasts, including classical time-series models such as ARIMA and exponential smoothing, as well as modern machine learning approaches such as random forests, and deep neural networks. However, these forecasts often fail to satisfy calibration. Our aim is to take any existing forecaster and transform its predictions *online* (in real time) so that the resulting forecasts satisfy both (1) and (2) for any sequence of outcomes. We refer to this joint goal as **calibration without crossings**. Furthermore, subject to calibration without crossings, we want the forecasts to remain *sharp* — all else equal, for two levels $\alpha \neq \beta$, it is more informative if q_t^α and q_t^β are closer together.

Our first objective, online calibration, has been studied extensively for the single quantile case ($|\mathcal{A}| = 1$) in the context of online conformal prediction, introduced by [Gibbs and Candès \(2021\)](#). Online conformal prediction methods are guaranteed to achieve the distribution-free calibration objective described in (1). Of particular relevance to our work is the Quantile Tracker algorithm from [Angelopoulos et al. \(2023\)](#). The idea behind this procedure is simple: To track the α -quantile over time, we should increase our current guess if it is smaller than y_t (it “*miscalculates*”) and we should decrease our current guess if it is larger than y_t (it “*covers*”). The amount by which we increase or decrease is chosen to yield a long-run coverage of α . Running the Quantile Tracker is guaranteed to achieve long-run coverage as long as y_t has bounded magnitude. Unfortunately, applying the Quantile Tracker to multiple quantile levels simultaneously often results in quantile crossings, violating (2).¹

To solve the problem of simultaneously calibrating multiple quantiles without crossings, we propose a simple procedure called *Multiple Quantile Tracker (MultiQT)* that combines a Quantile-Tracker-like update for each quantile level with an ordering step to ensure that the forecasted quantiles are distributionally consistent. As we later show, naive ways of combining these two components do not achieve distribution-free calibration, but our method provably does.

To prove the calibration guarantee of our procedure, we first connect our goal of calibration with no crossings to a more general problem of *constrained gradient equilibrium*. Many statistical objectives in online settings (including calibration) are special cases of a condition introduced by [Angelopoulos et al. \(2025\)](#) called *gradient equilibrium*, which says that the average gradient of the loss functions evaluated at the chosen iterates converges to zero as t goes to infinity. They show that, to produce iterates that achieve gradient equilibrium, one can simply run online gradient descent, provided that the losses satisfy a certain condition. However, it has been heretofore unknown whether gradient equilibrium can still be achieved if the iterates are restricted to some constraint set, such as in our multi-level quantile forecasting setting, where our forecasts must be in the set of ordered vectors. We provide an affirmative answer by showing that *lazy gradient descent*, which combines online gradient descent with a projection step to satisfy the iterate constraints, provably achieves gradient equilibrium as long as the loss function and constraint set jointly satisfy a condition we call *inward flow*.

¹In experiments on the COVID-19 Forecast Hub dataset from [Cramer et al. \(2022b\)](#), Quantile Tracker produced crossings at 87% of time steps on average (see Appendix A).

We show that the loss function and constraint set for the calibration without crossings problem satisfy inward flow. Thus, MultiQT, which can be written as lazy gradient descent on that loss function and constraint set, inherits a calibration guarantee from our more general analysis of gradient equilibrium with constraints. Finally, we prove a no-regret guarantee in terms of the quantile loss. Due to the decomposition of the quantile loss into calibration and sharpness terms, this result implies that MultiQT achieves calibration without paying a steep price in terms of sharpness.

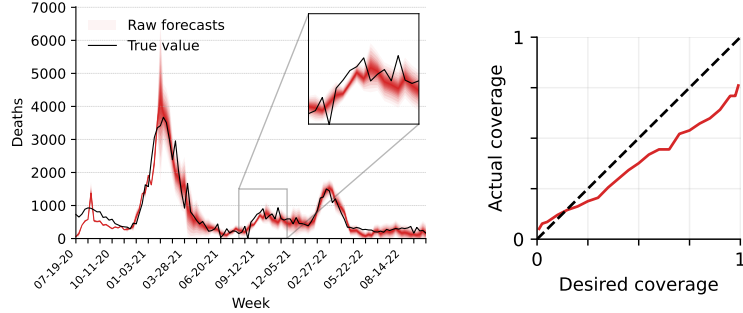
1.1 A peek at results: calibrating COVID-19 forecasts

To illustrate the behavior of our method in practice, we begin with a brief case study. During the COVID-19 pandemic, forecasting teams submitted forecasts each week to the United States COVID-19 Forecast Hub for COVID-19 deaths in each state one, two, three, and four weeks into the future. In Figure 1a, we show one forecasting team’s one-week-ahead forecasts for weekly COVID-19 deaths in California. We observe that these quantile forecasts are too narrow and biased downwards — in other words, they convey more certainty than is appropriate and fail to cover the true death count at the desired rate. Our proposed MultiQT method can be applied in real time to recalibrate such forecasts. Figure 1b shows the results of running MultiQT online (at each time t , using the performance of the forecasts up through time $t - 1$ to correct the next forecast). We observe that MultiQT corrects the downward bias of the upper quantiles and the resulting forecasts achieve close to perfect calibration. By improving the coherence of the forecasts with the eventual death counts, these better calibrated forecasts improve the quality of public communication about the expected trajectory of the pandemic and can even inform public health decisions regarding allocation of scarce resources like masks and hospital staffing (Cramer et al., 2022b). We will return to this COVID-19 forecasting application in Section 5.

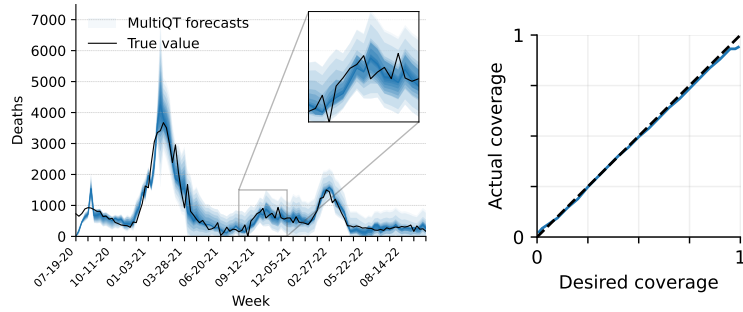
1.2 Related work

Online calibration of a single quantile in the presence of distribution shift has been studied extensively in the context of online conformal prediction, beginning with Gibbs and Candès (2021). The central idea underlying many of these methods is to apply online gradient descent to the quantile loss, either in α -space (Gibbs and Candès, 2021) or in y_t -space (Angelopoulos et al., 2023), where the latter has the advantage of not requiring a quantile computation at each time step. Extensions in this line of work include ways to better set the learning rate (Zaffran et al., 2022; Gibbs and Candès, 2024), losses besides coverage (Feldman et al., 2022; Lekeufack et al., 2024), approaches tailored to multi-horizon forecasting (Yang et al., 2024; Wang and Hyndman, 2024) or otherwise exploit error predictability (Hu et al., 2025), and improving adaptivity by targeting strongly adaptive regret (Bhatnagar et al., 2023; Hajishemmi and Shen, 2024). Gradient equilibrium, proposed in Angelopoulos et al. (2025), generalizes the concept of online calibration beyond the single quantile calibration problem considered in online conformal prediction and provides sufficient conditions for online gradient descent to achieve gradient equilibrium.

A complementary line of calibration methods uses Blackwell approachability and related ideas, resulting in algorithms that are generally more complex than those based on gradient descent but can offer stronger (conditional) guarantees. Blackwell (1956) studies when and how a player can guarantee that their average payoff vector approaches a target convex set in an adversarial game. Blackwell’s approachability theorem shows that it suffices to choose actions that make a certain inner product non-positive. Calibration arises as a special case, where the convex set encodes zero calibration error. These ideas underpin many works on calibration (Foster, 1999; Foster and Hart, 2021) and defensive forecasting (Vovk et al., 2005; Perdomo



(a) Raw forecasts and their calibration.



(b) Forecasts and calibration after applying MultiQT.

Figure 1: One-week-ahead forecasts of weekly COVID-19 deaths in California from July 11, 2020 to October 22, 2022 generated by forecaster `RobertWalraven-ESG` before (top) and after (bottom) applying MultiQT. Forecasts are made at levels 0.01, 0.025, 0.05, 0.1, 0.15, 0.2, 0.25, 0.3, 0.35, 0.4, 0.45, 0.5, 0.55, 0.6, 0.65, 0.7, 0.75, 0.8, 0.85, 0.9, 0.95, 0.975, and 0.99. To visualize these forecasts, we plot colored bands where the lightest opacity connects the 0.01 and 0.99 level forecasts, the next lightest connects the 0.025 and 0.975 level forecasts, and so on.

and Recht, 2025). Using these ideas, Gupta et al. (2022) propose algorithms for group-conditional quantile calibration, which are applied to online conformal prediction in Bastani et al. (2022). These ideas were extended to distributional and vector calibration by Noarov et al. (2023), who give an algorithm for high-dimensional conditional calibration subject to an arbitrary convex constraint set. Although this framework can in principle accommodate calibration without crossings, it lacks a practical implementation for this setting, as it requires solving nontrivial optimization problems at each time step. In contrast, our goal is to provide an easily implementable procedure targeted at the specific problem of calibrating quantile forecasts subject to an order constraint. Also related are Deshpande et al. (2023) and Marx et al. (2024), which use Blackwell approachability to calibrate probabilistic forecasts that specify a distribution over y_t .

Quantile estimation is a problem with a long history, dating back to Koenker and Bassett (1978). It was initially considered only in the offline setting (with no distribution shift), but the problem of quantile crossing was nonetheless present; the problem of ensuring quantile monotonicity when jointly learning multiple quantiles dates back to Bassett Jr and Koenker (1982), and solutions have been proposed in the form of post-processing (Chernozhukov et al., 2010; Fakoor et al., 2023), constrained optimization (Liu and Wu, 2009), or deep learning architectures that enforce monotonicity of the output vector (Gasthaus et al., 2019;

Park et al., 2022), all in the offline setting. In the online setting, Zhang et al. (2024) proposes a method that enforces monotonicity but only achieves a no-regret guarantee and not a calibration guarantee. Li and Rodríguez (2025) makes use of ideas from Angelopoulos et al. (2023) to design a loss function for training the forecaster that targets coverage with no quantile crossings, but in practice their method still produces crossings (at roughly 10% of time steps in their experiments). In comparison, we propose a lightweight method that can wrap around any existing forecaster and is guaranteed to achieve coverage while having no quantile crossings.

Finally, our work relates to a broader literature on forecast recalibration, which considers how to improve the calibration of an existing forecaster (Brocklehurst et al., 1990) or an ensemble of forecasters (Hamill and Colucci, 1997; Raftery et al., 2005; Gneiting and Ranjan, 2013; van den Dool et al., 2017).

2 Method

In this section, we present our online method for generating calibrated, distributionally consistent quantile forecasts given an initially uncalibrated base forecaster. We do so by learning offsets that result in calibrated forecasts when added to the base forecasts. All omitted proofs in this and proceeding sections are deferred to Appendix B unless otherwise stated.

Notation. We use $b_t = [b_t^{\alpha_1}, b_t^{\alpha_2}, \dots, b_t^{\alpha_{|\mathcal{A}|}}]$ to denote the base forecasts at time t , where b_t^α is the base forecast for level α . We use $\theta_t \in \mathbb{R}^{|\mathcal{A}|}$ to denote the offset we are adjusting online and $q_t := b_t + \theta_t$ to denote the corresponding recalibrated forecast at time t . We define $\text{cov}_t^\alpha = \mathbb{1}\{y_t \leq q_t^\alpha\}$ to be the coverage indicator for the α -level forecast. For a closed convex set $C \subseteq \mathbb{R}^d$, we use $\Pi_C(x) = \operatorname{argmin}_{y \in C} \|x - y\|_2^2$ to denote the Euclidean projection of x onto C . Given a vector $v \in \mathbb{R}^d$, the set $C - v = \{x - v : x \in C\}$ is the set C shifted by v . We define $\mathcal{K}^d = \{x \in \mathbb{R}^d : x_1 \leq x_2 \leq \dots \leq x_d\}$ to be the set of d -dimensional vectors with nondecreasing entries, where we will suppress the d subscript when the dimensionality is inferable (in general, $d = |\mathcal{A}|$). We refer to the projection $\Pi_{\mathcal{K}}$ as *isotonic regression*.

Base forecasts. We assume the base forecasts are distributionally consistent, i.e.,

$$b_t^{\alpha_1} \leq b_t^{\alpha_2} \leq \dots \leq b_t^{\alpha_{|\mathcal{A}|}}$$

for all t . These base forecasts can be generated in any way, e.g., $b_t^\alpha = f_t^\alpha(x_t)$ where f_t^α is some (possibly time-varying) predictor trained on past data y_1, \dots, y_{t-1} that optionally incorporates information from features x_t . In problems with no base forecaster, we can set all base forecasts equal to zero ($b_t = \mathbf{0}$). If instead there is a point forecaster that forecasts the mean or median at each time step, we can set all base forecasts at time t to the point forecast k_t at time t ($b_t = [k_t, k_t, \dots, k_t]$).

We begin by presenting some relevant background on the Quantile Tracker method (Section 2.1) that our proposed method builds upon (Section 2.2).

2.1 Background: Quantile Tracker

Given a desired coverage level α , the *Quantile Tracker (QT)* algorithm from Angelopoulos et al. (2023) updates the offsets according to

$$\theta_{t+1}^\alpha = \theta_t^\alpha - \eta(\text{cov}_t^\alpha - \alpha) \tag{3}$$

starting from some initial offset $\theta_1^\alpha \in \mathbb{R}$ and for some learning rate $\eta > 0$, then outputs the forecast $q_t^\alpha = b_t^\alpha + \theta_t^\alpha$. This update rule is intuitive: We increase our forecast by $\eta\alpha$ when we miscover, making it more likely we will cover at the next time step, and decrease by $\eta(1 - \alpha)$ when we cover.

The following result tells us that the Quantile Tracker is guaranteed to achieve long-run coverage as long as the residuals are bounded.

Proposition 1 (Quantile Tracker guarantee from Angelopoulos et al. (2023)). *Suppose there exists $R > 0$ such that $|y_t - b_t^\alpha| \leq R$ for all t . Then the coverage gap of the Quantile Tracker iterates is upper bounded as*

$$\left| \frac{1}{T} \sum_{t=1}^T \text{cov}_t^\alpha - \alpha \right| \leq \frac{2|\theta_1^\alpha| + R + \eta}{\eta T}. \quad (4)$$

However, applying the Quantile Tracker update to multiple quantile levels simultaneously often results in crossed quantiles, which is undesirable. A natural solution to the crossing problem is to run the Quantile Tracker as normal and order the forecasts at each time step before revealing them. Two common ordering mechanisms are sorting and isotonic regression. Formally, given a vector $v \in \mathbb{R}^d$, we define $\text{SORT}(v)$ to be the vector whose i -th entry is the i -th smallest entry of v . Isotonic regression is represented as $\Pi_{\mathcal{K}}$, as defined at the beginning of this section. Unfortunately, the following result says that this post hoc ordering solution fails to achieve distribution-free calibration with either of these ordering mechanisms.

Proposition 2 (Post hoc ordering of Quantile Tracker fails). *For a quantile level α , let q_t^α be the Quantile Tracker iterate obtained using the update rule (3) starting from any initial offset θ_1^α and let $[\hat{q}_t^{\alpha_1}, \hat{q}_t^{\alpha_2}, \dots, \hat{q}_t^{\alpha_{|\mathcal{A}|}}] := m([q_t^{\alpha_1}, q_t^{\alpha_2}, \dots, q_t^{\alpha_{|\mathcal{A}|}}])$ where $m : \mathbb{R}^{|\mathcal{A}|} \rightarrow \mathbb{R}^{|\mathcal{A}|}$ is a mapping that produces a vector with nondecreasing entries. For both $m = \text{SORT}$ and $m = \Pi_{\mathcal{K}}$, there exists a set of levels \mathcal{A} and sequence of (y_t, b_t) with $|y_t - b_t^\alpha| < R$ for all α and t (for some $R > 0$) such that for some quantile level $\alpha \in \mathcal{A}$, we have $\lim_{T \rightarrow \infty} \frac{1}{T} \sum_{t=1}^T \mathbb{1}\{y_t \leq \hat{q}_t^\alpha\} \neq \alpha$.*

The intuition for this result is simple: By Proposition 1, we know that q_t^α , $t = 1, 2, \dots$ is guaranteed to achieve long-run coverage of α . If we replace a non-vanishing fraction of q_t^α 's with some arbitrary value, we would not expect the resulting sequence to still achieve α coverage. This is precisely what happens if crossings happen infinitely often. Whenever a crossing occurs, applying m maps \hat{q}_t^α to a value that is not q_t^α (for $m = \text{SORT}$, \hat{q}_t^α is set to q_t^β for some $\beta \neq \alpha$, and for $m = \Pi_{\mathcal{K}}$, \hat{q}_t^α is set to some pooled value). As a result, the long-run empirical coverage of the \hat{q}_t^α 's differs from that of the q_t^α 's. Based on this intuition, we construct a formal counterexample where long-run coverage is violated in Appendix C.

2.2 Multi-Level Quantile Tracker (MultiQT)

The method we propose is simple but, as we will later show, has compelling theoretical guarantees and strong empirical performance. At a high level, our method maintains two vectors of offsets: one hidden and one played. The hidden offsets do not necessarily result in ordered forecasts when added to the base forecasts, but the played offsets do. We will use $\tilde{\theta}_t = [\tilde{\theta}_t^{\alpha_1}, \tilde{\theta}_t^{\alpha_2}, \dots, \tilde{\theta}_t^{\alpha_{|\mathcal{A}|}}]$ to denote the hidden offsets that our method maintains internally.

Procedure 1 (Multi-Level Quantile Tracker (MultiQT)). Choose learning rate $\eta > 0$ and initial value $\tilde{\theta}_1 \in \mathcal{K}$ for the hidden offset. For $t = 1, 2, \dots$,

1. Compute the played offset $\theta_t = \Pi_{\mathcal{K}-b_t}(\tilde{\theta}_t)$.
2. Play forecast $q_t = b_t + \theta_t$.
3. Update the hidden offset: For each quantile level $\alpha \in \mathcal{A}$,

$$\tilde{\theta}_{t+1}^\alpha = \tilde{\theta}_t^\alpha - \eta(\text{cov}_t^\alpha - \alpha). \quad (5)$$

Note that Steps 1 and 2 can be combined into a single step:

$$q_t = \Pi_{\mathcal{K}}(b_t + \tilde{\theta}_t). \quad (6)$$

This is equivalent to the two-step procedure because $\Pi_C(x + b) = b + \Pi_{C-b}(x)$ for any closed convex set $C \subseteq \mathbb{R}^d$ and vectors $x, b \in \mathbb{R}^d$ (see Appendix B.4 for a proof of this fact). Writing the MultiQT forecast q_t in this way makes it clear it belongs to \mathcal{K} and is thus distributionally consistent. When running MultiQT in practice, we compute q_t using (6); this isotonic regression can be computed efficiently in $O(|\mathcal{A}|)$ time via the Pool Adjacent Violators Algorithm (PAVA) (Ayer et al., 1955; Barlow et al., 1972).

We highlight that in (5), the hidden offsets are updated based on the coverage induced by the played offset: What appears in this update is $\text{cov}_t^\alpha = \mathbb{1}\{y_t \leq b_t^\alpha + \theta_t^\alpha\}$ rather than $\mathbb{1}\{y_t \leq b_t^\alpha + \tilde{\theta}_t^\alpha\}$. Described more abstractly, the update is a gradient step starting from the hidden offset but using the gradient evaluated at the played offset. As we will later see, this combination turns out to be crucial for achieving the desired calibration guarantee.

MultiQT with delayed feedback or lead time. Procedure 1 assumes that at each time t , we are able to observe y_t before making our forecast for time $t + 1$, but there are many settings where this is not the case. This can happen if there is *delayed feedback*, where feedback is observed with some constant delay $D \geq 0$, meaning that the true value at time t is not observed until after the forecast is made at time $t + D$. Equivalently (from the perspective of our method), we may be asked to make forecasts with a *lead time* of $D + 1$. In such settings, feedback for time t is not observed until after we make our forecasts at time $t + 1, t + 2, \dots, t + D$. A lead time of one ($D = 0$) corresponds to the standard MultiQT setting, but $D \geq 1$ can be viewed as a delayed feedback problem. In such situations, we can run a delayed feedback version of MultiQT, which looks exactly like Procedure 1 except the hidden offset update in (5) is replaced with

$$\tilde{\theta}_{t+1}^\alpha = \tilde{\theta}_t^\alpha - \eta(\text{cov}_{t-D}^\alpha - \alpha) \quad (7)$$

for $t > D$ and $\tilde{\theta}_{t+1}^\alpha = \tilde{\theta}_t^\alpha$ for $t \leq D$. Equivalently, at time t , we update the hidden offset with the feedback that is observed at time t , except for the first D time steps where no feedback is observed. Compared to the original MultiQT update, the only difference is that the coverage indicator is the one for the time $t - D$ forecast rather than time t .

3 Constrained Gradient Equilibrium

To show that MultiQT solves the problem of calibration without crossings, we first solve a more general problem we call *constrained gradient equilibrium* and then show that MultiQT is the instantiation of this

general solution for our problem (Figure 2). Thinking about our problem at the more general level gives us a useful framework for cleanly proving the desired calibration guarantee.

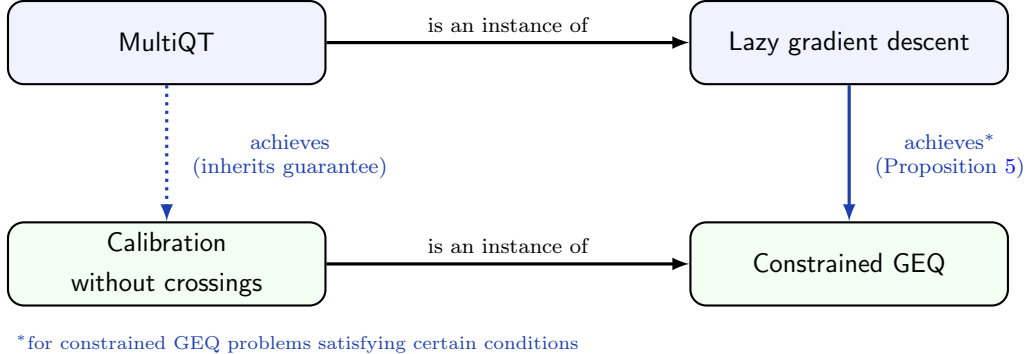


Figure 2: To prove that MultiQT achieves calibration without crossings, we will first show that lazy gradient descent achieves constrained gradient equilibrium (constrained GEQ). MultiQT then inherits the desired guarantee.

We begin by defining gradient equilibrium and its constrained variant and then show that the latter encompasses calibration without crossings.

Definition 1 (Angelopoulos et al. (2025)). A sequence of iterates $\theta_t \in \mathbb{R}^d$, $t = 1, 2, \dots$ satisfies *gradient equilibrium (GEQ)* with respect to a sequence of loss functions $\ell_t : \mathbb{R}^d \rightarrow \mathbb{R}$, $t = 1, 2, \dots$ if

$$\lim_{T \rightarrow \infty} \frac{1}{T} \sum_{t=1}^T g_t(\theta_t) = \mathbf{0}, \quad (8)$$

where g_t is the gradient² of ℓ_t for $t = 1, 2, \dots$ and $\mathbf{0}$ is the d -dimensional zero vector.

However, there are many settings in which the iterates are restricted to (time-varying) constraint sets. This gives rise to the following problem definition.

Definition 2. A sequence of iterates $\theta_t \in \mathbb{R}^d$, $t = 1, 2, \dots$ satisfies *constrained gradient equilibrium (constrained GEQ)* with respect to a sequence of loss functions $\ell_t : \mathbb{R}^d \rightarrow \mathbb{R}$, $t = 1, 2, \dots$ and constraint sets $C_t \subseteq \mathbb{R}^d$, $t = 1, 2, \dots$ if

- (a) $\theta_t \in \mathbb{R}^d$, $t = 1, 2, \dots$ satisfies gradient equilibrium with respect to $\ell_t : \mathbb{R}^d \rightarrow \mathbb{R}$, $t = 1, 2, \dots$ (Definition 1), and
- (b) $\theta_t \in C_t$ for $t = 1, 2, \dots$

Calibration without crossings as constrained GEQ. We observe that our goal of calibration without crossings is an instance of constrained gradient equilibrium. For $\alpha \in [0, 1]$, let $\rho_\alpha : \mathbb{R} \times \mathbb{R} \rightarrow \mathbb{R}$ be the α -level quantile loss, where

$$\rho_\alpha(\hat{y}, y) = \begin{cases} \alpha|y - \hat{y}| & \text{if } y - \hat{y} \geq 0 \\ (1 - \alpha)|y - \hat{y}| & \text{otherwise.} \end{cases} \quad (9)$$

²If ℓ_t is subdifferentiable but not differentiable, we can modify this definition. Given a sequence of subdifferentiable loss functions, let g_t , $t = 1, 2, \dots$ be some sequence of subgradients of these losses. A sequence of iterates $\theta_t \in \mathbb{R}^d$, $t = 1, 2, \dots$ satisfies *gradient equilibrium (GEQ)* with respect to the specified sequence of subgradients if (8) is satisfied.

Given a set of levels \mathcal{A} and vector of forecasts $q_t = [q_t^{\alpha_1}, q_t^{\alpha_2}, \dots, q_t^{\alpha_{|\mathcal{A}|}}]$, let $\rho_{\mathcal{A}} : \mathbb{R}^{|\mathcal{A}|} \times \mathbb{R} \rightarrow \mathbb{R}$ be the aggregated quantile loss, where

$$\rho_{\mathcal{A}}(q_t, y) = \sum_{\alpha \in \mathcal{A}} \rho_{\alpha}(q_t^{\alpha}, y). \quad (10)$$

Now consider the loss function on θ_t that applies the aggregated quantile loss to the vector of forecasts $q_t = b_t + \theta_t$ and the observed value y_t :

$$\ell_t(\theta_t) = \rho_{\mathcal{A}}(b_t + \theta_t, y_t) = \sum_{\alpha \in \mathcal{A}} \rho_{\alpha}(b_t^{\alpha} + \theta_t^{\alpha}, y_t). \quad (11)$$

We will call (11) the *MultiQT loss*. A subgradient of the MultiQT loss at θ_t is

$$g_t(\theta_t) = \begin{bmatrix} \text{cov}_t^{\alpha_1} - \alpha_1 \\ \text{cov}_t^{\alpha_2} - \alpha_2 \\ \vdots \\ \text{cov}_t^{\alpha_{|\mathcal{A}|}} - \alpha_{|\mathcal{A}|} \end{bmatrix}^T, \quad (12)$$

where we recall that $\text{cov}_t^{\alpha} := \mathbb{1}\{y_t \leq q_t^{\alpha}\} = \mathbb{1}\{y_t \leq b_t^{\alpha} + \theta_t^{\alpha}\}$. To streamline presentation, we will refer to (12) as simply “the gradient” of the MultiQT loss. We now observe the following equivalence:

$$\lim_{T \rightarrow \infty} \frac{1}{T} \sum_{t=1}^T g_t(\theta_t) = \mathbf{0} \iff \lim_{T \rightarrow \infty} \frac{1}{T} \sum_{t=1}^T \text{cov}_t^{\alpha} = \alpha \text{ for all } \alpha \in \mathcal{A}.$$

In other words, if a sequence of iterates satisfy gradient equilibrium with respect to ℓ_t , $t = 1, 2, \dots$ as defined in (11), then they also satisfy calibration.

However, for our problem it is not enough for the iterates to be calibrated; they must also produce distributionally consistent forecasts once added to the base forecasts. Setting the constraint set at time t as

$$C_t = \mathcal{K} - b_t, \quad (13)$$

which is the isotonic cone shifted by the base forecast b_t , ensures that the resulting forecast q_t does not have crossed quantiles. Thus, calibration without crossings is an instance of constrained GEq for the loss function and constraint set defined above.

3.1 Background: gradient descent

It turns out that we do not need to devise new algorithms in order to produce iterates that satisfy gradient equilibrium. Online gradient descent, a standard algorithm in online learning, can also be used to solve the gradient equilibrium problem.

Gradient descent achieves GEq. Given some initial point $\theta_1 \in \mathbb{R}^d$ and learning rate $\eta > 0$, *online gradient descent* obtains iterates via the update rule

$$\theta_{t+1} = \theta_t - \eta g_t(\theta_t), \quad (14)$$

where g_t is a subgradient of the loss function at time t . As observed in Proposition 2 of [Angelopoulos et al. \(2025\)](#), the average gradient satisfies

$$\frac{1}{T} \sum_{t=1}^T g_t(\theta_t) = \frac{\theta_1 - \theta_{T+1}}{\eta T}. \quad (15)$$

This comes from rearranging (14) to get $g_t(\theta_t) = (\theta_t - \theta_{t+1})/\eta$ and then averaging over t . Since θ_1 is chosen by us, it is bounded. Thus, if we can bound θ_{T+1} , this would imply a bound on the average gradient. [Angelopoulos et al. \(2025\)](#) show that a sufficient condition for θ_{T+1} to be bounded or sublinear in T is for the loss functions to be Lipschitz and restorative at all time steps. Lipschitzness is a standard condition, and we say a loss function is *L-Lipschitz* if all of its subgradients g satisfy $\|g(\theta)\|_2 \leq L$ for all θ . Restorativity is a new condition that they introduce, which we now describe.

Definition 3 (Restorativity, [Angelopoulos et al. \(2025\)](#)). A loss function ℓ is said to be (h, ϕ) -restorative for $h \geq 0$ and non-negative function ϕ if all of its subgradients g satisfy

$$\langle \theta, g(\theta) \rangle \geq \phi(\theta) \quad \text{whenever } \|\theta\|_2 > h. \quad (16)$$

Intuitively, restorativity tells us that whenever the iterates get too far from the origin, the negative gradient will push the iterate back towards the origin. This can be seen most easily in the one-dimensional setting where $\theta \in \mathbb{R}$ and $\phi(\theta) = 0$; in this case, restorativity says that $\langle \theta, g(\theta) \rangle \geq 0$ whenever $|\theta| \geq h$. This implies that whenever θ is large in magnitude, the negative gradient will be anti-aligned with it, so following the negative gradient will decrease the magnitude of θ . This intuition is formalized in the following result, which tells us that online gradient descent produces bounded iterates when the losses are restorative, and consequently achieves gradient equilibrium.

Proposition 3 (Online gradient descent achieves GEQ, Proposition 5 of [Angelopoulos et al. \(2025\)](#)). *Suppose at each time t , the loss function ℓ_t is L -Lipschitz and $(h_t, 0)$ -restorative. Then the online gradient descent iterates produced by (14) satisfy $\|\theta_{T+1}\|_2 \leq \sqrt{\|\theta_1\|_2^2 + \eta^2 L^2 T + 2\eta L \sum_{t=1}^T h_t}$. If h_t is nondecreasing, this implies*

$$\left\| \frac{1}{T} \sum_{t=1}^T g_t(\theta_t) \right\|_2 \leq \frac{2\|\theta_1\|_2}{\eta T} + \sqrt{\frac{L^2}{T} + \frac{2Lh_T}{\eta T}}, \quad (17)$$

which goes to zero as $T \rightarrow \infty$ as long as h_t is sublinear.

Note that the Quantile Tracker algorithm (Section 2.1) is simply online gradient descent with respect to the loss $\ell_t(\theta) = \rho_\alpha(b_t^\alpha + \theta, y_t)$. The gradient of this loss can be expressed as $\text{cov}_t^\alpha - \alpha$, and plugging this into (14) exactly recovers the Quantile Tracker update from (3). The calibration guarantee of the Quantile Tracker (Proposition 1) follows directly from the $(R, 0)$ restorativity of ℓ_t and Proposition 3. This connection was first observed in Corollary 1 of [Angelopoulos et al. \(2025\)](#).

Projected gradient descent does not achieve constrained GEQ. Perhaps the most common way to enforce iterate constraints is via projection. Now that we have seen that online gradient descent with constant step sizes achieves gradient equilibrium, a natural first guess for achieving constrained gradient equilibrium is to run projected gradient descent. Given constraint sets C_t , $t = 1, 2, \dots$, initial point $\theta_1 \in C_1$, and learning rate $\eta > 0$, *projected gradient descent* obtains iterates via the update rule

$$\theta_{t+1} = \Pi_{C_{t+1}}(\theta_t - \eta g_t(\theta_t)). \quad (18)$$

This can also be written as a two-step procedure involving a hidden iterate $\tilde{\theta}_t$, where we first play $\theta_t = \Pi_{C_t}(\tilde{\theta}_t)$ and then perform the hidden iterate update $\tilde{\theta}_{t+1} = \theta_t - \eta g_t(\theta_t)$. Note that projected gradient descent is equivalent to agile mirror descent with regularizer $\mathcal{R}(x) = \|x\|_2^2/2$ ([Hazan, 2019](#)). Unfortunately, projected

gradient descent does not guarantee gradient equilibrium in general, and, in fact, provably fails to achieve our goal of calibration without crossings. To see why, observe that we can view projected gradient descent as online gradient descent on the subgradient

$$\tilde{g}_t(\theta) = g_t(\theta) + g_{I_t}(\theta), \quad (19)$$

where g_{I_t} is the subgradient of the characteristic function

$$I_t(\theta) = \begin{cases} 0 & \text{if } \theta \in C_t \\ \infty & \text{otherwise.} \end{cases}$$

By the gradient equilibrium guarantee for online gradient descent (Proposition 3), the projected gradient descent iterates satisfy $\lim_{T \rightarrow \infty} \frac{1}{T} \sum_{t=1}^T \tilde{g}_t(\theta_t) = 0$, which implies

$$\lim_{T \rightarrow \infty} \frac{1}{T} \sum_{t=1}^T g_t(\theta_t) = \lim_{T \rightarrow \infty} \frac{1}{T} \sum_{t=1}^T g_{I_t}(\theta_t).$$

The right-hand side is not zero in general,³ thus projected gradient descent is not guaranteed to achieve gradient equilibrium. The next proposition formally states that projected gradient descent is not only not guaranteed but, in fact, fails to solve our calibration without crossings problem (see Appendix C for proof).

Proposition 4 (Projected gradient descent fails). *Let $\theta_t, t = 1, 2, \dots$ be the iterates obtained from running projected gradient descent, as described in (18), with the MultiQT losses ℓ_t defined in (11) and constraint sets $C_t = \mathcal{K} - b_t$ at each time t . There exists a set of levels \mathcal{A} and sequence of (y_t, b_t) with $|y_t - b_t^\alpha| < R$ for all α and t (for some $R > 0$) such that for some quantile level $\alpha \in \mathcal{A}$, we have $\lim_{T \rightarrow \infty} \frac{1}{T} \sum_{t=1}^T \mathbb{1}\{y_t \leq b_t^\alpha + \theta_t^\alpha\} \neq \alpha$.*

3.2 Lazy gradient descent

As we saw above, incorporating constraints into gradient descent via projected gradient descent fails to achieve gradient equilibrium. Another way to incorporate constraints into gradient descent is the following: Given constraint sets $C_t, t = 1, 2, \dots$, initial hidden iterate $\tilde{\theta}_1 \in C_1$, and learning rate $\eta > 0$, *lazy (projected) gradient descent* (Zinkevich, 2003) obtains iterates via a two-step procedure:

$$\theta_t = \Pi_{C_t}(\tilde{\theta}_t) \quad (20)$$

$$\tilde{\theta}_{t+1} = \tilde{\theta}_t - \eta g_t(\theta_t). \quad (21)$$

“Lazy” refers to how (21) takes the gradient step starting from the hidden iterate $\tilde{\theta}_t$ rather than the played iterate θ_t . Applying the same rearranging and averaging procedure used in Section 3.1 to derive the expression for the average gradients of online gradient descent, the update rule (21) implies that the lazy gradient descent iterates satisfy

$$\frac{1}{T} \sum_{t=1}^T g_t(\theta_t) = \frac{\tilde{\theta}_1 - \tilde{\theta}_{T+1}}{\eta T}. \quad (22)$$

³For an extended discussion, see Appendix B.1 of Angelopoulos et al. (2025). Briefly, the subgradient $g_{I_t}(\theta_t)$ is zero if θ_t is in the interior of C_t but when θ_t is on the boundary of C_t , it can take on any value in the normal cone to C_t at θ_t . Since projected gradient descent can produce iterates that fall on the boundary of the constraint set arbitrarily often, we cannot guarantee that $\lim_{T \rightarrow \infty} \frac{1}{T} \sum_{t=1}^T g_{I_t}(\theta_t)$ is controlled.

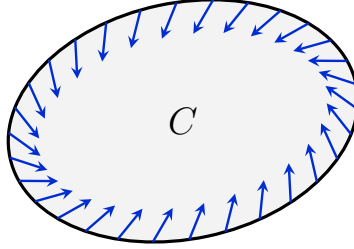


Figure 3: Visualization of inward flow. The blue arrows represent the negative gradient $-g$ evaluated at points on the boundary of the constraint set C .

This is identical to the average gradient expression for online gradient descent (15) except with all θ_t 's replaced with $\tilde{\theta}_t$'s. Whereas with online gradient descent, we wanted to show that the played iterates θ_t remained bounded or growing sublinearly, here we want to control the hidden iterates $\tilde{\theta}_t$. For online gradient descent, restorativity and Lipschitzness of the losses was a sufficient condition for the desired boundedness. Here, we need to introduce an additional condition that applies jointly to the loss function and constraint set at each time step.

Definition 4 (Inward flow). Let ℓ be a loss function with gradient g and let C be a closed convex set. The pair (ℓ, C) satisfies *inward flow* if, for any θ on the boundary of C , the negative gradient is in the tangent cone of C at θ — that is,

$$-g(\theta) \in T_C(\theta) \quad \text{for all } \theta \in \text{bd}(C),$$

where the tangent cone of a set C at a point x is defined as

$$T_C(x) = \text{cl}\{y : \text{there exists } \beta > 0 \text{ such that } x + \varepsilon y \in C \text{ for all } \varepsilon \in [0, \beta]\}$$

and cl denotes closure.

Inward flow says that starting at any θ on the edge of the constraint set and taking an arbitrarily small step in the direction of the negative gradient keeps us within the constraint set. In other words, following the direction of steepest descent causes us to “flow” further into the constraint set. We provide a visualization in Figure 3. This property plays an important role in our analysis of lazy gradient descent because whenever $\tilde{\theta}_t$ is outside of C_t , it is projected to a point θ_t on the boundary of C_t . Inward flow then ensures that the gradient at θ_t points into C_t , which allows us to control terms of the form $\langle g_t(\theta_t), \tilde{\theta}_t \rangle$ and, in turn, establish that $\tilde{\theta}_t$ remains bounded (or grows sublinearly). We emphasize that inward flow is a joint property of the loss function and the constraint set: For a loss function ℓ and two convex constraint sets C and \tilde{C} , just because (ℓ, C) satisfies inward flow does not mean that (ℓ, \tilde{C}) will also satisfy inward flow. We return to this in Section 6.

Combining restorativity and inward flow, we arrive at the following result.

Proposition 5 (Lazy gradient descent achieves GEQ under inward flow). *Suppose at each time t , the loss function ℓ_t is L -Lipschitz and $(h_t, 0)$ -restorative and the pair (ℓ_t, C_t) satisfies inward flow. Then the hidden iterates of lazy gradient descent satisfy $\|\tilde{\theta}_{T+1}\|_2 \leq \sqrt{\|\tilde{\theta}_1\|_2^2 + \eta^2 L^2 T + 2\eta L \sum_{t=1}^T h_t}$. If h_t is nondecreasing, this implies*

$$\left\| \frac{1}{T} \sum_{t=1}^T g_t(\theta_t) \right\|_2 \leq \frac{2\|\tilde{\theta}_1\|_2}{\eta T} + \sqrt{\frac{L^2}{T} + \frac{2Lh_T}{\eta T}}, \quad (23)$$

which goes to zero as $T \rightarrow \infty$ as long as h_t is sublinear.

We observe that Proposition 3 can be recovered as a special case of this result; online gradient descent is an instance of lazy gradient descent where the constraint set at every time t is $C_t = \mathbb{R}^d$, so the projection always results in $\theta_t = \tilde{\theta}_t$. Since the boundary of \mathbb{R}^d is empty, inward flow is always trivially satisfied by online gradient descent regardless of the loss functions. Removing that condition of Proposition 5 and replacing $\|\tilde{\theta}_1\|_2$ with $\|\theta_1\|_2$ exactly recovers Proposition 3.

This result can be extended to the delayed feedback setting. Consider *lazy gradient descent with constant delay $D \geq 0$* , which maintains the projection step in (20) but applies gradient updates to the hidden iterates in a delayed way:

$$\tilde{\theta}_{t+1} = \tilde{\theta}_t - \eta g_{t-D}(\theta_{t-D}), \quad (24)$$

where we define $g_t(\theta_t) = \mathbf{0}$ for $t \leq 0$.

Proposition 6 (Lazy gradient descent with delay achieves GEQ under inward flow). *Under the conditions of Proposition 5, the iterates of lazy gradient descent with $D \geq 0$ satisfy*

$$\|\tilde{\theta}_{T+1}\|_2 \leq \sqrt{\|\tilde{\theta}_1\|_2^2 + \eta^2 L^2 (2D+1)T + 2\eta L \sum_{t=1}^{T-D} h_t}.$$

If h_t is nondecreasing, this implies

$$\left\| \frac{1}{T} \sum_{t=1}^T g_t(\theta_t) \right\|_2 \leq \frac{2\|\tilde{\theta}_1\|_2}{\eta T} + \sqrt{\frac{L^2(2D+1)}{T} + \frac{2Lh_{T-D}}{\eta T}} + \frac{DL}{T}. \quad (25)$$

Comparison of online gradient descent methods with constraints. We now consider why lazy gradient descent succeeds at achieving gradient equilibrium whereas other ways of combining gradient descent with projection fail. Table 1 outlines three such methods we have considered: Post hoc projection, projected gradient descent, and lazy gradient descent. Post hoc projection is the method explored in the $m = \Pi_K$ case of Proposition 2, where we showed that it fails to achieve gradient equilibrium for our problem of calibration without crossings. We showed that projected gradient descent similarly fails in Proposition 4. However, as we just stated in Proposition 5, lazy gradient descent successfully solves the constraint gradient equilibrium problem by both enforcing the constraints *and* satisfying gradient equilibrium.

The way that the constraint is enforced — projection — is the same for all methods. The only difference is the update step. Of the three methods, only lazy gradient descent is guaranteed to achieve gradient equilibrium. We provide some intuition for why lazy gradient descent is a “Goldilocks” approach: First, *post hoc projection discards current information*. Under post hoc projection, feedback for the played iterate is never incorporated into subsequent updates. Since our goal is to drive the average gradient $g_t(\theta_t)$ toward zero, it would be valuable to use the observed gradient $g_t(\theta_t)$ to inform future iterates. Post hoc projection ignores this information. Second, *projected gradient descent discards past information*. In projected gradient descent, the update depends only on the projected point θ_t , and the unprojected iterate $\tilde{\theta}_t$ does not appear in the update. Since projection does not preserve all information about $\tilde{\theta}_t$, the method fails to fully utilize the accumulated knowledge encoded in $\tilde{\theta}_t$. Finally, *lazy gradient descent combines both sources of information*. It preserves past knowledge by updating from $\tilde{\theta}_t$ while simultaneously incorporating present feedback through the gradient evaluated at θ_t . This blend between retaining history and responding to current information enables lazy gradient descent to achieve gradient equilibrium.

Table 1: Comparison of online gradient descent methods that incorporate constraints. We abbreviate “gradient descent” as GD.

	<u>Post hoc projection</u>	<u>Projected GD</u>	<u>Lazy GD</u>
Projection		$\theta_t = \Pi_{C_t}(\tilde{\theta}_t)$	
Update	$\tilde{\theta}_{t+1} = \tilde{\theta}_t - \eta_t g_t(\tilde{\theta}_t)$	$\tilde{\theta}_{t+1} = \theta_t - \eta_t g_t(\theta_t)$	$\tilde{\theta}_{t+1} = \tilde{\theta}_t - \eta_t g_t(\theta_t)$
Enforces constraint?	✓	✓	✓
Satisfies GEQ?	✗	✗	✓*

*under inward flow

As a final remark on alternative methods, we note that it is important that constraints are enforced via projection. In the context of calibration without crossings, we find that modifying MultiQT by replacing $q_t = \Pi_{\mathcal{K}}(b_t + \tilde{\theta}_t)$ with $q_t = \text{SORT}(b_t + \tilde{\theta}_t)$ results in a procedure that provably fails to achieve calibration (see Proposition 13 in the Appendix). When sorting is applied, the resulting point is not in general on the boundary of the constraint set of ordered vectors. Thus, inward flow does not tell us anything about this point.

4 Guarantees for MultiQT

Having introduced the framework of constrained gradient equilibrium in the previous section, we are now ready to present the theoretical guarantees of MultiQT. Recall the proof roadmap presented in Figure 2. We have already shown: (1) Calibration without crossings is an instance of constrained gradient equilibrium. (2) Lazy gradient descent solves constrained gradient equilibrium problems that satisfy Lipschitz, restorativity, and inward flow conditions (Proposition 5). What remains to be shown is:

1. MultiQT is the relevant instantiation of lazy gradient descent for the calibration without crossings problem.
2. Calibration without crossings satisfies the Lipschitz, restorativity, and inward flow conditions.

If these two statements are true, then it directly follows that MultiQT solves calibration without crossings. Furthermore, if we show that MultiQT is an instance of lazy gradient descent, we inherit a regret guarantee for free.

MultiQT is lazy gradient descent. It is easy to show that MultiQT is an instance of lazy gradient descent. Referring back to Procedure 1, we observe that it is exactly equivalent to lazy gradient descent with the MultiQT loss defined in (11) and constraint sets $C_t = \mathcal{K} - b_t$ for $t = 1, 2, \dots$. As explained in Section 3, constrained gradient equilibrium with respect to this choice of loss function and constraint set is equivalent to calibration without crossings. We have thus shown the first statement is true. We now focus on the second.

4.1 Calibration guarantee

To show the desired calibration guarantee for MultiQT, we must show that the procedure satisfies the Lipschitz, restorativity, and inward flow conditions of Proposition 5. Lipschitzness is straightforward to show: The MultiQT loss at time t has gradient g_t that satisfies $\|g_t(\theta)\|_2 = \sqrt{\sum_{\alpha \in \mathcal{A}} (\text{cov}_t^\alpha - \alpha)^2} \leq \sqrt{\sum_{\alpha \in \mathcal{A}} 1} = \sqrt{|\mathcal{A}|}$, so it is $\sqrt{|\mathcal{A}|}$ -Lipschitz. The second condition, restorativity, is satisfied by the MultiQT losses as long as the errors between the base forecast and true values are bounded, as the following lemma formally states.

Lemma 1 (Restorativity of MultiQT loss). *Suppose the residuals are bounded: $|y_t - b_t^\alpha| \leq R$ for all $\alpha \in \mathcal{A}$ and times t for some $R > 0$. Define $d_{\mathcal{A}} = \min_{\alpha \in \mathcal{A}} \min(\alpha, 1 - \alpha)$ to be the smallest distance between any level in \mathcal{A} and an edge of $[0, 1]$. Then the MultiQT loss defined in (11) is $(h, \phi(h))$ -restorative for any $h \geq \frac{R|\mathcal{A}|^{3/2}}{d_{\mathcal{A}}}$ and $\phi(h) = \frac{hd_{\mathcal{A}}}{\sqrt{|\mathcal{A}|}} - R|\mathcal{A}|$.*

Finally, we must show that MultiQT satisfies inward flow.

Lemma 2 (Inward flow of MultiQT). *MultiQT satisfies inward flow — that is, at all times t , the gradient g_t of the MultiQT loss defined in (11) and constraint set C_t defined in (13) satisfy $-g_t(\theta) \in T_{C_t}(\theta)$ for all θ on the boundary of C_t .*

As we discuss further in Section 6, inward flow is not satisfied by arbitrary losses and constraints, and Lemma 2 exploits structure specific to MultiQT. We now state the main result for MultiQT, which follows directly from previously stated results.

Theorem 1 (Calibration guarantee for MultiQT). *If $|y_t - b_t^\alpha| \leq R$ for all $\alpha \in \mathcal{A}$ and times t , then for every quantile level $\alpha \in \mathcal{A}$, the MultiQT iterates satisfy*

$$\left| \frac{1}{T} \sum_{t=1}^T \text{cov}_t^\alpha - \alpha \right| \leq \frac{2\|\tilde{\theta}_1\|_2}{\eta T} + \sqrt{\frac{|\mathcal{A}|}{T} + \frac{2R|\mathcal{A}|^{3/2}}{\eta d_{\mathcal{A}} T}}. \quad (26)$$

Proof. By Lemma 1 and Lemma 2, we can apply Proposition 5 with $h = \frac{R|\mathcal{A}|^{3/2}}{d_{\mathcal{A}}}$, $\phi(h) = 0$, and Lipschitz constant $L = \sqrt{|\mathcal{A}|}$. This yields a bound on the ℓ_2 -norm of the average gradients. To obtain the calibration error bound for each individual quantile level, we use the fact that for any vector $x = [x_1, x_2, \dots, x_m]$, we have $|x_i| \leq \|x\|_2$ for all $i = 1, 2, \dots, m$. \square

Theorem 1 tells us that MultiQT is guaranteed to achieve calibration, as described in (1). Furthermore, the projection step ensures that the forecasts satisfy the desired distributional consistency property from (2). Thus, we have shown that the method we propose is guaranteed to satisfy our initial desiderata. This is true even if there is a delay in observing y_t ; applying the delayed feedback version of Proposition 5 tells us that MultiQT with delayed feedback, as described in (7), achieves the same calibration guarantee given in Theorem 1 except the bound worsens with increasing delay.

Proposition 7 (Calibration guarantee for MultiQT with delay). *Under the conditions of Theorem 1, for every quantile level $\alpha \in \mathcal{A}$, MultiQT with constant delay $D \geq 0$ satisfies*

$$\left| \frac{1}{T} \sum_{t=1}^T \text{cov}_t^\alpha - \alpha \right| \leq \frac{2\|\tilde{\theta}_1\|_2}{\eta T} + \sqrt{\frac{|\mathcal{A}|(2D+1)}{T} + \frac{2R|\mathcal{A}|^{3/2}}{\eta d_{\mathcal{A}} T} + \frac{D|\mathcal{A}|^{1/2}}{T}}. \quad (27)$$

4.2 Regret guarantee

In this section, we provide a regret guarantee for MultiQT with respect to the aggregated quantile loss. Before presenting the result, we briefly explain why this quantity is a relevant performance metric. Recall our secondary objective after calibration without crossings is *sharpness* — we want forecasts to be as concentrated and informative as possible. It turns out that the aggregated quantile loss $\rho_{\mathcal{A}}$ from (10) captures both calibration and sharpness. A convenient way to see this is through its equivalence to the weighted interval score. Consider the centered β -level forecast interval $[q^{\beta/2}, q^{1-\beta/2}]$, which aims to contain y with probability $1 - \beta$. Given a realization of y , we can compute the *interval score*:

$$\text{IS}_{\beta}([q^{\beta/2}, q^{1-\beta/2}], y) = (q^{1-\beta/2} - q^{\beta/2}) + \frac{2}{\beta} \cdot \text{dist}(y, [q^{\beta/2}, q^{1-\beta/2}]).$$

The first term penalizes wider intervals and therefore captures sharpness. The second term captures coverage: $\text{dist}(y, [q^{\beta/2}, q^{1-\beta/2}])$ is defined to be zero when y lies inside the interval; otherwise it is the distance between y and the side of the interval to which it is closest.

Given forecast intervals $[q^{\beta/2}, q^{1-\beta/2}]$ at multiple coverage levels $\beta \in \mathcal{B}$, we can combine the individual interval scores into the *weighted interval score*:

$$\text{WIS}_{\mathcal{B}}(\{[q^{\beta/2}, q^{1-\beta/2}]\}_{\beta \in \mathcal{B}}, y) = \sum_{\beta \in \mathcal{B}} \beta \cdot \text{IS}_{\beta}([q^{\beta/2}, q^{1-\beta/2}], y).$$

To relate this to the aggregated quantile loss, define

$$\mathcal{A} = \bigcup_{\beta \in \mathcal{B}} \{\beta/2, 1 - \beta/2\},$$

which is the set of quantile levels needed to construct the centered β -level forecast intervals for all $\beta \in \mathcal{B}$. Let $q = [q^{\alpha_1}, q^{\alpha_2}, \dots, q^{\alpha_{|\mathcal{A}|}}]$ denote the corresponding quantile forecasts. As long as the quantile forecasts are non-crossing, it can be shown that the aggregated quantile loss is equal to the weighted interval score divided by two:

$$\rho_{\mathcal{A}}(q, y) = \frac{1}{2} \cdot \text{WIS}_{\mathcal{B}}(\{[q^{\beta/2}, q^{1-\beta/2}]\}_{\beta \in \mathcal{B}}, y).$$

Thus, the aggregated quantile loss inherits the sharpness–calibration decomposition of the interval score.

In addition to blending the desiderata of calibration and sharpness, the aggregated quantile loss also has the desirable property of being a strictly proper scoring rule, ensuring that a forecaster who knows they are being evaluated according to the quantile loss is incentivized to report honest forecasts. As a result, the quantile loss is a common measure of quantile forecast performance used by the applied forecasting community, where it goes by the name *quantile score* (Chen et al., 2022; Gneiting et al., 2023).

Now that we have motivated why the aggregated quantile loss deserves consideration, we will state the regret guarantee for MultiQT. This guarantee is inherited by virtue of MultiQT being an instance of online mirror descent (see, e.g., Zinkevich (2003); Shalev-Shwartz et al. (2012); Hazan (2019) for such regret bounds). Let $\mathcal{C} = \bigcap_{t=1}^{T+1} \mathcal{C}_t$ be the intersection of MultiQT constraint sets over time, as defined in (13). This minimally includes the set $\{x \in \mathbb{R}^{|\mathcal{A}|} : x_1 \leq x_2 \leq \dots \leq x_{|\mathcal{A}|}\}$ of ordered offsets. The following result states that, in the long run, the average aggregated quantile loss of MultiQT forecasts will be no worse than applying any constant correction from \mathcal{C} to the base forecaster, up to an additive term depending on the learning rate η and the number of quantile levels $|\mathcal{A}|$.

Proposition 8 (Regret of MultiQT). *Let $\ell_t(\theta) = \rho_{\mathcal{A}}(b_t + \theta, y_t)$ be the MultiQT loss. If $|y_t - b_t^\alpha| \leq R$ for all levels $\alpha \in \mathcal{A}$ and times t , then the average loss of the MultiQT offsets $\theta_1, \theta_2, \dots, \theta_T$ starting from initialization $\tilde{\theta}_1 = \mathbf{0}$ compared to any constant vector of offsets $\theta \in \mathcal{C}$ satisfies*

$$\frac{1}{T} \sum_{t=1}^T \ell_t(\theta_t) - \frac{1}{T} \sum_{t=1}^T \ell_t(\theta) \leq \frac{R^2 |\mathcal{A}|}{2\eta T} + 2\eta |\mathcal{A}|. \quad (28)$$

We remark that when $\tilde{\theta}_1 \neq \mathbf{0}$, the result holds but with $\frac{R^2 |\mathcal{A}|}{2\eta T}$ replaced by $\frac{(R\sqrt{|\mathcal{A}|} + \|\tilde{\theta}_1\|_2)^2}{2\eta T}$. The quantity on the left-hand side of (28) represents the “regret” of using MultiQT compared to a constant offset of θ , and we will refer to it as $\text{Regret}_T(\theta) := \frac{1}{T} \sum_{t=1}^T \ell_t(\theta_t) - \frac{1}{T} \sum_{t=1}^T \ell_t(\theta)$. As stated, the result says that the regret of MultiQT compared to any constant correction to the base forecasts is at most $2\eta |\mathcal{A}|$ as T goes to infinity. Plugging in the learning rate that minimizes the right hand side ($\eta = \frac{R}{2\sqrt{T}}$) gives

$$\text{Regret}_T(\theta) \leq \frac{2R |\mathcal{A}|}{\sqrt{T}}. \quad (29)$$

This is a no-regret result: The regret bound goes to zero as the number of time steps goes to infinity. Although the learning rate of $\eta = \frac{R}{2\sqrt{T}}$ suggests that a priori knowledge of the horizon T is needed, the same $O(1/\sqrt{T})$ rate can be achieved without knowledge of T by using decaying learning rates $\eta_t \propto 1/\sqrt{t}$ — see, e.g., [Hazan \(2019\)](#).

Notably, applying Proposition 8 to $\theta = \mathbf{0}$ tells us that running MultiQT will, at worst, lead to only mildly worse average loss compared to using the raw forecasts b_t . In other words, for any learning rate and any base forecaster, Proposition 8 provides a “do bounded harm” guarantee, where the bound is controlled by the learning rate.

It is worth noting that when MultiQT is run with no base forecaster ($b_t = \mathbf{0}$ for all t), Proposition 8 has the following interpretation: After T time steps, we can compare the regret of the MultiQT iterates to the vector of empirical α -quantiles of the observed y_1, y_2, \dots, y_T for each $\alpha \in \mathcal{A}$. The result bounds the MultiQT regret compared to these true empirical quantiles in hindsight.

The next result, adapted from [Quanrud and Khashabi \(2015\)](#), says that a similar regret guarantee holds for MultiQT with delayed feedback.

Proposition 9 (Regret of MultiQT with delay). *Under the conditions of Proposition 8, the regret of MultiQT with constant delay $D \geq 0$ compared to any $\theta \in \mathcal{C}$ where $\mathcal{C} = \bigcap_{t=1}^{T+D+1} (\mathcal{K} - b_t)$ satisfies*

$$\text{Regret}_T(\theta) \leq \frac{R^2 |\mathcal{A}|}{2\eta T} + 2\eta |\mathcal{A}|(D+1). \quad (30)$$

For the optimal learning rate $\eta = \frac{R}{2} \sqrt{\frac{1}{(D+1)T}}$, this becomes

$$\text{Regret}_T(\theta) \leq \frac{2R |\mathcal{A}| \sqrt{D+1}}{\sqrt{T}}.$$

4.3 Calibration-regret trade-off

In the bounds provided in Theorem 1 and Proposition 8, there is a trade-off when choosing the learning rate η . If we want to solely optimize the calibration error bound, we should choose a learning rate that is constant in T , resulting in an $O(1/\sqrt{T})$ calibration error bound and an $O(1)$ regret bound. Conversely, if we want to solely optimize the regret bound, we would choose $\eta \propto 1/\sqrt{T}$, resulting in an $O(T^{-1/4})$ calibration error bound and an $O(1/\sqrt{T})$ regret bound.

Suppose we care about controlling both the calibration error bound and the regret bound. Then, plugging in the bounds on each, we get

$$\left| \frac{1}{T} \sum_{t=1}^T \text{cov}_t^\alpha - \alpha \right| + \text{Regret}_T(\theta) = O \left(\frac{1}{\sqrt{\eta T}} + \frac{1}{\eta T} + \eta \right). \quad (31)$$

This bound is minimized by choosing $\eta \propto T^{-1/3}$, which ensures that both the calibration error and regret bounds are $O(T^{-1/3})$. Whether this trade-off is fundamental or can be avoided with an appropriately designed algorithm is worth exploring in future work.

5 Experiments

We apply the MultiQT procedure to two real forecasting datasets relating to COVID-19 deaths and renewable energy production.

Metrics. Recall that our goal is calibration without crossing. Since MultiQT always satisfies “without crossings” by design, the main criteria we need to evaluate is calibration. We evaluate calibration in several ways. First, we consider the miscalibration of the forecasts at each quantile level $\alpha \in \mathcal{A}$ by examining the gap between the desired coverage α and the actual (empirical) coverage of the α -level forecasts. We convey this visually by plotting the actual coverage vs. desired coverage for each quantile level. Second, to summarize the miscalibration across all quantile levels into a single scalar metric, we compute the *(average) calibration error* as

$$\text{Calibration Error} = \frac{1}{|\mathcal{A}|} \sum_{\alpha \in \mathcal{A}} \left| \widehat{\text{Cov}}_\alpha - \alpha \right|,$$

where $\widehat{\text{Cov}}_\alpha = \frac{1}{T} \sum_{t=1}^T \text{cov}_t^\alpha$ is the empirical coverage of the α -level forecasts on the time series of length T . We use average calibration error as our main calibration metric in this section. An alternative method of summarizing miscalibration into a single metric is to compute the entropy of the distribution of probability integral transform values (Gneiting et al., 2007; Rumack et al., 2022), and we provide results using this metric in Appendix E.1.

Although our primary goal is calibration, the aggregated quantile loss is also of interest due to its connections to forecast sharpness and its ubiquity as an evaluation metric in the forecasting community, as explained in Section 4.2. We compute the *(average) quantile loss* as the time-averaged aggregated quantile loss:

$$\text{Quantile Loss} = \frac{1}{T|\mathcal{A}|} \sum_{t=1}^T \rho_{\mathcal{A}}(q_t, y)$$

Setting the learning rate. Although the calibration error bound in Theorem 1 suggests that setting a larger learning rate is better (to achieve better calibration), in practice, an excessively large learning rate leads to volatile forecasts that appear overly jagged. To determine an appropriate learning rate for MultiQT, we use a modified version of the heuristic used by Angelopoulos et al. (2023) to set the Quantile Tracker learning rate. They set the learning rate adaptively so that the learning rate at time t is 0.1 times the largest true residual $|y_t - b_t^\alpha|$ seen in the last 50 time steps. We replace the max of recent residuals with the 90% quantile to avoid setting excessively large learning rates after encountering a single large true value. Specifically, we set the learning rate at time t as $\eta_t = \max(0.01 \cdot \text{Quantile}_{0.9}(\cup_{\alpha \in \mathcal{A}} \{ |y_s - b_s^\alpha| \}_{s=t-51}^{t-1}), \epsilon)$ for $\epsilon = 0.1$. The $\max(\cdot, \epsilon)$ ensures that the learning rate is positive even if the residuals are zero.

5.1 COVID-19 death forecasting

During the COVID-19 pandemic, forecasts were important for public communication and informing public health decision making. The United States COVID-19 Forecast Hub is a repository of real-time forecasts of key COVID-19 outcomes collected during the pandemic in a collaborative effort between researchers at the University of Massachusetts, Amherst and the United States Center for Disease Control and Prevention (Cramer et al., 2022a). From April 2020 through April 2024, the Forecast Hub solicited quantile forecasts of weekly COVID-19 hospitalizations and deaths at the state and national level. Forecasts were collected for 23 quantile levels (0.01, 0.025, 0.05, 0.1, 0.15, 0.2, 0.25, 0.3, 0.35, 0.4, 0.45, 0.5, 0.55, 0.6, 0.65, 0.7, 0.75, 0.8, 0.85, 0.9, 0.95, 0.975, and 0.99) at forecast horizons of h week(s) ahead for $h \in \{1, 2, 3, 4\}$.

We apply our MultiQT procedure to weekly state-level COVID-19 death forecasts generated by 15 forecasting teams, corresponding to $15 \times 50 = 750$ time series for each forecast horizon h . Following Buchweitz et al. (2025), we restrict ourselves to forecasters with top performance in terms of quantile loss (as identified in Figure 2 of Cramer et al. (2022b)), then filter out forecasters with missing forecasts and those with forecasts for fewer than 50 time steps for any state. The selected forecasters have forecasts for periods ranging from 68 to 152 weeks. When applying MultiQT to $h = 1$ week ahead forecasts, we use the standard implementation described in Procedure 1. For $h \in \{2, 3, 4\}$, we run the delayed feedback version of MultiQT with a delay of $D = h - 1$. For some teams, the forecasts are well calibrated to begin with, whereas other forecasts are systematically biased in some way (too low or too high, or with confidence bands that are too narrow or too wide). We find that wrapping MultiQT around these forecasts successfully corrects for any biases and improves calibration, as we now describe.

Figure 4a plots the calibration of the raw one-week-ahead death forecasts submitted to the COVID-19 Forecast Hub. Forecasters that fall below the dotted black line are biased downwards, meaning that their forecasts are too small on average. Conversely, those that fall above are biased upwards, meaning that their forecasts are too large on average. Both forms of miscalibration dilute the utility of forecasts to decision makers. Figure 4b plots the calibration of the same forecasts after applying MultiQT. We see that MultiQT reduces both types of bias. In Figure 14 in the Appendix, we provide the analogous figures for two-, three-, and four-week-ahead forecasts, which exhibit a similar improvement in calibration after MultiQT is applied.

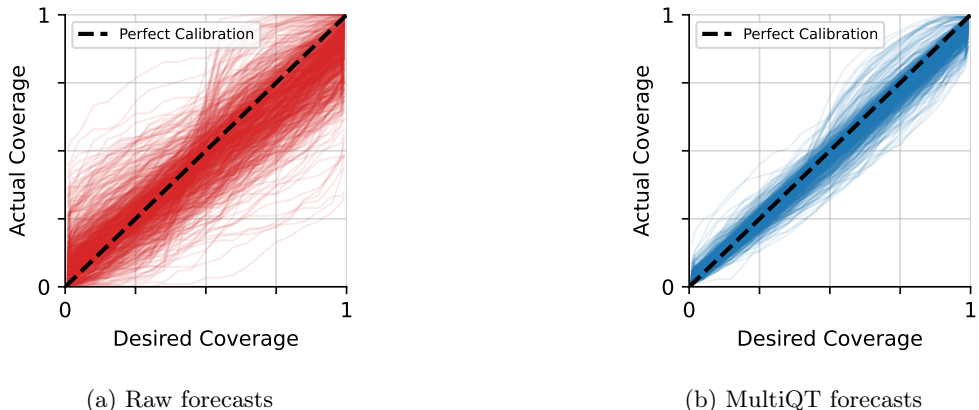


Figure 4: Actual coverage vs. desired coverage at each quantile level for one-week-ahead COVID-19 death forecasts before (red) and after (blue) applying MultiQT. Each forecaster \times state combination is a line.

Figure 5 illustrates the change in calibration error and quantile loss induced by MultiQT. The tail of the

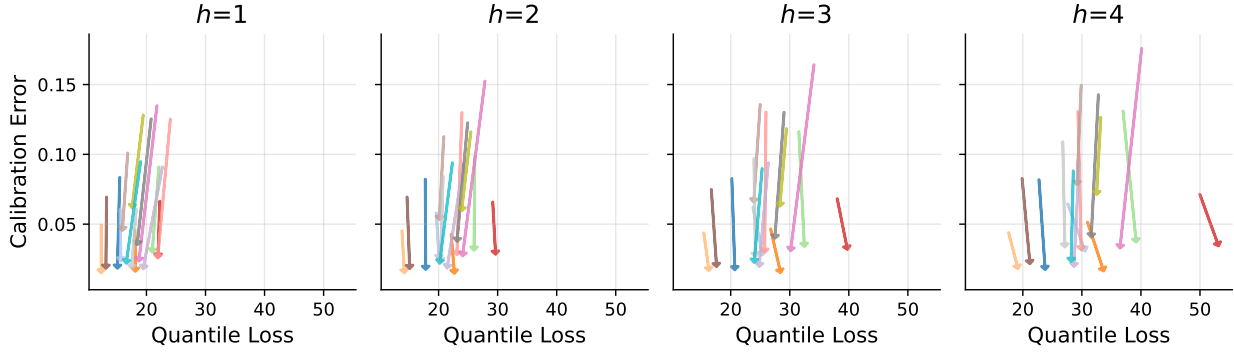


Figure 5: Average quantile loss and average calibration error for raw forecasts (**tail** of arrow) and MultiQT forecasts (**head** of arrow) for h -week-ahead COVID-19 death forecasts, where $h \in \{1, 2, 3, 4\}$. Each color represents a forecaster, and the coordinates of the head and tail are determined by averaging metrics across all 50 states for the specified horizon. For both metrics, lower is better.

arrow represents the performance of the raw forecasts and the head of the arrow represents the performance of the forecasts after applying MultiQT. All arrows point downwards, which tells us that MultiQT achieves the goal of improving calibration. In fact, after recalibrating with MultiQT, most forecasters achieve an average calibration error close to zero, corresponding to perfect calibration. We also see that this improvement in calibration does not ever significantly degrade the quantile loss and, in fact, often leads to a slight improvement. This is consistent with the regret guarantee stated in Proposition 8. In Figures 15 - 18 of Appendix E.2, we provide visualizations of how individual COVID-19 forecasters are improved by MultiQT.

5.2 Energy forecasting

While renewable energy sources such as wind and solar hold great promise for reducing carbon emissions, a significant downside is that they suffer from uncertain production due to the inherent stochasticity of weather. This uncertainty must be properly accounted for in order to successfully integrate renewable energy sources into the energy grid. To ensure that supply continuously meets demand, grid operators rely on accurate forecasts of renewable energy production to determine when it is necessary to procure additional energy reserves via balancing capacity markets.

The ARPA-E PERFORM dataset was created to help develop more efficient and reliable energy grids (Bryce et al., 2023). It consists of probabilistic forecasts made by the National Renewable Energy Laboratory, a national laboratory of the U.S. Department of Energy, for wind and solar energy for various sites in the United States along with the realized true values, all measured in megawatts. The quantile forecasts are made at 99 evenly spaced quantile levels from 0.1 to 0.99. We focus on day-ahead wind and solar power forecasting for sites belonging to the Electric Reliability Council of Texas (ERCOT), the main operator of the electrical grid in Texas. For wind power, there are 264 sites, and for solar power, there are 226 proposed sites, making a total of 490 sites. Day-ahead forecasts are made at 12:00 p.m. CST each day for the energy production during each hour of the subsequent day. These forecasts are then used by grid operators to determine whether (and for what times) to order balancing capacity products for the next day to ensure supply meets demand (Hirth and Ziegenhagen, 2015; Regelleistung, 2024). Balancing capacity products are available in four-hour blocks. The dataset provides forecasts for each day of 2018, yielding time series of length 365.

We run MultiQT separately for each hour of the day. For example, one sequence of y_t 's we consider is the

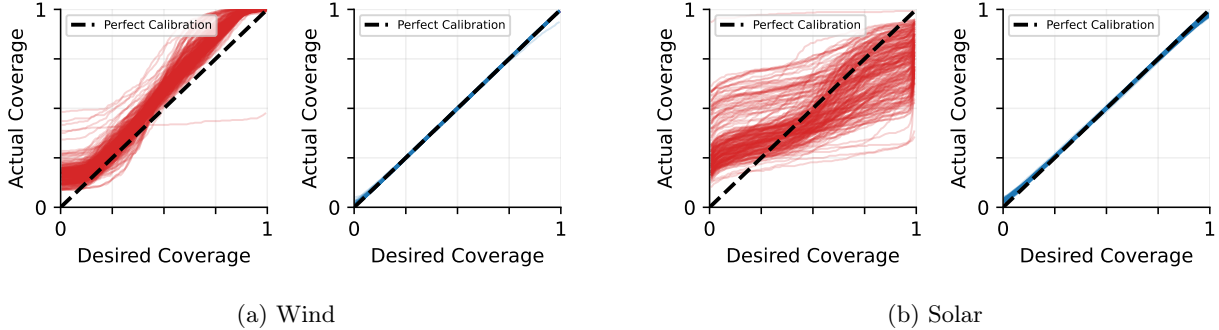


Figure 6: Actual coverage vs. desired coverage at each quantile level of day-ahead raw forecasts (red) and MultiQT-calibrated forecasts (blue) for wind and solar energy production at 10:00 a.m. CST.

wind production of a particular site at 10:00 a.m. on January 1, 10:00 a.m. on January 2, 10:00 a.m. on January 3, and so on. We specifically focus on the hours 2:00 a.m., 6:00 a.m., 10:00 a.m., 2:00 p.m., 6:00 p.m., and 10:00 p.m. CST. Each of these hours belongs to a different four-hour block and can be used to inform whether a balancing capacity product is needed for that time block. For the first three hours we selected (2:00 a.m., 6:00 a.m., 10:00 a.m.), feedback from the previous day’s forecast is available before the next day’s forecasts are issued at 12:00 p.m., so there is no delay in feedback. However, for the afternoon and evening hours (2:00 p.m., 6:00 p.m., and 10:00 p.m.), there is a one-day delay since we do not observe feedback for these hours before issuing the next day’s forecasts. For these hours, we run MultiQT with a feedback delay of $D = 1$.

Figure 6 visualizes the miscalibration of the quantile forecasts before and after applying MultiQT to the forecasts for energy production at 10:00 a.m. CST. The raw forecasts suffer from miscalibration: The wind forecasts are biased upwards, as evidenced by the calibration curves falling above the $y = x$ line, and the solar forecasts are too narrow, as evidenced by the nearly horizontal calibration curves. MultiQT corrects these issues and produces near perfect calibration. In Figure 19 in the Appendix, we see MultiQT causes a similar improvement in the calibration of energy forecasts for other hours of the day.

Figure 7 provides a holistic evaluation of MultiQT in terms of calibration and the average quantile loss for all six hours we consider. The results are qualitatively similar to the results for the COVID-19 dataset. MultiQT consistently improves forecast calibration and never substantially increases the average quantile loss. In particular, for the solar forecasts, we generally see a strong improvement in quantile loss due to the extremely poor calibration of the raw forecasts.

We remark that in energy production forecasting, calibration can translate directly into a reliability guarantee. For example, if a grid operator wants to ensure that 99% of the time, the energy supply at time t is at least D_t , they can do so by ordering $D_t - q_t^{0.99}$ of additional capacity via the balancing capacity market, where $(q_t^{0.99})_{t=1}^T$ is a calibrated sequence of 0.99-level quantile forecasts. This is because calibration guarantees that q_t^α is above y_t exactly $\alpha \times 100\%$ of the time in the long run, so $D_t - q_t^\alpha$ will be larger than the true supply gap $D_t - y_t$ exactly $\alpha \times 100\%$ of the time.

Case study. To better understand how MultiQT changes the base forecasts, we visualize the forecasts before and after applying MultiQT for a wind energy site that was particularly miscalibrated to begin with (Figure 8). For the sake of visualization, we show forecasts only for a 50-day period starting from March 1, 2018, but the calibration is computed on the entire year of 2018. We see that the raw forecasts are too

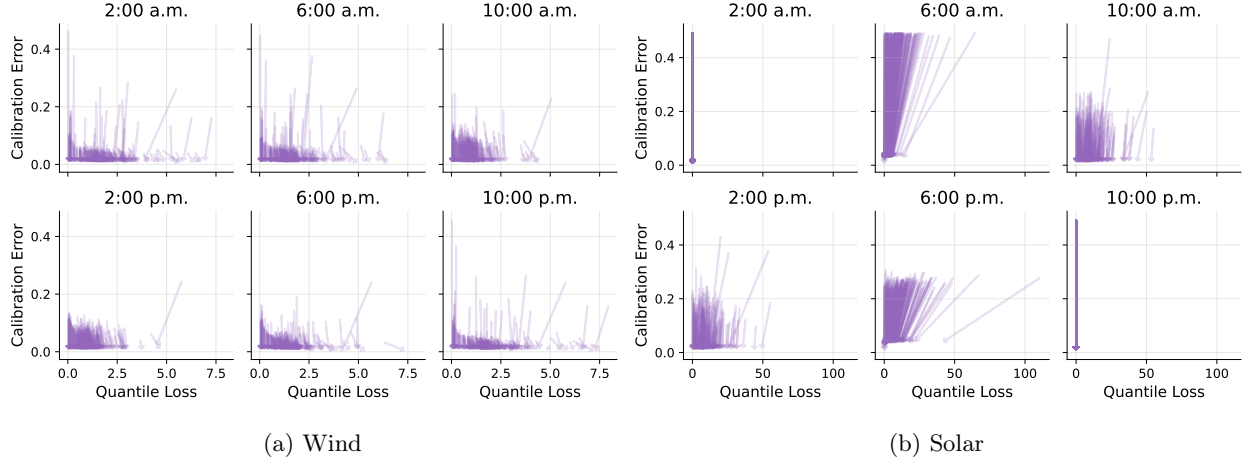


Figure 7: Average quantile loss and average calibration error for raw forecasts (**tail** of arrow) and MultiQT forecasts (**head** of arrow) for day-ahead wind and solar energy production at 2:00 a.m., 6:00 a.m., 10:00 a.m., 2:00 p.m., 6:00 p.m., and 10:00 p.m. CST. Each arrow corresponds to a wind or solar energy site. For both metrics, lower is better.

narrow in many places and fail to cover the true value, but MultiQT largely corrects for this and gives a better representation of the uncertainty. Figures 21 and 22 in Appendix E.3 reproduce this set of plots for additional wind and solar sites.

6 Discussion

From quantile forecasts to prediction intervals. In this paper, we proposed a simple procedure that can wrap around any existing quantile forecaster to produce corrected forecasts that are guaranteed to be calibrated without crossing. Throughout, we have touched on some reasons why calibration without crossings is an important problem. Here, we note one final application that we have already implicitly made use of when visualizing forecasts: Non-crossing quantile forecasts can be used to construct *nested* prediction intervals, and if the quantile forecasts are calibrated, the resulting prediction intervals will have the correct long-run coverage. Here, “nested” implies, for example, that an equal-tailed 0.5-level prediction interval is fully contained within an equal-tailed 0.9-level prediction interval. Concretely, suppose we want to construct a sequence of prediction intervals $I_t \subseteq \mathbb{R}$, $t = 1, 2, \dots$ with a long-run coverage of $1 - \alpha$ — that is, $\lim_{T \rightarrow \infty} \frac{1}{T} \sum_{t=1}^T \mathbb{1}\{y_t \in I_t\} = 1 - \alpha$. To do so, we can simply let $I_t = (q_t^{\alpha/2}, q_t^{1-\alpha/2}]$ where $q_t^{\alpha/2}$ has long-run coverage of $\alpha/2$, $q_t^{1-\alpha/2}$ has long-run coverage of $1 - \alpha/2$, and $q_t^{\alpha/2} \leq q_t^{1-\alpha/2}$ at all times t .⁴ As we have shown, such $q_t^{\alpha/2}$ and $q_t^{1-\alpha/2}$ can be obtained by running MultiQT. Then,

$$\frac{1}{T} \sum_{t=1}^T \mathbb{1}\{y_t \in I_t\} = 1 - \frac{1}{T} \sum_{t=1}^T \mathbb{1}\{y_t \leq q_t^{\alpha/2}\} - \frac{1}{T} \sum_{t=1}^T \mathbb{1}\{y_t > q_t^{1-\alpha/2}\} = 1 - \alpha/2 - \alpha/2 = 1 - \alpha,$$

where the first equality comes from our choice of I_t and the second equality comes from the long-run coverage of the individual quantile forecasts. Thus, the prediction interval has the correct coverage, and due to the no crossings property, constructing prediction intervals at different α levels will always result in nested intervals.

⁴In practice, we can use the closed interval $I_t = [q_t^{\alpha/2}, q_t^{1-\alpha/2}]$ and still achieve the correct coverage with probability one if y_t is continuously distributed with no point masses.

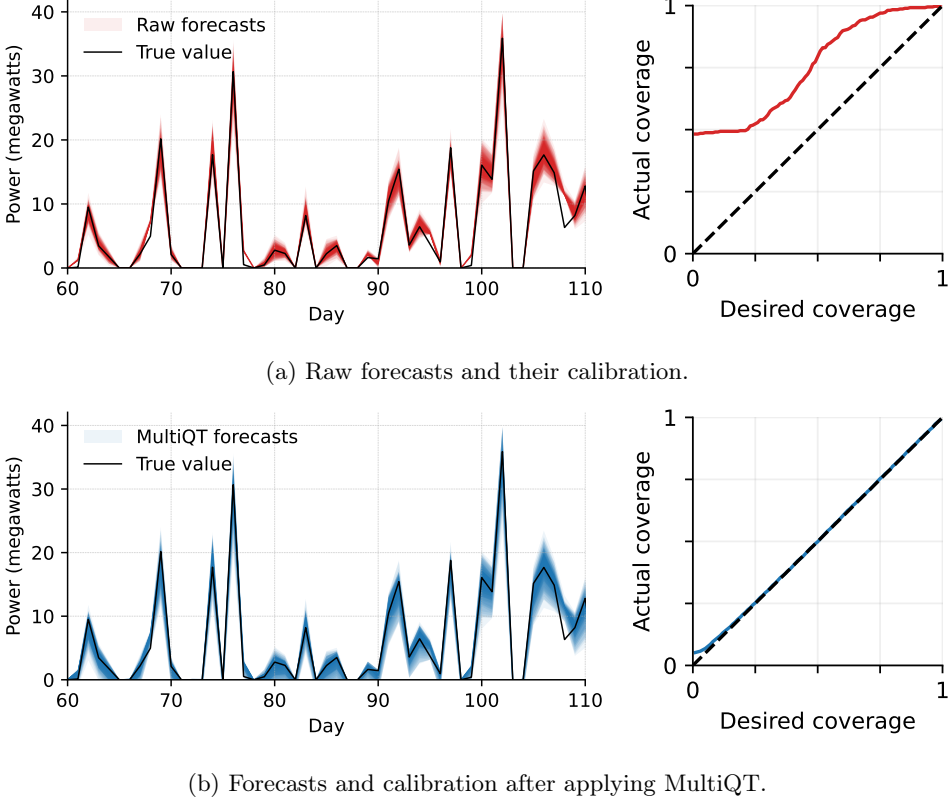


Figure 8: Day-ahead wind energy forecasts and corresponding calibration for the site `Wind_Power_Partners_94_Wind_Farm` for 10:00 a.m. CST each day from March 1, 2018 to April 20, 2018 before (red) and after (blue) applying MultiQT.

1/T rate for calibration error. In Section 4, we showed that the calibration error of the MultiQT forecasts approaches zero at a $O(1/\sqrt{T})$ rate. However, if we could guarantee that the distance between the hidden and played iterates is bounded by a constant, this would allow us to achieve a faster convergence rate. This is the case when all entries of b_t are the same at every t , i.e., b_t is a point forecast.

Lemma 3 (Point forecasts imply bounded projection distance). *If the base forecasts are point forecasts (i.e., $b_t = [k_t, k_t, \dots, k_t]$ for some $k_t \in \mathbb{R}$) and $|y_t - k_t| \leq R$ for all times t , then the MultiQT iterates satisfy $\|\theta_t - \tilde{\theta}_t\|_2 \leq \frac{\eta|\mathcal{A}|^{3/2}}{\sqrt{3}}$ for all t .*

The proof of this and following results can be found in Appendix D. We conjecture that the MultiQT iterates also maintain bounded projection distance in the general setting where b_t is an arbitrary ordered vector. Although our experiments provide empirical evidence of this, establishing it theoretically requires techniques beyond those used in Lemma 3 and thus we leave it as an open problem. We now state a bound on the average gradient for lazy gradient descent when the projection distance is known to be bounded.

Proposition 10 (GEQ of lazy gradient descent under bounded projection distance). *Let θ_t and $\tilde{\theta}_t$ be the played and hidden lazy gradient descent iterates as described in (20) and (21). Suppose at each time t , (i) the loss function ℓ_t is L -Lipschitz and (h_t, ϕ_t) -restorative, where ϕ_t satisfies $\phi_t(\theta) \geq \frac{\eta L^2}{2}$ whenever $\|\theta\|_2 > h_t$, (ii) the pair (ℓ_t, C_t) satisfies inward flow, and (iii) the iterates satisfy $\|\theta_t - \tilde{\theta}_t\|_2 \leq B$. Then the hidden iterates*

of lazy gradient descent satisfy $\|\tilde{\theta}_{T+1}\|_2 \leq \max(\|\tilde{\theta}_1\|_2, h_T) + B + \eta L$. If h_t is nondecreasing, this implies

$$\left\| \frac{1}{T} \sum_{t=1}^T g_t(\theta_t) \right\|_2 \leq \frac{2\|\tilde{\theta}_1\|_2}{\eta T} + \frac{L}{T} + \frac{h_T + B}{\eta T}. \quad (32)$$

Whereas the more general result in Proposition 5 gives a $O(1/\sqrt{T})$ rate, if we know that $\|\theta_t - \tilde{\theta}_t\|_2$ stays bounded over time, the result above gives a $O(1/T)$ rate. We can then combine Proposition 10 and Lemma 3 to get the following $1/T$ rate on the calibration error of MultiQT with point forecasts.

Corollary 1 (Calibration rate for MultiQT with point forecasts). *If the base forecasts are point forecasts (i.e., $b_t = [k_t, k_t, \dots, k_t]$ for some $k_t \in \mathbb{R}$) and $|y_t - k_t| \leq R$ for all times t then for every quantile level $\alpha \in \mathcal{A}$, the MultiQT iterates satisfy*

$$\left| \frac{1}{T} \sum_{t=1}^T \text{cov}_t^\alpha - \alpha \right| \leq \frac{2\|\tilde{\theta}_1\|_2}{\eta T} + \frac{|\mathcal{A}|^{1/2}}{T} + \frac{|\mathcal{A}|^{3/2}}{2d_{\mathcal{A}}T} + \frac{R|\mathcal{A}|^{3/2}}{d_{\mathcal{A}}\eta T} + \frac{|\mathcal{A}|^{3/2}}{T\sqrt{3}}. \quad (33)$$

Inward flow. A key condition we use in this paper is inward flow, which says that the negative gradient field points inwards at the boundary of the constraint set. We showed that lazy gradient descent leads to gradient equilibrium when inward flow is satisfied, and our calibration guarantee for MultiQT relies on the fact that the MultiQT loss and constraint set satisfy inward flow. Unfortunately, inward flow can be difficult to satisfy in general. For instance, it is not sufficient that the minimizer of the loss lies within the constraint set, because the gradient of a loss function does not always point towards the minimizer.

An example that is particularly relevant to multi-level quantile forecasting is the constraint set that results in ε -separated quantiles, i.e., $C_t = \{x \in \mathbb{R}^{|\mathcal{A}|} \mid x_i + b_t^{\alpha_i} + \varepsilon \leq x_{i+1} + b_t^{\alpha_{i+1}} \text{ for } i = 1, 2, \dots, |\mathcal{A}| - 1\}$. This constraint set could be used to produce quantile forecasts that not only do not cross but are also separated by $\varepsilon > 0$. Unfortunately, the MultiQT loss and this ε -separated constraint set do not satisfy inward flow. This is visualized in Figure 9. The negative gradient, represented by the blue arrows, does not point inwards at all boundary points of the ε -separated constraint set in Figure 9b. We can contrast this with Figure 9a, which visualizes the constraint set used in MultiQT. Furthermore, this violation of inward flow makes it so that running MultiQT with this modified constraint set provably fails to achieve calibration (see Proposition 14 of Appendix C for a counterexample).

This leads to some natural follow-up questions. What are other problems in which inward flow is satisfied? If we cannot show that inward flow is satisfied for a given problem, can we find another sufficient condition that is more general that can also be used to show that lazy gradient descent achieves gradient equilibrium? Are there other methods that can be developed to solve constrained gradient equilibrium? One constraint set of particular interest is the simplex. For this constraint, lazy gradient descent and projected gradient descent are equivalent (see, e.g., Hazan (2019)), so do both or neither procedure succeed?

We note some additional directions for future work: First, relating to Section 4.3: Does gradient descent (either the standard or lazy variant) optimally trade off calibration (or, more generally, gradient equilibrium) and regret? Moreover, is this trade-off fundamental, or can it be avoided by using the right algorithm? Second, if the forecast residuals $Y_t - b_t$ are predictable, which is particularly likely to be true in multi-horizon forecasting settings, can this predictability be leveraged to further improve the forecasts using scorecasting procedures as in Angelopoulos et al. (2023) and Wang and Hyndman (2024)? Third, the goal of our work is “marginal” calibration — can we find similarly simple methods for achieving *conditional* calibration subject to constraints? Although the problem of conditional calibration has been explored (see, e.g., Noarov et al.

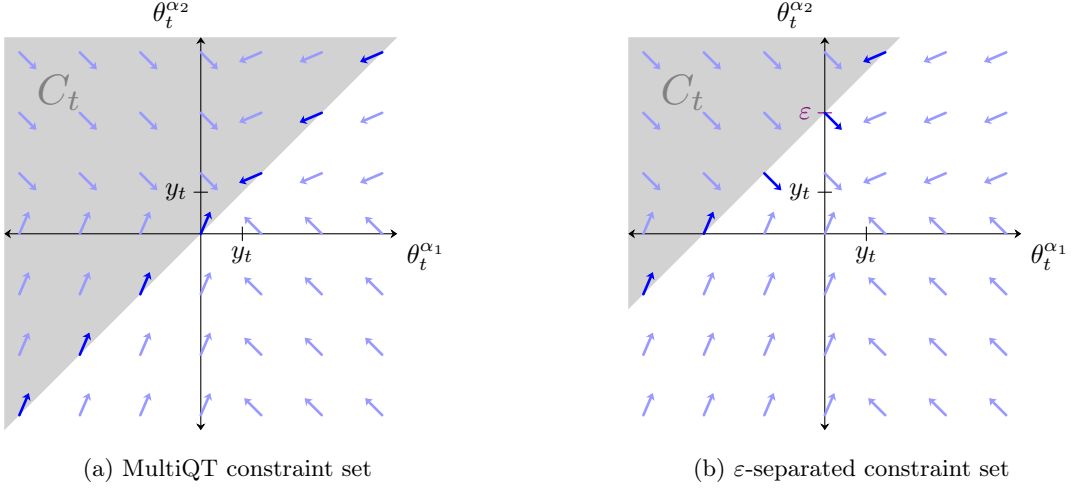


Figure 9: Visualization of the negative gradient of the MultiQT loss (blue arrows) in the two quantile case with no base forecaster ($b_t = \mathbf{0}$) and the y_t as marked. Whether inward flow is satisfied depends on the constraint set C_t ; it holds for the MultiQT constraint set but not the ε -separated constraint set

(2023)), we still lack a lightweight, easily implementable solution. Finally, a similar question can be asked of whether simple methods can be constructed to calibrate *distributional* forecasts, represented via a quantile function $q : [0, 1] \rightarrow \mathbb{R}$, subject to constraints.

Acknowledgments

We thank Rina Barber and Aaron Roth for helpful discussions and Erez Buchweitz for guidance on working with the COVID-19 Forecast Hub dataset. TD was supported by the National Science Foundation Graduate Research Fellowship Program under grant no. 2146752. IG and RJT were supported by the Office of Naval Research, ONR grant N00014-20-1-2787.

References

Anastasios N. Angelopoulos, Emmanuel J. Candès, and Ryan J. Tibshirani. Conformal PID control for time series prediction. In *Advances in Neural Information Processing Systems*, 2023.

Anastasios N. Angelopoulos, Michael I. Jordan, and Ryan J. Tibshirani. Gradient equilibrium in online learning: Theory and applications. *arXiv preprint arXiv:2501.08330*, 2025.

Miriam Ayer, H Daniel Brunk, George M Ewing, William T Reid, and Edward Silverman. An empirical distribution function for sampling with incomplete information. *The Annals of Mathematical Statistics*, pages 641–647, 1955.

Richard E. Barlow, D. J. Bartholomew, J. M. Bremner, and H. D. Brunk. *Statistical Inference Under Order Restrictions: The Theory and Application of Isotonic Regression*. Wiley, 1972.

Gilbert Bassett Jr and Roger Koenker. An empirical quantile function for linear models with iid errors. *Journal of the American Statistical Association*, 77(378):407–415, 1982.

Osbert Bastani, Varun Gupta, Christopher Jung, Georgy Noarov, Ramya Ramalingam, and Aaron Roth.

Practical adversarial multivalid conformal prediction. *Advances in Neural Information Processing Systems*, 35:29362–29373, 2022.

Aadyot Bhatnagar, Huan Wang, Caiming Xiong, and Yu Bai. Improved online conformal prediction via strongly adaptive online learning. In *Proceedings of the International Conference on Machine Learning*, 2023.

David Blackwell. An analog of the minimax theorem for vector payoffs. *Pacific Journal of Mathematics*, 6(1), 1956.

Sarah Brocklehurst, PY Chan, Bev Littlewood, and John Snell. Recalibrating software reliability models. *IEEE Transactions on Software Engineering*, 16(4):458–470, 1990.

Richard Bryce, Grant Buster, Kate Doubleday, Cong Feng, Ross Ring-Jarvi, Michael Rossol, Flora Zhang, and Bri-Mathias Hodge. Solar PV, wind generation, and load forecasting dataset for ERCOT 2018: Performance-based energy resource feedback, optimization, and risk management (PERFORM). Technical report, National Renewable Energy Laboratory (NREL), 2023.

Erez Buchweitz, João Vitor Romano, and Ryan J Tibshirani. Asymmetric penalties underlie proper loss functions in probabilistic forecasting. *arXiv preprint arXiv:2505.00937*, 2025.

Ying Cao and Zuo-Jun Max Shen. Quantile forecasting and data-driven inventory management under nonstationary demand. *Operations Research Letters*, 47(6):465–472, 2019.

Zhi Chen, Anil Gaba, Ilia Tsetlin, and Robert L Winkler. Evaluating quantile forecasts in the M5 uncertainty competition. *International Journal of Forecasting*, 38(4):1531–1545, 2022.

Victor Chernozhukov, Iván Fernández-Val, and Alfred Galichon. Quantile and probability curves without crossing. *Econometrica*, 78(3):1093–1125, 2010.

Estee Y. Cramer, Yuxin Huang, Yijin Wang, Evan L. Ray, Matthew Cornell, Johannes Bracher, Andrea Brennen, Alvaro J. Castro Rivadeneira, Aaron Gerding, Katie House, Dasuni Jayawardena, Abdul Hannan Kanji, Ayush Khandelwal, Khoa Le, Vidhi Mody, Vrushti Mody, Jarad Niemi, Ariane Stark, Apurv Shah, Nutcha Wattanachit, Martha W. Zorn, Nicholas G. Reich, and US COVID-19 Forecast Hub Consortium. The United States COVID-19 Forecast Hub dataset. *Scientific Data*, 9, 2022a.

Estee Y. Cramer, Evan L. Ray, Velma K. Lopez, Johannes Bracher, Andrea Brennen, Alvaro J. Castro Rivadeneira, Aaron Gerding, Tilmann Gneiting, Katie H. House, Yuxin Huang, Dasuni Jayawardena, Abdul H. Kanji, Ayush Khandelwal, Khoa Le, Anja Mühlmann, Jarad Niemi, Apurv Shah, Ariane Stark, Yijin Wang, Nutcha Wattanachit, Martha W. Zorn, Youyang Gu, et al. Evaluation of individual and ensemble probabilistic forecasts of COVID-19 mortality in the United States. *Proceedings of the National Academy of Sciences*, 119(15):e2113561119, 2022b.

Shachi Deshpande, Charles Marx, and Volodymyr Kuleshov. Calibrated regression against an adversary without regret. *arXiv preprint arXiv:2302.12196*, 2023.

Colin Doms, Sarah C Kramer, and Jeffrey Shaman. Assessing the use of influenza forecasts and epidemiological modeling in public health decision making in the united states. *Scientific Reports*, 8(1):12406, 2018.

Rasool Fakoor, Taesup Kim, Jonas Mueller, Alexander Smola, and Ryan J. Tibshirani. Flexible model aggregation for quantile regression. *Journal of Machine Learning Research*, 24(162):1–45, 2023.

Shai Feldman, Liran Ringel, Stephen Bates, and Yaniv Romano. Achieving risk control in online learning settings. *arXiv preprint arXiv:2205.09095*, 2022.

Dean P. Foster. A proof of calibration via Blackwell’s approachability theorem. *Games and Economic*

Behavior, 29(1-2):73–78, 1999.

Dean P. Foster and Sergiu Hart. Forecast hedging and calibration. *Journal of Political Economy*, 129(12):3447–3490, 2021.

Jan Gasthaus, Konstantinos Benidis, Yuyang Wang, Syama Sundar Rangapuram, David Salinas, Valentin Flunkert, and Tim Januschowski. Probabilistic forecasting with spline quantile function rnns. In *Proceedings of the International Conference on Artificial Intelligence and Statistics*, pages 1901–1910. PMLR, 2019.

Isaac Gibbs and Emmanuel J. Candès. Adaptive conformal inference under distribution shift. In *Advances in Neural Information Processing Systems*, 2021.

Isaac Gibbs and Emmanuel J. Candès. Conformal inference for online prediction with arbitrary distribution shifts. *Journal of Machine Learning Research*, 25(162):1–36, 2024.

Tilmann Gneiting and Roopesh Ranjan. Combining predictive distributions. *Electronic Journal of Statistics*, 7:1747–1782, 2013.

Tilmann Gneiting, Fadoua Balabdaoui, and Adrian E. Raftery. Probabilistic forecasts, calibration and sharpness. *Journal of the Royal Statistical Society: Series B*, 69(2):243–268, 2007.

Tilmann Gneiting, Daniel Wolfram, Johannes Resin, Kristof Kraus, Johannes Bracher, Timo Dimitriadis, Veit Hagemeyer, Alexander I. Jordan, Sebastian Lerch, Kaleb Phipps, et al. Model diagnostics and forecast evaluation for quantiles. *Annual Review of Statistics and Its Application*, 10(1):597–621, 2023.

Varun Gupta, Christopher Jung, Georgy Noarov, Mallesh M. Pai, and Aaron Roth. Online multivalid learning: Means, moments, and prediction intervals. In *13th Innovations in Theoretical Computer Science Conference (ITCS 2022)*. Schloss Dagstuhl-Leibniz-Zentrum für Informatik, 2022.

Erfan Hajihashemi and Yanning Shen. Multi-model ensemble conformal prediction in dynamic environments. *Advances in Neural Information Processing Systems*, 37:118678–118700, 2024.

Thomas M Hamill and Stephen J Colucci. Verification of Eta–RSM short-range ensemble forecasts. *Monthly Weather Review*, 125(6):1312–1327, 1997.

Elad Hazan. Introduction to online convex optimization, 2019. Version 3, last revised 6 Aug 2023.

Lion Hirth and Inka Ziegenhagen. Balancing power and variable renewables: Three links. *Renewable and Sustainable Energy Reviews*, 50:1035–1051, 2015.

Tao Hong and Shu Fan. Probabilistic electric load forecasting: A tutorial review. *International Journal of Forecasting*, 32(3):914–938, 2016.

Dongjian Hu, Junxi Wu, Shu-Tao Xia, and Changliang Zou. Distribution-informed online conformal prediction. *arXiv preprint arXiv:2512.07770*, 2025.

Roger Koenker and Gilbert Bassett. Regression quantiles. *Econometrica*, 46(1):33–50, 1978.

Jordan Lekeufack, Anastasios N Angelopoulos, Andrea Bajcsy, Michael I Jordan, and Jitendra Malik. Conformal decision theory: Safe autonomous decisions from imperfect predictions. In *2024 IEEE International Conference on Robotics and Automation (ICRA)*, pages 11668–11675. IEEE, 2024.

Ruipu Li and Alexander Rodríguez. Neural conformal control for time series forecasting. In *Proceedings of the AAAI Conference on Artificial Intelligence*, volume 39, pages 18439–18447, 2025.

Yufeng Liu and Yichao Wu. Stepwise multiple quantile regression estimation using non-crossing constraints. *Statistics and its Interface*, 2(3):299–310, 2009.

Chelsea S Lutz, Mimi P Huynh, Monica Schroeder, Sophia Anyatonwu, F Scott Dahlgren, Gregory Danyluk,

Danielle Fernandez, Sharon K Greene, Nodar Kipshidze, Leann Liu, et al. Applying infectious disease forecasting to public health: a path forward using influenza forecasting examples. *BMC Public Health*, 19(1):1659, 2019.

Charles Marx, Volodymyr Kuleshov, and Stefano Ermon. Calibrated probabilistic forecasts for arbitrary sequences. *arXiv preprint arXiv:2409.19157*, 2024.

Georgy Noarov, Ramya Ramalingam, Aaron Roth, and Stephan Xie. High-dimensional prediction for sequential decision making. *arXiv preprint arXiv:2310.17651*, 2023.

Youngsuk Park, Danielle Maddix, François-Xavier Aubet, Kelvin Kan, Jan Gasthaus, and Yuyang Wang. Learning quantile functions without quantile crossing for distribution-free time series forecasting. In *Proceedings of the International Conference on Artificial Intelligence and Statistics*, pages 8127–8150. PMLR, 2022.

Juan Carlos Perdomo and Benjamin Recht. In defense of defensive forecasting. *arXiv preprint arXiv:2506.11848*, 2025.

Kent Quanrud and Daniel Khashabi. Online learning with adversarial delays. *Advances in Neural Information Processing Systems*, 28, 2015.

Adrian E. Raftery, Tilmann Gneiting, Fadoua Balabdaoui, and Michael Polakowski. Using Bayesian model averaging to calibrate forecast ensembles. *Monthly Weather Review*, 133(5):1155–1174, 2005.

Regelleistung. How does the balancing market work?, 2024. URL <https://www.regelleistung.net/en-us/Basics-of-balancing-services/How-does-the-balancing-market-work>. Accessed: 2025-09-01.

Aaron Rumack, Ryan J. Tibshirani, and Roni Rosenfeld. Recalibrating probabilistic forecasts of epidemics. *PLOS Computational Biology*, 18(12):e1010771, 2022.

Shai Shalev-Shwartz et al. Online learning and online convex optimization. *Foundations and Trends® in Machine Learning*, 4(2):107–194, 2012.

Huug van den Dool, Emily Becker, Li-Chuan Chen, and Qin Zhang. The probability anomaly correlation and calibration of probabilistic forecasts. *Weather and Forecasting*, 32(1):199–206, 2017.

Vladimir Vovk, Akimichi Takemura, and Glenn Shafer. Defensive forecasting. In *International Workshop on Artificial Intelligence and Statistics*, pages 365–372. PMLR, 2005.

Xiaoqian Wang and Rob J Hyndman. Online conformal inference for multi-step time series forecasting. *arXiv preprint arXiv:2410.13115*, 2024.

Zitong Yang, Emmanuel Candès, and Lihua Lei. Bellman conformal inference: Calibrating prediction intervals for time series. *arXiv preprint arXiv:2402.05203*, 2024.

Margaux Zaffran, Olivier Féron, Yannig Goude, Julie Josse, and Aymeric Dieuleveut. Adaptive conformal predictions for time series. In *Proceedings of the International Conference on Machine Learning*, 2022.

Zhiyu Zhang, Zhou Lu, and Heng Yang. The benefit of being Bayesian in online conformal prediction. *arXiv preprint arXiv:2410.02561*, 2024.

Martin Zinkevich. Online convex programming and generalized infinitesimal gradient ascent. In *Proceedings of the International Conference on Machine Learning*, pages 928–936, 2003.

A Distributional Inconsistency of Quantile Tracker

To demonstrate that running the Quantile Tracker separately for each quantile level cannot be used to solve calibration without crossings, we run the Quantile Tracker (using the learning rate heuristic described in Section 5) on the COVID-19 dataset from [Cramer et al. \(2022a\)](#). We focus on one-week-ahead forecasts, yielding 750 time series (15 forecasters \times 50 states). Figure 10 plots the fraction of time steps for each of these time series where at least one pair of quantiles is crossed. We say a crossing has occurred at time t if there exists quantile levels $\alpha < \beta$ with corresponding forecasts q_t^α and q_t^β such that $q_t^\alpha > q_t^\beta$. We observe that on average, the Quantile Tracker results in distributionally inconsistent quantiles at 87% of time steps, which is practically undesirable.

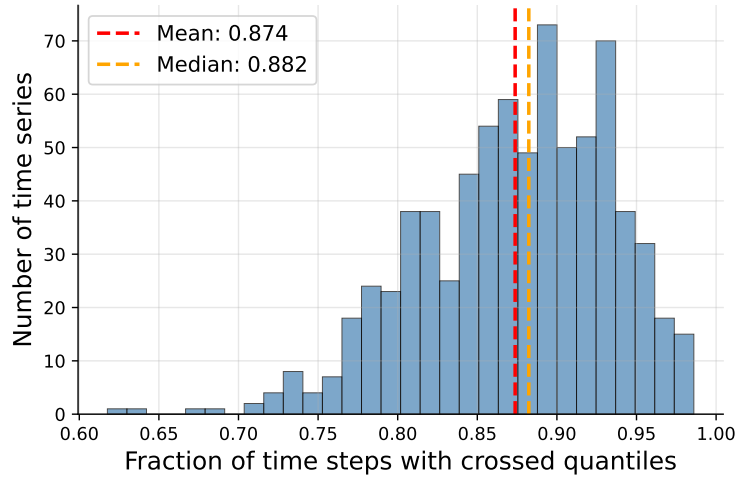


Figure 10: Histogram of fraction of time steps with crossings after applying the Quantile Tracker algorithm from [Angelopoulos et al. \(2023\)](#) to $h = 1$ week ahead quantile forecasts for COVID deaths in each of the 50 states, generated by 15 forecasting teams.

B Proofs for Sections 3 and 4

We prove results for the delayed feedback setting with a constant delay of $D \geq 0$. Results for the no-delay setting follow immediately by setting $D = 0$. The object of our analysis is lazy gradient descent with constant delay, which we now describe.

Lazy gradient descent with delay $D \geq 0$. Instead of observing y_t at time t , it is not observed until after we play our action at time $t + D$, at which point we take the gradient step based on that feedback. Let $\tilde{\theta}_1$ be an arbitrary initial value. For $t = 1, 2, \dots$, the lazy gradient descent algorithm with delay $D \geq 0$ is given by

$$\theta_t = \Pi_{C_t}(\tilde{\theta}_t) \tag{34}$$

$$\tilde{\theta}_{t+1} = \tilde{\theta}_t - \eta g_{t-D}(\theta_{t-D}), \tag{35}$$

where g_t is a subgradient of the loss function ℓ_t and we define $g_t(\theta_t) = \mathbf{0}$ for $t \leq 0$. By unrolling (35), we obtain $\tilde{\theta}_{t+1} = \tilde{\theta}_1 - \eta \sum_{s=1}^{t-D} g_s(\theta_s)$. This allows us to rewrite the whole algorithm as

$$\theta_{t+1} = \Pi_{C_{t+1}} \left(\tilde{\theta}_1 - \eta \sum_{s=1}^{t-D} g_s(\theta_s) \right), \quad (36)$$

where we adopt the convention that the summation from a to b is zero if $b \leq a$. In the following proofs, we will use this unrolled expression for θ_{t+1} when it is more convenient.

B.1 Proofs of constrained gradient equilibrium for lazy gradient descent with delay

The following result is the analogue of Proposition 2 of [Angelopoulos et al. \(2025\)](#) in the delayed feedback setting with constraints.

Proposition 11 (Average gradient bound for delayed lazy gradient descent). *If at each time t , the loss function ℓ_t is L -Lipschitz, then the iterates of lazy gradient descent with delay D satisfy*

$$\left\| \frac{1}{T} \sum_{t=1}^T g_t(\theta_t) \right\|_2 \leq \frac{\|\tilde{\theta}_1\|_2 + \|\tilde{\theta}_{T+1}\|_2}{\eta T} + \frac{DL}{T}. \quad (37)$$

Proof. Unrolling (35), we get

$$\tilde{\theta}_{T+1} = \tilde{\theta}_1 - \eta \sum_{t=1}^{T-D} g_t(\theta_t).$$

Adding and subtracting $-\eta \sum_{t=T-D+1}^T g_t(\theta_t)$ to the right side gives

$$\begin{aligned} \tilde{\theta}_{T+1} &= \tilde{\theta}_1 - \eta \sum_{t=1}^T g_t(\theta_t) + \eta \sum_{t=T-D+1}^T g_t(\theta_t) \\ \iff \eta \sum_{t=1}^T g_t(\theta_t) &= \tilde{\theta}_1 - \tilde{\theta}_{T+1} + \eta \sum_{t=T-D+1}^T g_t(\theta_t) \\ \iff \frac{1}{T} \sum_{t=1}^T g_t(\theta_t) &= \frac{\tilde{\theta}_1 - \tilde{\theta}_{T+1}}{\eta T} + \frac{1}{T} \sum_{t=T-D+1}^T g_t(\theta_t). \end{aligned}$$

By the triangle inequality,

$$\begin{aligned} \left\| \frac{1}{T} \sum_{t=1}^T g_t(\theta_t) \right\|_2 &\leq \frac{\|\tilde{\theta}_1\|_2 + \|\tilde{\theta}_{T+1}\|_2}{\eta T} + \frac{1}{T} \sum_{t=T-D+1}^T \|g_t(\theta_t)\|_2 \\ &\leq \frac{\|\tilde{\theta}_1\|_2 + \|\tilde{\theta}_{T+1}\|_2}{\eta T} + \frac{DL}{T}, \end{aligned}$$

where the last inequality comes from the Lipschitzness of the loss functions. \square

We will use this result to prove Proposition 6.

Proof of Proposition 6 (Lazy gradient descent with delay achieves GEQ under inward flow). We will upper bound $\|\tilde{\theta}_{T+1}\|_2$ by bounding $\|\tilde{\theta}_{T+1}\|_2^2$, following the proof structure from Proposition 5 of [Angelopoulos et al.](#)

(2025). Note that if $T < D$, no feedback is observed and $\|\tilde{\theta}_{T+1}\|_2 = \|\tilde{\theta}_T\|_2 = \dots = \|\tilde{\theta}_1\|_2$, which satisfies the stated bound. We now focus on the $T \geq D$ case. We begin by expanding the square:

$$\|\tilde{\theta}_{T+1}\|_2^2 = \|\tilde{\theta}_T\|_2^2 + \eta^2 \|g_{T-D}(\theta_{T-D})\|_2^2 - 2\eta \langle g_{T-D}(\theta_{T-D}), \tilde{\theta}_T \rangle. \quad (38)$$

By Lipschitzness, the second term of (38) is bounded by $\eta^2 L^2$. We now focus on bounding the third term of (38), which we rewrite as

$$-2\eta \langle g_{T-D}(\theta_{T-D}), \tilde{\theta}_T \rangle = -2\eta \langle g_{T-D}(\theta_{T-D}), \tilde{\theta}_{T-D} \rangle - 2\eta \langle g_{T-D}(\theta_{T-D}), \tilde{\theta}_T - \tilde{\theta}_{T-D} \rangle. \quad (39)$$

We start by bounding the first term of (39). By Lemma 4 below, inward flow implies $\langle g_t(\theta_t), \tilde{\theta}_t \rangle \geq \langle g_t(\theta_t), \theta_t \rangle$ at any time t . Thus, to upper bound $-\langle g_{T-D}(\theta_{T-D}), \tilde{\theta}_{T-D} \rangle$, it suffices to upper bound $-\langle g_{T-D}(\theta_{T-D}), \theta_{T-D} \rangle$. If $\|\theta_{T-D}\|_2 > h_{T-D}$, then the restorativity condition kicks in and we have

$$-\langle g_{T-D}(\theta_{T-D}), \theta_{T-D} \rangle \leq 0.$$

Otherwise, if $\|\theta_{T-D}\|_2 < h_{T-D}$, we have

$$\begin{aligned} -\langle g_{T-D}(\theta_{T-D}), \theta_{T-D} \rangle &\leq \|g_{T-D}(\theta_{T-D})\|_2 \|\theta_{T-D}\|_2 \\ &\leq L h_{T-D} \end{aligned}$$

where the first inequality is Cauchy-Schwarz and the second inequality comes from Lipschitzness and the condition on $\|\theta_{T-D}\|_2$. For ease of notation, we define $h_t = 0$ for $t \leq 0$. Combining the above cases, we have $-\langle g_{T-D}(\theta_{T-D}), \theta_{T-D} \rangle \leq \max(0, L h_{T-D}) = L h_{T-D}$.

The second term of (39) is the penalty we incur for delayed feedback. To bound it, note that

$$\begin{aligned} -\langle g_{T-D}(\theta_{T-D}), \tilde{\theta}_T - \tilde{\theta}_{T-D} \rangle &\leq \|g_{T-D}(\theta_{T-D})\|_2 \|\tilde{\theta}_T - \tilde{\theta}_{T-D}\|_2 \\ &\leq \|g_{T-D}(\theta_{T-D})\|_2 \left\| \eta \sum_{t=T-D}^{T-1} g_t(\theta_t) \right\|_2 \\ &\leq \eta \|g_{T-D}(\theta_{T-D})\|_2 \left(\sum_{t=T-D}^{T-1} \|g_t(\theta_t)\|_2 \right) \\ &\leq \eta D L^2, \end{aligned}$$

where the first inequality is Cauchy-Schwarz, the second inequality comes from the lazy gradient descent update rule from (35), the third inequality is an application of the triangle inequality, and the fourth inequality uses the Lipschitzness of the losses.

Inserting both of these bounds into (39), we get

$$-2\eta \langle g_{T-D}(\theta_{T-D}), \tilde{\theta}_T \rangle \leq 2\eta L h_{T-D} + 2\eta^2 D L^2.$$

We now return to our original goal of bounding $\|\tilde{\theta}_{T+1}\|_2$. Plugging these bounds back into (38), we obtain

$$\begin{aligned} \|\tilde{\theta}_{T+1}\|_2^2 &\leq \|\tilde{\theta}_T\|_2^2 + \eta^2 L^2 + 2\eta L h_{T-D} + 2\eta^2 D L^2 \\ &= \|\tilde{\theta}_T\|_2^2 + \eta^2 L^2 (2D + 1) + 2\eta L h_{T-D} \\ &\leq \|\tilde{\theta}_{D+1}\|_2^2 + \eta^2 L^2 (2D + 1)(T - D) + 2\eta L \sum_{t=1}^{T-D} h_t \\ &\leq \|\tilde{\theta}_1\|_2^2 + \eta^2 L^2 (2D + 1)T + 2\eta L \sum_{t=1}^{T-D} h_t, \end{aligned}$$

where the second inequality is obtained by iteratively applying the bound from the second line, and the third uses $T - D \leq T$ and $\|\tilde{\theta}_{t+1}\|_2 = \|\tilde{\theta}_1\|_2$ for $t \leq D$. Taking the square root gives the stated bound on $\|\tilde{\theta}_{T+1}\|_2$.

To get the bound on the ℓ_2 -norm of the average gradient, we first simplify the $\|\tilde{\theta}_{T+1}\|_2$ bound by observing that the nondecreasing property of h_t implies $\sum_{t=1}^{T-D} h_t \leq (T-D)h_{T-D} \leq Th_{T-D}$ and apply the fact that $\sqrt{a+b} \leq \sqrt{a} + \sqrt{b}$. We then invoke Proposition 11. \square

We now prove a fact used in the previous proof about the effect of projection on the inner product of an iterate and its gradient when inward flow is satisfied.

Lemma 4 (Gradient alignment). *If a loss ℓ (with gradient g) and a closed convex set $C \subseteq \mathbb{R}^m$ satisfy inward flow, then*

$$\langle \tilde{\theta}, g(\Pi_C(\tilde{\theta})) \rangle \geq \langle \Pi_C(\tilde{\theta}), g(\Pi_C(\tilde{\theta})) \rangle \quad \text{for any } \tilde{\theta} \text{ in } \mathbb{R}^m.$$

Proof. Let $\theta = \Pi_C(\tilde{\theta})$ be the projection of $\tilde{\theta}$ onto C and define the normal cone of a set A at point x as $N_A(x) := \{v : v^\top(x - y) \geq 0 \text{ for all } y \in A\}$. By definition of projection, there exists $v \in N_C(\theta)$ such that $\tilde{\theta} = \theta + v$. Thus, we can write

$$\langle \tilde{\theta}, g(\theta) \rangle = \langle \theta, g(\theta) \rangle + \langle v, g(\theta) \rangle. \quad (40)$$

We lower bound the second term by splitting into two cases. First, if $\tilde{\theta} \in C$, then $v = \mathbf{0}$ and thus $\langle v, g(\theta) \rangle = 0$. Second, if $\tilde{\theta} \notin C$, then θ will be on the boundary of C . By definition of inward flow, we know there exists $\varepsilon > 0$ such that $\theta - \varepsilon g(\theta) = \omega$ for some $\omega \in C$. We can thus write

$$\begin{aligned} \langle v, g(\theta) \rangle &= \frac{1}{\varepsilon} \langle v, \varepsilon g(\theta) \rangle \\ &= \frac{1}{\varepsilon} \langle v, \theta - \omega \rangle \\ &\geq 0 \quad \text{since } v \in N_C(\theta). \end{aligned}$$

Plugging $\langle v, g(\theta) \rangle \geq 0$ into (40) yields $\langle \tilde{\theta}, g(\theta) \rangle \geq \langle \theta, g(\theta) \rangle$. \square

B.2 Proofs of properties of MultiQT

Proof of Lemma 1 (Restorativity of MultiQT loss). Suppose $\|\theta_t\|_2 \geq h$ for some $h \geq \frac{R|\mathcal{A}|^{3/2}}{d_{\mathcal{A}}}$. This implies there exists $\alpha^* \in \mathcal{A}$ such that $|\theta_t^{\alpha^*}| \geq h/\sqrt{|\mathcal{A}|}$, because if all entries had magnitude strictly less than $h/\sqrt{|\mathcal{A}|}$, we would have $\|\theta_t\|_2 = \sqrt{\sum_{i=1}^{|\mathcal{A}|} (\theta_t^{\alpha_i})^2} < \sqrt{\sum_{i=1}^{|\mathcal{A}|} h^2/|\mathcal{A}|} = h$. We will make use of this fact after expanding the inner product:

$$\langle \theta_t, g_t(\theta_t) \rangle = \sum_{\alpha \in \mathcal{A}} \theta_t^\alpha (\text{cov}_t^\alpha - \alpha) \quad (41)$$

$$= \sum_{\alpha: \theta_t^\alpha < -R} \theta_t^\alpha (\text{cov}_t^\alpha - \alpha) + \sum_{\alpha: \theta_t^\alpha > R} \theta_t^\alpha (\text{cov}_t^\alpha - \alpha) + \sum_{\alpha: \theta_t^\alpha \in [-R, R]} \theta_t^\alpha (\text{cov}_t^\alpha - \alpha). \quad (42)$$

We will show that the first two sums must be positive and then argue that at least one of the sums must be large. In the first summation, since $\theta_t^\alpha < -R$, we must have $\text{cov}_t^\alpha = 0$, so $\text{cov}_t^\alpha - \alpha = -\alpha$ is negative; thus each summand is positive. In the second summation, since $\theta_t^\alpha > R$, we must have $\text{cov}_t^\alpha = 1$, so $\text{cov}_t^\alpha - \alpha = 1 - \alpha$ is positive; thus each of these summands is also positive. To see that at least one of the sums must be large, observe that since $|\theta_t^{\alpha^*}| \geq h/\sqrt{|\mathcal{A}|} \geq R$ (because $h \geq \frac{R|\mathcal{A}|^{3/2}}{d_{\mathcal{A}}}$), we know α^* must appear in the indices of

one of the first two summations. If α^* appears in the first summation, this means $\theta_t^{\alpha^*} < -h/\sqrt{|\mathcal{A}|}$, so the first summation can be lower bounded by $h\alpha^*/\sqrt{|\mathcal{A}|}$. If α^* appears in the second summation, this means $\theta_t^{\alpha^*} > h/\sqrt{|\mathcal{A}|}$, so the second summation can be lower bounded by $h(1 - \alpha^*)/\sqrt{|\mathcal{A}|}$. Combining, we conclude that the first two sums can be lower bounded as

$$\sum_{\alpha: \theta_t^\alpha < -R} \theta_t^\alpha (\text{cov}_t^\alpha - \alpha) + \sum_{\alpha: \theta_t^\alpha > R} \theta_t^\alpha (\text{cov}_t^\alpha - \alpha) \geq \frac{h \min(\alpha^*, 1 - \alpha^*)}{\sqrt{|\mathcal{A}|}} \geq \frac{hd_{\mathcal{A}}}{\sqrt{|\mathcal{A}|}}.$$

The third sum in (42) is lower bounded by $-R|\mathcal{A}|$ since $\text{cov}_t^\alpha - \alpha \in [-1, 1]$ for any $\alpha \in [0, 1]$. Plugging everything back into (42), we get

$$\langle \theta_t, g_t(\theta_t) \rangle \geq \frac{hd_{\mathcal{A}}}{\sqrt{|\mathcal{A}|}} - R|\mathcal{A}|.$$

Note that the right-hand side is non-negative for any $h \geq \frac{R|\mathcal{A}|^{3/2}}{d_{\mathcal{A}}}$. \square

Proof of Lemma 2 (Inward flow of MultiQT). We will prove a stronger condition that for any $\theta_t \in C_t$, where $C_t = \mathcal{K} - b_t$ is the MultiQT constraint set at time t , there exists $\beta > 0$ such that $\theta_t - \varepsilon g_t(\theta_t) \in C_t$ for all $\varepsilon < \beta$. In other words, we want to show that if we take a small enough step in the direction of the negative gradient starting from θ_t , the quantiles would remain uncrossed. We do this by first arguing that we do not have to worry about crossings between quantiles that are on the same side of y_t and then arguing that the quantiles that sandwich y_t must be separated by a positive distance, so we can keep them uncrossed by setting the step size to be half that distance, or smaller.

For $\varepsilon > 0$, define $\omega = \theta_t - \varepsilon g_t(\theta_t)$. For the quantile loss, each individual element of ω can be written as $\omega^\alpha = \theta_t^\alpha - \varepsilon(\text{cov}_t^\alpha - \alpha)$. We want to show that for sufficiently small ε , we must have $\omega \in C_t$. In other words, we must verify $\omega^{\alpha_i} + b_t^{\alpha_i} \leq \omega^{\alpha_{i+1}} + b_t^{\alpha_{i+1}}$ for $i = 1, \dots, |\mathcal{A}| - 1$.

First observe the following fact: For any pair of quantile levels $\alpha < \beta$, if $\text{cov}_t^\alpha = \text{cov}_t^\beta$, then $\omega^\alpha + b_t^\alpha \leq \omega^\beta + b_t^\beta$ for any $\varepsilon > 0$. To prove this fact, we will show $\omega^\beta + b_t^\beta - (\omega^\alpha + b_t^\alpha) \geq 0$.

$$\begin{aligned} \omega^\beta + b_t^\beta - (\omega^\alpha + b_t^\alpha) &= \theta_t^\beta - \varepsilon(\text{cov}_t^\beta - \beta) + b_t^\beta - [\theta_t^\alpha - \varepsilon(\text{cov}_t^\alpha - \alpha) + b_t^\alpha] \\ &= \theta_t^\beta + b_t^\beta - (\theta_t^\alpha + b_t^\alpha) - \varepsilon(\text{cov}_t^\beta - \text{cov}_t^\alpha - \beta + \alpha) \\ &\geq \theta_t^\beta + b_t^\beta - (\theta_t^\alpha + b_t^\alpha) \quad \text{since } \text{cov}_t^\alpha = \text{cov}_t^\beta \text{ and } \beta > \alpha \\ &\geq 0 \quad \text{since } \theta_t \in C_t. \end{aligned}$$

Since $\theta_t^{\alpha_1} + b_t^{\alpha_1} \leq \theta_t^{\alpha_2} + b_t^{\alpha_2} \leq \dots \leq \theta_t^{\alpha_{|\mathcal{A}|}} + b_t^{\alpha_{|\mathcal{A}|}}$, we know $0 \leq \text{cov}_t^{\alpha_1} \leq \text{cov}_t^{\alpha_2} \leq \dots \leq \text{cov}_t^{\alpha_{|\mathcal{A}|}} \leq 1$. Thus, there exists $B \in \{-1, 0, \dots, |\mathcal{A}|\}$ such that $\text{cov}_t^{\alpha_i} = 0$ for all $i \leq B$ and $\text{cov}_t^{\alpha_i} = 1$ for all $i > B$. For $i < B$ and $i > B$, we have $\omega^{\alpha_i} + b_t^{\alpha_i} \leq \omega^{\alpha_{i+1}} + b_t^{\alpha_{i+1}}$ for any $\varepsilon > 0$ by the fact above. The only case that remains is $i = B$. If $B = -1$ or $B = m$, this means cov_t^α was the same for all quantile levels, so we are done. Now consider the case where $0 \leq B \leq |\mathcal{A}| - 1$. Since $\text{cov}_t^{\alpha_B} = 0$ and $\text{cov}_t^{\alpha_{B+1}} = 1$, this implies y_t landed in $(\theta_t^{\alpha_B} + b_t^{\alpha_B}, \theta_t^{\alpha_{B+1}} + b_t^{\alpha_{B+1}}]$, which means $(\theta_t^{\alpha_{B+1}} + b_t^{\alpha_{B+1}}) - (\theta_t^{\alpha_B} + b_t^{\alpha_B}) > 0$. Informally, since $\theta_t^{\alpha_B}$ and $\theta_t^{\alpha_{B+1}}$ are separated by a positive amount, we can increase $\theta_t^{\alpha_B}$ by a little and decrease $\theta_t^{\alpha_{B+1}}$ by a little while still maintaining the ordering. Formally, choose any $\varepsilon < \delta$ where $\delta = \frac{\theta_t^{\alpha_{B+1}} + b_t^{\alpha_{B+1}} - (\theta_t^{\alpha_B} + b_t^{\alpha_B})}{2}$. Then,

$$\begin{aligned} \omega^{\alpha_{B+1}} + b_t^{\alpha_{B+1}} - (\omega^{\alpha_B} + b_t^{\alpha_B}) &= \theta_t^{\alpha_{B+1}} - \varepsilon(\text{cov}_t^{\alpha_{B+1}} - \alpha_{B+1}) + b_t^{\alpha_{B+1}} - [\theta_t^{\alpha_B} - \varepsilon(\text{cov}_t^{\alpha_B} - \alpha_B) + b_t^{\alpha_B}] \\ &\geq \theta_t^{\alpha_{B+1}} + b_t^{\alpha_{B+1}} - (\theta_t^{\alpha_B} + b_t^{\alpha_B}) - 2\varepsilon \\ &\geq 0, \end{aligned}$$

where the first inequality comes from noting $|\text{cov}_t^\alpha - \alpha| \leq 1$ for any $\alpha \in [0, 1]$ and the second inequality comes from the choice of ε . \square

B.3 Proofs of regret bound

Roadmap. The goal of this section is to prove Proposition 9, which gives the regret bound for MultiQT with delay $D \geq 0$. We start by analyzing the more general lazy mirror descent with delay procedure, then specialize the result to lazy gradient descent with delay starting from an arbitrary $\tilde{\theta}_1$. We finally apply this lazy mirror descent result to obtain a regret bound for MultiQT. Before defining lazy mirror descent, we must introduce a definition.

Definition 5. A function $f : C \rightarrow \mathbb{R}$ is σ -strongly convex over $C \subseteq \mathbb{R}^m$ with respect to the norm $\|\cdot\|$ if for all $x \in C$ we have

$$f(y) \geq f(x) + \langle g, y - x \rangle + \frac{\sigma}{2} \|y - x\|^2$$

for all subgradients g and points $y \in C$.

Lazy mirror descent with constant delay $D \geq 0$. Suppose $C_t \subseteq \mathbb{R}^m$ is the constraint set at time t , g_t is a subgradient of the loss function ℓ_t at time t , $\eta > 0$ is a learning rate, and the regularizer $\mathcal{R} : \mathbb{R}^m \rightarrow \mathbb{R}$ is σ -strongly convex over \mathbb{R}^m with respect to the norm $\|\cdot\|$. For $t = 0, 1, 2, \dots$, *lazy mirror descent with delay $D \geq 0$* obtains iterates via the rule

$$\theta_{t+1} = \operatorname{argmin}_{\theta \in C_{t+1}} \left\{ \left\langle \sum_{s=1}^{t-D} g_s(\theta_s), \theta \right\rangle + \frac{\mathcal{R}(\theta)}{\eta} \right\}. \quad (43)$$

In particular, this implies $\theta_1 = \operatorname{argmin}_{\theta \in C_1} \mathcal{R}(\theta)$. $D = 0$ corresponds to the standard non-delayed mirror descent where feedback for time t becomes available before θ_{t+1} is chosen. The next proposition says that lazy gradient descent (with delay) is a special case of lazy mirror descent (with delay).

Proposition 12. *The iterates of lazy gradient descent starting from initialization $\tilde{\theta}_1$ are equivalent to the iterates of lazy mirror descent with regularizer $\mathcal{R}(\theta) = \|\theta - \tilde{\theta}_1\|_2^2/2$, which is 1-strongly convex with respect to $\|\cdot\|_2$. This is true for any feedback delay $D \geq 0$.*

Proof. The unrolled expression of lazy gradient descent with delay from (36) tells us

$$\begin{aligned} \theta_{t+1} &= \operatorname{argmin}_{\theta \in C_{t+1}} \frac{1}{2} \left\| \theta - \tilde{\theta}_1 + \eta \sum_{s=1}^{t-D} g_s(\theta_s) \right\|_2^2 \\ &= \operatorname{argmin}_{\theta \in C_{t+1}} \left\{ \left\langle \sum_{s=1}^{t-D} g_s(\theta_s), \theta \right\rangle + \frac{1}{2\eta} \|\theta - \tilde{\theta}_1\|_2^2 \right\}, \end{aligned}$$

where the second line comes from expanding the square, removing terms not containing θ , and dividing by η . This expression is exactly equivalent to the lazy mirror descent with delay update from (43) with the stated regularizer. To see that $\mathcal{R}(\theta) = \|\theta - \tilde{\theta}_1\|_2^2/2$ is 1-strongly convex with respect to $\|\cdot\|_2$, observe that for any θ and θ' , we have

$$\begin{aligned} \mathcal{R}(\theta) &= \frac{1}{2} \|\theta - \tilde{\theta}_1\|_2^2 \\ &= \frac{1}{2} \|(\theta' - \tilde{\theta}_1) + (\theta - \theta')\|_2^2 \\ &= \frac{1}{2} \|\theta' - \tilde{\theta}_1\|_2^2 + \langle \theta' - \tilde{\theta}_1, \theta - \theta' \rangle + \frac{1}{2} \|\theta - \theta'\|_2^2 \\ &= \mathcal{R}(\theta') + \langle \nabla \mathcal{R}(\theta'), \theta - \theta' \rangle + \frac{1}{2} \|\theta - \theta'\|_2^2, \end{aligned}$$

where the final inequality uses $\nabla \mathcal{R}(\theta) = \theta - \tilde{\theta}_1$. \square

We thus focus on obtaining a regret bound for lazy mirror descent, as this will imply a regret bound for lazy gradient descent, of which MultiQT is an instance. The following result is a special case of Theorem A.5 of [Quanrud and Khashabi \(2015\)](#), which provides a regret bound for lazy mirror descent with non-constant delays. For completeness, we state and prove the result for the *constant* delay setting, which simplifies the proof from [Quanrud and Khashabi \(2015\)](#). We also write the result to more explicitly allow and account for time-varying constraint sets.

Theorem 2 (Regret bound of lazy mirror descent with delay). *Suppose the regularizer \mathcal{R} is σ -strongly convex with respect to the norm $\|\cdot\|$ and, at each time t , the loss function ℓ_t is L -Lipschitz (that is, $\|g_t(\theta)\|_* \leq L$ for all θ).⁵ Let $C = \bigcap_{t=1}^{T+D+1} C_t$ be the intersection of constraint sets over time. Then the iterates of lazy mirror descent with constant delay $D \geq 0$ satisfy*

$$\frac{1}{T} \sum_{t=1}^T \ell_t(\theta_t) - \frac{1}{T} \sum_{t=1}^T \ell_t(u) \leq \frac{\mathcal{R}(u)}{\eta T} - \frac{\min_{\theta \in C} \mathcal{R}(\theta)}{\eta T} + \frac{2\eta L^2(D+1)}{\sigma} \quad \text{for all } u \in C.$$

Proof. Convexity tells us that $\ell_t(u) \geq \ell_t(\theta_t) + \langle g_t(\theta_t), u - \theta_t \rangle$. Rearranging and summing over t gives

$$\begin{aligned} \sum_{t=1}^T (\ell_t(\theta_t) - \ell_t(u)) &\leq \sum_{t=1}^T \langle g_t(\theta_t), \theta_t - u \rangle \\ &= \sum_{t=1}^T \langle g_t(\theta_t), \theta_{t+D+1} - u \rangle + \sum_{t=1}^T \langle g_t(\theta_t), \theta_t - \theta_{t+D+1} \rangle. \end{aligned} \quad (44)$$

We will bound the first summation in (44) using standard arguments for lazy mirror descent. We claim that for any T ,

$$\sum_{t=1}^T \langle g_t(\theta_t), \theta_{t+D+1} \rangle + \frac{\mathcal{R}(\theta_1)}{\eta} \leq \sum_{t=1}^T \langle g_t(\theta_t), u \rangle + \frac{\mathcal{R}(u)}{\eta} \quad \text{for all } u \in C. \quad (45)$$

We proceed by induction. For the base case, consider $T = 0$. The claim reduces to $\mathcal{R}(\theta_1) \leq \mathcal{R}(u)$ for all $u \in C$, which is true by definition of lazy mirror descent. Now assume the statement is true for $T - 1$, i.e.,

$$\sum_{t=1}^{T-1} \langle g_t, \theta_{t+D+1} \rangle + \frac{\mathcal{R}(\theta_1)}{\eta} \leq \sum_{t=1}^{T-1} \langle g_t, u \rangle + \frac{\mathcal{R}(u)}{\eta} \quad \text{for all } u \in C. \quad (46)$$

We will show the statement must hold for T . Observe that

$$\begin{aligned} \sum_{t=1}^T \langle g_t(\theta_t), \theta_{t+D+1} \rangle + \frac{\mathcal{R}(\theta_1)}{\eta} &= \langle g_T(\theta_T), \theta_{T+D+1} \rangle + \sum_{t=1}^{T-1} \langle g_t(\theta_t), \theta_{t+D+1} \rangle + \frac{\mathcal{R}(\theta_1)}{\eta} \\ &\leq \langle g_T(\theta_T), \theta_{T+D+1} \rangle + \sum_{t=1}^{T-1} \langle g_t(\theta_t), \theta_{T+D+1} \rangle + \frac{\mathcal{R}(\theta_{T+D+1})}{\eta} \\ &= \sum_{t=1}^T \langle g_t(\theta_t), \theta_{T+D+1} \rangle + \frac{\mathcal{R}(\theta_{T+D+1})}{\eta} \\ &\leq \sum_{t=1}^T \langle g_t(\theta_t), u \rangle + \frac{\mathcal{R}(u)}{\eta} \quad \text{for all } u \in C, \end{aligned}$$

⁵For the sake of generality, we state the result in terms of an arbitrary norm $\|\cdot\|$, which requires the Lipschitzness condition to be defined in terms of the corresponding dual norm $\|\cdot\|_*$. Aside from this theorem, Lipschitzness should be assumed to be in terms of $\|\cdot\|_2$ even if it is not explicitly stated.

where the first inequality comes from applying (46) with $u = \theta_{T+D+1}$ and the second inequality comes from the definition of θ_{T+D+1} as the minimizer over C_{T+D+1} , and $C_{T+D+1} \subseteq C$. We have thus shown that (45) holds for all T . Rearranging (45), we get the following upper bound on the first summation in (44):

$$\sum_{t=1}^T \langle g_t(\theta_t), \theta_{t+D+1} - u \rangle \leq \frac{\mathcal{R}(u)}{\eta} - \frac{\mathcal{R}(\theta_1)}{\eta}. \quad (47)$$

The second summation in (44) is the delay term. We bound each summand by first applying the triangle inequality, then using the standard procedure from undelayed lazy mirror descent for bounding $\|\theta_t - \theta_{t+1}\|$. Observe that

$$\langle g_t(\theta_t), \theta_t - \theta_{t+D+1} \rangle \leq \|g_t\|_* \|\theta_t - \theta_{t+D+1}\| \leq L \|\theta_t - \theta_{t+D+1}\| \leq L \sum_{s=t}^{t+D} \|\theta_s - \theta_{s+1}\|, \quad (48)$$

where the first inequality uses Cauchy-Schwarz, the second inequality invokes Lipschitzness of the loss function, and the third inequality applies the triangle inequality. We now focus on bounding a single $\|\theta_s - \theta_{s+1}\|$ term, which we will do by proving two inequalities that can be chained together to obtain a bound. Define $\psi_t(\theta) = \eta \sum_{s=1}^{t-D-1} \langle g_s(\theta_s), \theta \rangle + \mathcal{R}(\theta)$ for each time t , so $\theta_t = \operatorname{argmin}_{\theta \in C_t} \psi_t(\theta)$. Since \mathcal{R} is σ -strongly convex, ψ_t is also σ -strongly convex. Applying strong convexity to ψ_{s+1} and then invoking the first order optimality condition for θ_{s+1} yields

$$\psi_{s+1}(\theta_s) \geq \psi_{s+1}(\theta_{s+1}) + \langle \nabla \psi_{s+1}(\theta_{s+1}), \theta_s - \theta_{s+1} \rangle + \frac{\sigma}{2} \|\theta_s - \theta_{s+1}\|^2 \geq \psi_{s+1}(\theta_{s+1}) + \frac{\sigma}{2} \|\theta_s - \theta_{s+1}\|^2,$$

which can be rearranged to get $\psi_{s+1}(\theta_{s+1}) - \psi_{s+1}(\theta_s) \leq -\frac{\sigma}{2} \|\theta_s - \theta_{s+1}\|^2$. This is the first inequality we need. To get the second inequality, observe that by definition of ψ_t , we have

$$\begin{aligned} \psi_{s+1}(\theta_{s+1}) - \psi_{s+1}(\theta_s) &= (\psi_s(\theta_{s+1}) + \eta \langle g_{s-D}, \theta_{s+1} \rangle) - (\psi_s(\theta_s) + \eta \langle g_{s-D}, \theta_s \rangle) \\ &= \psi_s(\theta_{s+1}) - \psi_s(\theta_s) + \eta \langle g_{s-D}, \theta_{s+1} - \theta_s \rangle \\ &\geq \eta \langle g_{s-D}, \theta_{s+1} - \theta_s \rangle, \end{aligned}$$

where the inequality comes from ψ_s being the minimizer of ψ_s , so $\psi_s(\theta_{s+1}) \geq \psi_s(\theta_s)$. Combining this with the first inequality, we get

$$\eta \langle g_{s-D}, \theta_{s+1} - \theta_s \rangle \leq \psi_{s+1}(\theta_{s+1}) - \psi_{s+1}(\theta_s) \leq -\frac{\sigma}{2} \|\theta_s - \theta_{s+1}\|^2.$$

Multiplying through by -1 yields then applying Cauchy-Schwarz yields

$$\frac{\sigma}{2} \|\theta_s - \theta_{s+1}\|^2 \leq -\eta \langle g_{s-D}, \theta_{s+1} - \theta_s \rangle \leq \eta \|g_{s-D}\|_* \|\theta_{s+1} - \theta_s\| \leq \eta L \|\theta_{s+1} - \theta_s\|,$$

and dividing both sides by $\frac{\sigma}{2} \|\theta_{s+1} - \theta_s\|$ gives $\|\theta_{s+1} - \theta_s\| \leq \frac{2\eta L}{\sigma}$. Plugging this bound back into (48) gives

$$\langle g_t(\theta_t), \theta_t - \theta_{t+D+1} \rangle \leq \frac{2\eta L^2(D+1)}{\sigma},$$

so the second summation of (44) is upper bounded as

$$\sum_{t=1}^T \langle g_t(\theta_t), \theta_t - \theta_{t+D+1} \rangle \leq \frac{2\eta L^2(D+1)T}{\sigma}. \quad (49)$$

Plugging the bounds given in (47) and (49) into (44) and dividing by T yields the stated bound. \square

Armed with this result, we can state a general regret bound for lazy gradient descent starting from an arbitrary hidden iterate value $\tilde{\theta}_1$.

Corollary 2 (Regret bound of lazy gradient descent with delay). *Suppose at each time t the loss function ℓ_t is L -Lipschitz with respect to $\|\cdot\|_2$ and let $C = \bigcap_{t=1}^{T+D+1} C_t$ be the intersection of all constraint sets over time. Then the iterates of lazy gradient descent with constant delay $D \geq 0$ starting from $\tilde{\theta}_1 \in C$ satisfy*

$$\frac{1}{T} \sum_{t=1}^T \ell_t(\theta_t) - \frac{1}{T} \sum_{t=1}^T \ell_t(u) \leq \frac{\|u - \tilde{\theta}_1\|_2^2}{2\eta T} + 2\eta L^2(D+1) \quad \text{for all } u \in C.$$

Proof. This follows directly from Proposition 12 and Theorem 2. \square

We are now almost ready to prove the MultiQT regret bound from Proposition 8. A final result is needed to bound the ℓ_2 -norm of the optimal comparator in the MultiQT setting.

Lemma 5 (Optimal comparator for MultiQT). *Let ℓ_t be the MultiQT loss at time t , as defined in (11), and define $\theta^* \in \operatorname{argmin}_{\theta \in C} \sum_{t=1}^T \ell_t(\theta)$ to be an optimal fixed offset in hindsight that results in ordered forecasts at every time step when added to the base forecasts. If $|y_t - b_t^\alpha| \leq R$ for all $\alpha \in \mathcal{A}$ and times t , we must have*

$$\|\theta^*\|_2^2 \leq R^2 |\mathcal{A}|. \quad (50)$$

Proof. In brief, θ^* is the vector of empirical quantiles of the residuals, which is guaranteed to lie within a box with the stated norm bound. We now formally show this. For the purposes of this proof, it is useful to introduce some notation. Recall that we defined the quantile loss (for level $\alpha \in [0, 1]$) as taking two arguments:

$$\rho_\alpha(\hat{y}, y) = \begin{cases} \alpha|y - \hat{y}| & \text{if } y - \hat{y} \geq 0, \\ (1 - \alpha)|y - \hat{y}| & \text{otherwise.} \end{cases}$$

We now define a single-argument quantile loss

$$\varrho_\alpha(x) = \begin{cases} \alpha|x| & \text{if } x \geq 0, \\ (1 - \alpha)|x| & \text{if } x < 0. \end{cases}$$

Observe that $\rho_\alpha(\hat{y}, y) = \varrho_\alpha(y - \hat{y})$. For $\alpha \in \mathcal{A}$, let $X_t^\alpha := y_t - b_t^\alpha$. By assumption, $X_t^\alpha \in [-R, R]$ for all t . The MultiQT loss from (11) can be expressed in terms of the single-argument quantile loss ϱ_α and X_t^α :

$$\ell_t(\theta_t) = \sum_{\alpha \in \mathcal{A}} \varrho_\alpha(X_t^\alpha - \theta_t^\alpha)$$

Now fix an $\alpha \in \mathcal{A}$. Holding all other coordinates fixed, the α -coordinate of any optimizer $\theta^* \in \operatorname{argmin}_{\theta \in C} \sum_{t=1}^T \ell_t(\theta)$ solves

$$\theta^{*,\alpha} \in \operatorname{argmin}_{\theta \in \mathbb{R}} \sum_{t=1}^T \varrho_\alpha(X_t^\alpha - \theta).$$

It follows that $\theta^{*,\alpha}$ must be an empirical α -quantile of $\{X_t\}_{t=1}^T$ because the optimality condition requires

$$0 \in \partial_\theta \sum_{t=1}^T \varrho_\alpha(X_t^\alpha - \theta) \iff \#\{t : X_t^\alpha < \theta\} \leq \alpha T \leq \#\{t : X_t^\alpha \leq \theta\}.$$

Thus, $\theta^{*,\alpha}$ is as an empirical α -quantile of $\{X_t^\alpha\}_{t=1}^T$. Every empirical quantile lies between the sample minimum and maximum, so $|\theta^{*,\alpha}| \leq \max_t |X_t^\alpha| \leq R$. Since this is true for all $\alpha \in \mathcal{A}$, we have

$$\|\theta^*\|_2^2 = \sum_{\alpha \in \mathcal{A}} (\theta^{*,\alpha})^2 \leq \sum_{\alpha \in \mathcal{A}} R^2 = R^2 |\mathcal{A}|.$$

□

We can now prove the regret bound for MultiQT with delay stated in Proposition 9.

Proof of Proposition 9. Let $\theta^* \in \operatorname{argmin}_{\theta \in \mathcal{C}} \sum_{t=1}^T \ell_t(\theta)$ denote the optimal comparator. Then, for any $\theta \in \mathcal{C}$ we have

$$\begin{aligned} \max_{\theta \in \mathcal{C}} \left(\frac{1}{T} \sum_{t=1}^T \ell_t(\theta_t) - \frac{1}{T} \sum_{t=1}^T \ell_t(\theta) \right) &\leq \frac{1}{T} \sum_{t=1}^T \ell_t(\theta_t) - \frac{1}{T} \sum_{t=1}^T \ell_t(\theta^*) \\ &\leq \frac{\|\theta^* - \tilde{\theta}_1\|_2^2}{2\eta T} + 2\eta |\mathcal{A}|(D+1) \\ &\leq \frac{R^2 |\mathcal{A}|}{2\eta T} + 2\eta |\mathcal{A}|(D+1), \end{aligned}$$

where the second inequality follows from Corollary 2 and the $\sqrt{|\mathcal{A}|}$ -Lipschitzness of the MultiQT loss, and the third inequality applies Lemma 5 and the assumption that $\tilde{\theta}_1 = \mathbf{0}$. □

B.4 Auxiliary proofs

The following result is used in Section 2.2 to express the projection step of MultiQT as a simple isotonic regression.

Lemma 6 (Projection commutes with translations). *Let $C \subseteq \mathbb{R}^m$ be a closed convex set and let $\Pi_C(x) := \operatorname{argmin}_{y \in C} \|x - y\|_2^2$ denote the projection of x onto C . For any $x, b \in \mathbb{R}^m$, we have*

$$\Pi_C(x + b) = \Pi_{C-b}(x) + b,$$

where $C - b := \{z \in \mathbb{R}^m : z + b \in C\}$ is the translation of C by $-b$.

Proof. Consider the two optimization problems

$$(I) \quad \min_{y \in C} \|(x + b) - y\|_2^2 \quad \text{and} \quad (II) \quad \min_{z \in C-b} \|x - z\|_2^2.$$

Define the change of variables $z = y - b$. Then (II) can be rewritten as $\min_{y-b \in C-b} \|x - (y - b)\|_2^2 \iff \min_{y \in C} \|(x + b) - y\|_2^2$, which is exactly equal to (I). Let y^* be the minimizer of (I), which is unique by the convexity of C . By the equivalence of (I) and (II), the minimizer of (II) is $z^* = y^* - b$. By definition, $\Pi_C(x + b) = y^*$ and $\Pi_{C-b}(x) = z^*$, and the desired result follows. □

C Negative Results for Some Alternative Methods

Recall that Proposition 2 says that running the Quantile Tracker for multiple quantile levels and post hoc ordering the iterates before presenting them (via either sorting or isotonic regression) does not achieve distribution-free calibration. We prove this by constructing a counterexample.

Proof of Proposition 2 (Post hoc ordering of Quantile Tracker fails). We define \mathcal{A} , y_t , $t = 1, 2, \dots$, and b_t , $t = 1, 2, \dots$ that provides a counterexample for both $m = \text{SORT}$ and $m = \Pi_{\mathcal{K}}$. We consider the no base forecaster setting ($b_t = \mathbf{0}$ for all t). This implies $q_t^\alpha = \theta_t^\alpha$, so below we will directly reference q_t^α instead of θ_t^α . For simplicity, we consider only two quantile levels, so $\mathcal{A} = \{\alpha, \beta\}$. For concreteness, let $\alpha = 0.5$ and $\beta = 0.75$. We now construct a sequence of y_t with a crossing event at a non-vanishing fraction of time steps, which will result in the incorrect long-run coverage after applying m . Recall that q_t^α denotes the α -level Quantile Tracker forecast at time t and \hat{q}_t^α denotes the value we output as our α -level forecast after applying the ordering function m .

First, consider $m = \text{SORT}$. We initialize our guess for both quantiles to the same value, and without loss of generality we will assume this value is zero ($q_1^\alpha = q_1^\beta = 0$). We then observe the following sequence of y_t values (visualized in Figure 11): y_1 lands above both forecasts, causing both forecasts to increase and become separated by a positive gap. y_2 lands in this gap, causing the α -level forecast to decrease and the β -level forecast to increase, so the quantiles are now crossed. y_3 lands in between the two crossed quantiles. y_4 through y_8 are a sequence of values that cause the forecasts to reset to the starting point of zero at time $t = 9$, at which point we repeat the entire sequence ad infinitum. Of the eight timesteps in the subsequence, q_t^α covers y_t four times, yielding the desired coverage of 0.5. Similarly, q_t^β covers y_t six times out of eight, yielding the desired coverage of 0.75. However, due to the crossing at $t = 3$, the sorted quantiles \hat{q}_t^α and \hat{q}_t^β yield coverages of $3/8$ and $7/8$, respectively.

Now consider $m = \Pi_{\mathcal{K}}$, corresponding to isotonic regression. By the Pool Adjacent Violators Algorithm (PAVA) (Barlow et al., 1972), we know that isotonic regression maps any pair of crossed quantiles to the same value. If we use the same sequence of y_t 's and initial values q_1^α and q_1^β as in the previous paragraph, the only change that occurs is we use isotonic regression instead of sorting at $t = 3$. Rather than swapping the coverage events at $t = 3$, applying isotonic regression will cause one of the coverage events in that column to flip: Let \bar{q} denote the common value that q_3^α and q_3^β are mapped to after applying isotonic regression. If $y_3 \leq \bar{q}$, then the coverage indicators for the ordered forecasts at $t = 3$ will both be one (denoted by \checkmark). Conversely, if $y_3 > \bar{q}$, then both will be zero (denoted by \times). In either case, one of the quantile forecast sequences will fail to achieve the desired coverage.

□

Recall that Proposition 4 says that projected gradient descent does not solve the calibration with crossings problem. We prove this by constructing a counterexample.

Proof of Proposition 4 (Projected gradient descent fails). We construct a counterexample where projected gradient descent fails to achieve calibration. Suppose we are tracking quantiles $\alpha, \beta \in (0, 1)$ where $\alpha + \beta = 0.5$ and $\alpha < \beta$. Assume there is no base forecaster, so $b_t = \mathbf{0}$ for all t , which implies $\theta_t^\tau = q_t^\tau$ for $\tau \in \{\alpha, \beta\}$. We initialize $\theta_1^\alpha = \theta_1^\beta = q$ for some $q \in \mathbb{R}$. We observe $y_1 > q$, so $\tilde{\theta}_2^\alpha = q + \eta\alpha$ and $\tilde{\theta}_2^\beta = q + \eta\beta$. Since $\alpha < \beta$, the quantiles are uncrossed, so we have $\theta_2^\alpha = \tilde{\theta}_2^\alpha$ and $\theta_2^\beta = \tilde{\theta}_2^\beta$. We then observe $y_2 \in (\theta_2^\alpha, \theta_2^\beta]$, so the hidden iterates update to $\tilde{\theta}_3^\alpha = q + 2\eta\alpha$ and $\tilde{\theta}_3^\beta = q + \eta\beta - \eta(1 - \beta) = q + \eta(2\beta - 1)$. Since $\alpha > \beta - 0.5$, we have $\tilde{\theta}_3^\alpha > \tilde{\theta}_3^\beta$, so a crossing has occurred. By the Pool Adjacent Violators Algorithm (Ayer et al., 1955), running isotonic regression causes us to set $\theta_3^\alpha = \theta_3^\beta = \frac{\tilde{\theta}_3^\alpha + \tilde{\theta}_3^\beta}{2}$. This further simplifies to $\frac{\tilde{\theta}_3^\alpha + \tilde{\theta}_3^\beta}{2} = q + \frac{2\eta\alpha + \eta(2\beta - 1)}{2} = q + \frac{\eta(2(\alpha + \beta) - 1)}{2} = q$, where the last equality follows from $\alpha + \beta = 0.5$. This puts us back to the starting point from $t = 1$. Repeating this sequence of y_t 's, we get that the sequence of θ^α 's will achieve a coverage of 0.5 and the θ^β 's achieve a coverage of 1 (regardless of what coverage levels α and β were chosen to be). □

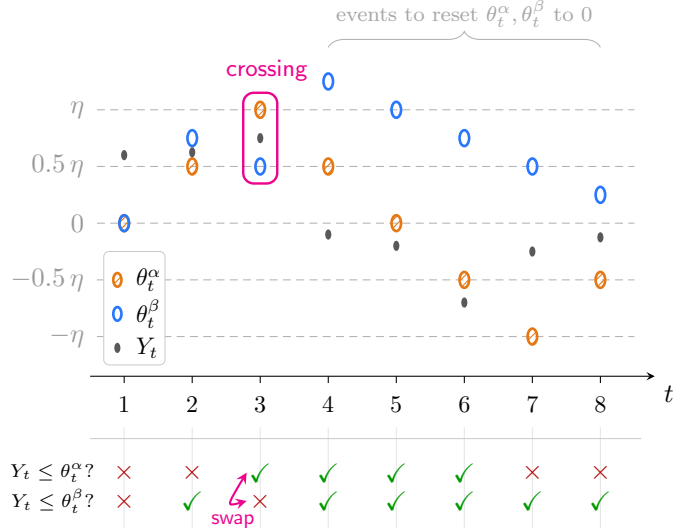


Figure 11: An example where *sorted* Quantile Tracker fails to achieve the correct coverage with two quantile levels, $\alpha = 0.5$ and $\beta = 0.75$. The sequence of y_t 's relative to θ_t^α and θ_t^β is (1) above both, (2) in between, (3) in between the crossed quantiles, (4-6) below both, (7-8) in between both. Both forecasts are initialized to zero at time $t = 1$ and return to zero at time $t = 9$, at which point the sequence of y_t 's is repeated. The coverage events are marked below with \checkmark and \times . Averaging across each row, we see that q_t^α achieves a coverage of 0.5 and q_t^β achieves a coverage of 0.75, as desired. However, applying sorting means that the coverage events at $t = 3$ will be swapped, leading the sorted iterates to achieve the incorrect coverage.

The next negative result highlights the importance of using projection to enforce the ordering constraints, as it shows that replacing the projection with sorting does not achieve distribution-free calibration.

Proposition 13 (MultiQT with sorting fails). *Let $q_t, t = 1, 2, \dots$ be forecasts obtained by replacing the MultiQT projection in (6) with $q_t = \text{SORT}(b_t + \tilde{\theta}_t)$. Then there exists a set of levels \mathcal{A} and sequence of (y_t, b_t) with $|y_t - b_t^\alpha| < R$ for all α and t (for some $R > 0$) such that for some quantile level $\alpha \in \mathcal{A}$, we have $\lim_{T \rightarrow \infty} \frac{1}{T} \sum_{t=1}^T \mathbb{1}\{y_t \leq q_t^\alpha\} \neq \alpha$.*

Proof. Suppose we are tracking two quantiles $\alpha, \beta \in (0, 1)$ where $\alpha < \beta$ and the base forecaster is $b_t = \mathbf{0}$ for all t , so $\theta_t^\tau = q_t^\tau$ for $\tau \in \{\alpha, \beta\}$. Suppose $\tilde{\theta}_t = q_t$ is uncrossed to start, but at time s , the true value y_s lands in $[q_s^\alpha, q_s^\beta]$ and the quantiles become crossed — that is, $\tilde{\theta}_{s+1}^\alpha > \tilde{\theta}_{s+1}^\beta$. To get q_{s+1} , we sort $\tilde{\theta}_{s+1}$, yielding $q_{s+1}^\alpha = \tilde{\theta}_{s+1}^\beta$ and $q_{s+1}^\beta = \tilde{\theta}_{s+1}^\alpha$. Now suppose y_{s+1} lands in between q_{s+1}^α and q_{s+1}^β . By the MultiQT update rule from (5), we have to increase $\tilde{\theta}_{s+1}^\beta$ and decrease $\tilde{\theta}_{s+1}^\alpha$, which worsens the crossing. This can be repeated ad finitum, causing $\tilde{\theta}_t^\beta$ and $\tilde{\theta}_t^\alpha$ to diverge to $+\infty$ and $-\infty$, respectively, so q_t^α (which equals $\tilde{\theta}_t^\beta$ for all $t > s$) will have coverage approaching one and q_t^β (which equals $\tilde{\theta}_t^\alpha$ for all $t > s$) will have coverage approaching zero. \square

We remark that the key ingredient of this counterexample is that, when the quantiles are crossed, the remapped quantiles have a *positive gap* and the true value label is able to land in between and cause the hidden iterates to be updated in different directions. This is possible for $q_t = \text{SORT}(b_t + \tilde{\theta}_t)$ but not $q_t = \Pi_{\mathcal{K}}(b_t + \tilde{\theta}_t)$, which maps crossed quantiles to the same value.

The next result highlights the importance of not only projection, but specifically projection to the

(b_t -shifted) isotonic cone; modifying the constraint set to induce strictly separated quantiles (instead of simply non-crossing) fails to achieve guaranteed calibration.

Proposition 14 (MultiQT with projection to strictly monotonic cone fails). *Let $\mathcal{K}_\varepsilon = \{x \in \mathbb{R}^{|\mathcal{A}|} \mid x_i + \varepsilon \leq x_{i+1} \text{ for } i = 1, 2, \dots, |\mathcal{A}| - 1\}$ for $\varepsilon > 0$ be the set of ordered vectors with ε -separated entries. Let $q_t, t = 1, 2, \dots$ be forecasts obtained by replacing the MultiQT projection in (6) with $q_t = \Pi_{\mathcal{K}_\varepsilon}(b_t + \tilde{\theta}_t)$.⁶ Then there exists a set of levels \mathcal{A} and sequence of (y_t, b_t) with $|y_t - b_t^\alpha| < R$ for all α and t (for some $R > 0$) such that for some quantile level $\alpha \in \mathcal{A}$, we have $\lim_{T \rightarrow \infty} \frac{1}{T} \sum_{t=1}^T \mathbb{1}\{y_t \leq q_t^\alpha\} \neq \alpha$.*

Proof. We adapt the construction from the proof of Proposition 13. Consider the same sequence of base forecasts and outcomes, and suppose that at some time s the hidden iterates become crossed. Under projection onto \mathcal{K}_ε , the projected forecasts at time $s + 1$ satisfy $q_{s+1}^\beta - q_{s+1}^\alpha \geq \varepsilon$, creating a strictly positive gap. By choosing y_{s+1} to lie in this interval and repeating this choice thereafter, the MultiQT update increases the larger hidden iterate and decreases the smaller one, causing their separation to grow over time. As a result, the coverage of one quantile converges to one and that of the other converges to zero. \square

We remark on the connection between the counterexample in the proof and the violation of inward flow induced by the ε -separated constraint set. The phenomenon that y_t can land in the gap between the two projected quantiles and induce a negative gradient that updates the entries of $\tilde{\theta}$ in different directions is possible because inward flow is not satisfied.

D Proofs of $1/T$ Rate

Proof of Lemma 3 (Point forecasts imply bounded projection distance). Our proof has two steps: First, we will show that if the base forecaster is level agnostic, the entries of $\tilde{\theta}$ can only get so crossed, specifically, $\tilde{\theta}_t^{\alpha_i} - \tilde{\theta}_t^{\alpha_{i+1}} \leq \eta$ for all $i = 1, 2, \dots, |\mathcal{A}| - 1$. We then bound $\|\tilde{\theta} - \Pi_{\mathcal{K}}(\tilde{\theta})\|_2$ for any $\tilde{\theta}$ satisfying this crossing bound to obtain the desired result.

Before beginning with the first step, we make the following observation about the MultiQT iterates when the base forecasts are level-agnostic: *When $b_t = k_t \mathbf{1}$ for some $k_t \in \mathbb{R}$, the played iterate is simply the isotonic regression of the hidden iterate* — that is,

$$\theta_t = \Pi_{\mathcal{K}}(\tilde{\theta}_t).$$

To see why, recall that in Section 2.2, we established that two equivalent definitions of q_t are $q_t = k_t \mathbf{1} + \theta_t$ and $q_t = \Pi_{\mathcal{K}}(k_t \mathbf{1} + \tilde{\theta}_t)$. Since isotonic regression satisfies the shift invariance $\Pi_{\mathcal{K}}(x + c\mathbf{1}) = \Pi_{\mathcal{K}}(x) + c\mathbf{1}$, the second definition can be rewritten as $q_t = \Pi_{\mathcal{K}}(\tilde{\theta}_t) + k_t \mathbf{1}$. Setting the two definitions equal to each other yields $\theta_t = \Pi_{\mathcal{K}}(\tilde{\theta}_t)$.

We start by showing $\tilde{\theta}_t^{\alpha_i} - \tilde{\theta}_t^{\alpha_{i+1}} \leq \eta$ for all $i = 1, 2, \dots, |\mathcal{A}| - 1$ and all times t by induction on t . The base case holds since Procedure 1 requires $\tilde{\theta}_1$ to be in \mathcal{K} . Now assume the statement holds through time t . Define $\Delta_i = \tilde{\theta}_t^{\alpha_{i+1}} - \tilde{\theta}_t^{\alpha_i}$, where $\Delta_t^i < 0$ means a crossing has occurred and $\Delta_t^i \geq 0$ means entries i and $i + 1$ of $\tilde{\theta}_t$ are ordered. Fix an i . We break into two cases:

- *Case 1: $\Delta_t^i < 0$, i.e., the entries were crossed at time t .* Since $\Delta_t^i < 0$, isotonic regression will pool entries i and $i + 1$ so that $q_t^{\alpha_i} = q_t^{\alpha_{i+1}}$ (Ayer et al., 1955), which implies $\text{cov}_t^{\alpha_i} = \text{cov}_t^{\alpha_{i+1}}$. Thus,

$$\Delta_{t+1}^i = \Delta_t^i - \eta[(\text{cov}_t^{\alpha_{i+1}} - \alpha_{i+1}) - (\text{cov}_t^{\alpha_i} - \alpha_i)] = \Delta_t^i + \eta(\alpha_{i+1} - \alpha_i) \geq \Delta_t^i \geq -\eta.$$

⁶Note that this procedure is equivalent to replacing Step 1 of Procedure 1 with $\theta_t = \Pi_{C_t}(\tilde{\theta}_t)$ for $C_t = \{x \in \mathbb{R}^{|\mathcal{A}|} \mid x_i + b_t^{\alpha_i} + \varepsilon \leq x_{i+1} + b_t^{\alpha_{i+1}} \text{ for } i = 1, 2, \dots, |\mathcal{A}| - 1\}$.

where the last inequality follows from the inductive hypothesis.

- *Case 2: $\Delta_t^i \geq 0$, i.e., the entries were ordered at time t .* Then the gradient update yields:

$$\Delta_{t+1}^i = \Delta_t^i - \eta[(\text{cov}_t^{\alpha_{i+1}} - \text{cov}_t^{\alpha_i}) - (\alpha_{i+1} - \alpha_i)].$$

Since the entries are ordered, $q_t^{\alpha_i} \leq q_t^{\alpha_{i+1}}$, which implies $\text{cov}_t^{\alpha_{i+1}} \geq \text{cov}_t^{\alpha_i}$. The indicator difference term is either 0 or 1. In the worst case (maximum decrease of Δ), the difference is 1. Thus:

$$\Delta_{t+1}^i \geq \Delta_t^i - \eta(1 - (\alpha_{i+1} - \alpha_i)).$$

Since $\Delta_t^i \geq 0$ and $(\alpha_{i+1} - \alpha_i) > 0$, it follows that $\Delta_{t+1}^i > -\eta$.

In both cases, $\Delta_{t+1}^i \geq -\eta$, which establishes the pairwise bound $\tilde{\theta}_{t+1}^{\alpha_i} - \tilde{\theta}_{t+1}^{\alpha_{i+1}} \leq \eta$.

Now, fix any $\tilde{\theta}_t$ satisfying $\tilde{\theta}_{t+1}^{\alpha_i} - \tilde{\theta}_{t+1}^{\alpha_{i+1}} \leq \eta$ for all i . Consider the ordered vector $\bar{\theta}_t$ obtained by iterating through the indices of $\tilde{\theta}_t$ and, whenever an unordered entry is encountered, setting its value equal to that of the previous index — that is, set $\bar{\theta}_t^{\alpha_1} = \tilde{\theta}_t^{\alpha_1}$, and for $i = 2, 3, \dots, |\mathcal{A}| - 1$, if $\tilde{\theta}_t^{\alpha_i} < \bar{\theta}_t^{\alpha_{i-1}}$, set $\bar{\theta}_t^{\alpha_i} = \bar{\theta}_t^{\alpha_{i-1}}$. Otherwise, set $\bar{\theta}_t^{\alpha_i} = \tilde{\theta}_t^{\alpha_i}$. Since $\bar{\theta}_t \in \mathcal{K}$, we have

$$\|\tilde{\theta}_t - \Pi_{\mathcal{K}}(\tilde{\theta}_t)\|_2 \leq \|\tilde{\theta}_t - \bar{\theta}_t\|_2.$$

Observe that $\tilde{\theta}_t^{\alpha_1} - \bar{\theta}_t^{\alpha_1} = 0$ and, for $i = 2, 3, \dots, |\mathcal{A}|$, $\tilde{\theta}_t^{\alpha_i} - \bar{\theta}_t^{\alpha_i} \leq \theta_t^{\alpha_{i-1}} - \bar{\theta}_t^{\alpha_{i-1}} + \eta$ by the pairwise bound shown above. Thus, we have $\tilde{\theta}_t^{\alpha_i} - \bar{\theta}_t^{\alpha_i} \leq \eta(i-1)$, so

$$\|\tilde{\theta}_t - \Pi_{\mathcal{K}}(\tilde{\theta}_t)\|_2 \leq \sqrt{\sum_{i=1}^{|\mathcal{A}|} (\eta(i-1))^2} = \eta \sqrt{\sum_{i=1}^{|\mathcal{A}|} (i-1)^2} = \eta \sqrt{\frac{|\mathcal{A}|(|\mathcal{A}|-1)(2|\mathcal{A}|-1)}{6}} \leq \frac{\eta |\mathcal{A}|^{3/2}}{\sqrt{3}}.$$

Since every hidden iterate $\tilde{\theta}_t$ satisfies the pairwise constraint and any vector satisfying this constraint has a distance of at most $\frac{\eta |\mathcal{A}|^{3/2}}{\sqrt{3}}$ to the ordered cone, we conclude that $\|\theta_t - \tilde{\theta}_t\|_2 \leq \frac{\eta |\mathcal{A}|^{3/2}}{\sqrt{3}}$ for all t . \square

Proof of Proposition 10 (GEQ of lazy gradient descent under bounded projection distance). For convenience, redefine $h_t = \max(\|\tilde{\theta}_1\|_2, h_t)$ and let $h_0 = \|\tilde{\theta}_1\|_2$. We will use induction to show $\|\tilde{\theta}_{T+1}\|_2 \leq h_T + B + \eta L$ for all $T \geq 0$, similar to the proof of Proposition 6 in Angelopoulos et al. (2025). The base case of $T = 0$ is trivially true. Now, for the inductive step, assume the inequality holds up through T . We split into two cases. First, if $\|\tilde{\theta}_T\|_2 \leq h_T + B$, then by the triangle inequality we have

$$\begin{aligned} \|\tilde{\theta}_{T+1}\|_2 &\leq \|\tilde{\theta}_T\|_2 + \eta \|g_t(\theta_t)\|_2 \\ &\leq h_T + B + \eta L, \end{aligned}$$

where the second inequality invokes the Lipschitzness of the loss function. Second, if $\|\tilde{\theta}_T\|_2 > h_T + B$, observe that

$$\begin{aligned} \|\tilde{\theta}_{T+1}\|_2^2 &= \|\tilde{\theta}_T\|_2^2 + \eta^2 \|g_T(\theta_T)\|_2^2 - 2\eta \langle \tilde{\theta}_T, g_T(\theta_T) \rangle \\ &\leq \|\tilde{\theta}_T\|_2^2 + \eta^2 L^2 - 2\eta \langle \tilde{\theta}_T, g_T(\theta_T) \rangle \\ &\leq \|\tilde{\theta}_T\|_2^2 + \eta^2 L^2 - 2\eta \phi_T(\theta_T) \\ &\leq \|\tilde{\theta}_T\|_2^2 \\ &\leq (h_T + B + \eta L)^2 \\ &\leq (h_{T+1} + B + \eta L)^2 \end{aligned}$$

where second line applies Lipschitzness, the third applies Lemma 7 below (which makes use of restorativity, inward flow, and the bounded distance between $\tilde{\theta}_t$ and θ_t), the fourth applies the assumed condition on $\phi_T(\tilde{\theta}_T)$, the fifth applies the inductive hypothesis, and the sixth uses the increasing property of h_t . Taking the square root concludes the inductive step. To get (32), plug this bound into Proposition 11 with $D = 0$. \square

We note that this proof procedure can be used to prove a similar result for lazy gradient descent with delay $D \geq 0$, but we have focused on the $D = 0$ case for simplicity. We now prove Lemma 7, which was a key component of the proof above.

Lemma 7. *Consider a loss ℓ (with gradient g) and closed convex set $C \subseteq \mathbb{R}^m$ such that the loss is (h, ϕ) -restorative and (ℓ, C) satisfy inward flow. If $\|\Pi_C(\tilde{\theta}) - \tilde{\theta}\|_2 \leq B$, then*

$$\langle \tilde{\theta}, g(\Pi_C(\tilde{\theta})) \rangle \geq \phi(\Pi_C(\tilde{\theta})) \quad \text{whenever } \|\tilde{\theta}\|_2 > h + B.$$

Proof. Consider any $\tilde{\theta}$ such that $\|\tilde{\theta}\|_2 > h + B$. Define $\theta = \Pi_C(\tilde{\theta})$. By the triangle inequality,

$$\|\theta\|_2 > \|\tilde{\theta}\|_2 - \|\theta - \tilde{\theta}\|_2 \geq h + B - B = h.$$

Combining this with the restorativity of ℓ , this tells us $\langle \theta, g(\theta) \rangle \geq \phi(\theta)$. Applying Lemma 4 then gives the desired result. \square

Proof of Corollary 1 (Calibration rate for MultiQT with point forecasts). From Lemma 1, we know that the MultiQT loss is $(h, \frac{hd_{\mathcal{A}}}{\sqrt{|\mathcal{A}|}} - R|\mathcal{A}|)$ -restorative. In order to satisfy the condition on ϕ that appears in Proposition 10, we need $\frac{hd_{\mathcal{A}}}{\sqrt{|\mathcal{A}|}} - R|\mathcal{A}| \geq \frac{\eta|\mathcal{A}|}{2}$, so we must choose $h \geq \frac{\sqrt{|\mathcal{A}|}}{d_{\mathcal{A}}} (\frac{\eta|\mathcal{A}|}{2} + R|\mathcal{A}|) = \frac{\eta|\mathcal{A}|^{3/2}}{2d_{\mathcal{A}}} + \frac{R|\mathcal{A}|^{3/2}}{d_{\mathcal{A}}}$. We then apply Proposition 10 with this (h, ϕ) , Lipschitz constant $L = |\mathcal{A}|$, and $B = \frac{\eta|\mathcal{A}|^{3/2}}{\sqrt{3}}$. This yields a bound on the ℓ_2 -norm of the average gradients. To obtain the calibration error bound for each individual quantile level, we use the fact that for any vector $x = [x_1, x_2, \dots, x_m]$, we have $|x_i| \leq \|x\|_2$ for all $i = 1, 2, \dots, m$. \square

E Additional Experimental Results

In this section, we provide supplementary empirical results that further illustrate the behavior of MultiQT across our forecasting tasks. First, we repeat the main experiments using PIT entropy as an alternative calibration metric, showing that our conclusions are robust to this choice (Section E.1). We then present additional case studies for COVID-19 death forecasting (Section E.2) and energy forecasting (Section E.3), including comprehensive calibration curves and detailed forecast visualizations, which confirm that MultiQT consistently improves calibration.

E.1 Results using PIT entropy

In Section 5, we used the average calibration error as the calibration metric. However, this is not the only way to quantify the calibration performance of quantile forecasts. Another metric is the PIT entropy (Gneiting et al., 2007; Rumack et al., 2022), which makes use of the fact that quantile forecasts can be interpolated to specify a distributional forecast for y_t . This metric is appropriate for evaluation in settings where the levels in \mathcal{A} are numerous and well dispersed across $[0, 1]$, as is the case in our experimental settings, but is less appropriate for sparse \mathcal{A} (e.g., if $\mathcal{A} = \{0.5, 0.9\}$, interpolation seems less appropriate).

Computing the PIT entropy. The *PIT entropy* refers to the entropy of the distribution of the probability integral transform (PIT) values. Here, we describe how to compute the PIT entropy given a sequence of quantile forecasts q_1, q_2, \dots, q_T and the corresponding true values y_1, y_2, \dots, y_T , where $q_t = (q_t^{\alpha_1}, q_t^{\alpha_2}, \dots, q_t^{\alpha_m})$ is the quantile forecast at time t for quantiles $\alpha_1 < \alpha_2 < \dots < \alpha_m$

Step 1: Convert quantile forecasts into a cumulative density function. We must first convert the quantile forecasts into a distributional forecast. Specifically, we want to define the cdf $F_t(y)$ for all $y \in \mathbb{R}$. The mapping from quantiles to distribution is one to many, and our procedure for selecting a distribution from the set of possibilities follows the procedure used in Appendix A.1 of [Buchweitz et al. \(2025\)](#). This can be summarized as linear interpolation for intermediate values combined with exponential tails for values outside the forecast range.

- If there exists $i \in [|\mathcal{A}|]$ such that $y \in [q_t^{\alpha_i}, q_t^{\alpha_{i+1}}]$, then $F_t(y) = \alpha_i + \frac{y - q_t^{\alpha_i}}{q_t^{\alpha_{i+1}} - q_t^{\alpha_i}}(\alpha_{i+1} - \alpha_i)$.
 - When ties occur (i.e., $q_t^{\alpha_{i+1}} = q_t^{\alpha_i}$), the interior slope on that segment is undefined so when y equals a tied forecast value, we set $F_t(y)$ to be the largest quantile level in the tied block. Formally, $F_t(y) = \alpha^{i_{\max}}$ where $i_{\max} = \max\{i : q_t^{\alpha_i} = y\}$.
- If no such i exists (so $y < q_t^{\alpha_1}$ or $y > q_t^{\alpha_{|\mathcal{A}|}}$), we attach exponential tails, chosen so that the density at the boundary matches the nearest interior segment.
 - For $y < q_t^{\alpha_1}$, we first find the smallest i such that $q_{i+1} \neq q_i$ and compute the density $\rho = \frac{\alpha_{i+1} - \alpha_i}{q_{i+1} - q_i}$. Define $\lambda = \frac{\rho}{\alpha_1}$. We then let $F_t(y) = \alpha_1 e^{\lambda(y - q_t^{\alpha_1})}$.
 - For $y > q_t^{\alpha_{|\mathcal{A}|}}$, we find the largest i such that $q_{i+1} \neq q_i$ and compute the density $\rho = \frac{\alpha_{i+1} - \alpha_i}{q_{i+1} - q_i}$. Define $\lambda = \frac{\rho}{1 - \alpha_{|\mathcal{A}|}}$. We then let $F_t(y) = 1 - (1 - \alpha_{|\mathcal{A}|}) e^{-\lambda(y - q_t^{\alpha_{|\mathcal{A}|}})}$.

Step 2: Compute the PIT values and their entropy. Apply the cdf's F_t from the previous step to get the PIT values $U_t = F_t(y_t)$ for $t = 1, 2, \dots, T$. Put these into $m = 10$ equal-width bins on $[0, 1]$. Let \hat{p}_i be the empirical frequencies for bin i . We compute the normalized Shannon entropy as

$$\hat{H} = - \sum_{i=1}^m \hat{p}_i \log \hat{p}_i / \log m,$$

where the division by $\log m$ ensures \hat{H} lies in $[0, 1]$. Under perfect calibration, the PIT values should be distributed uniformly on $[0, 1]$, which has maximal entropy. Thus, a \hat{H} near one indicates good calibration, while a value near zero indicates poor calibration.

We now reproduce the main figures from Section 5 with PIT entropy in place of average calibration error. Figure 12 is the analogue of Figure 5. Figure 13 is the analogue of Figure 7. The results are qualitatively similar to the results using average calibration error — MultiQT results in strong improvements in calibration.

E.2 Additional COVID-19 forecasting results

In Figure 4 of the main paper, we showed the effect of MultiQT on the calibration of COVID-19 death forecasts at the one-week-ahead forecasting horizon. Now, we provide the same type of calibration plots for *all* forecasting horizons (one, two, three, and four weeks ahead) in Figure 14. We observe that MultiQT consistently improves calibration across all forecasting horizons.

Figures 15 - 18 visualize individual COVID-19 death forecasts before and after applying MultiQT, similar to Figure 1 in the main text. To provide a sense of the effect of MultiQT on forecasts for both states with

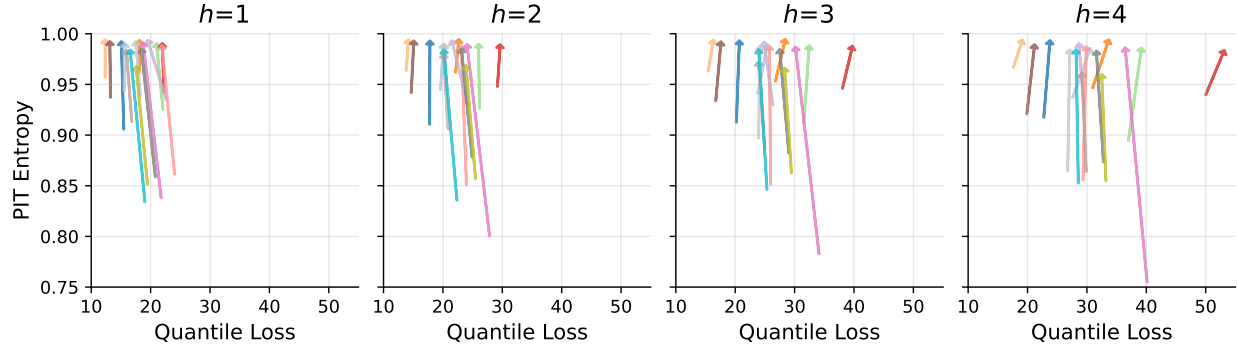


Figure 12: Average quantile loss and PIT entropy for raw forecasts (**tail** of arrow) and MultiQT forecasts (**head** of arrow) for h -week-ahead COVID-19 death forecasts, where $h \in \{1, 2, 3, 4\}$. Each color represents a forecaster, and the coordinates of the head and tail are determined by averaging metrics across all 50 states for the specified horizon. For quantile loss, lower is better. For PIT entropy, higher is better.

large populations and small populations, the first pair of figures (Figures 15 and 16) illustrate the effect of using MultiQT to correct one-week-ahead forecasts of COVID deaths in (the large state) California for each of the 15 COVID-19 forecasting teams; the second pair of figures (Figures 17 and 18) show the same for (the small state) Vermont. Forecasts are made at levels 0.01, 0.025, 0.05, 0.1, 0.15, 0.2, 0.25, 0.3, 0.35, 0.4, 0.45, 0.5, 0.55, 0.6, 0.65, 0.7, 0.75, 0.8, 0.85, 0.9, 0.95, 0.975, and 0.99. To visualize these forecasts, we plot colored bands where the lightest opacity connects the 0.01 and 0.99 level forecasts, the next lightest connects the 0.025 and 0.975 level forecasts, and so on. We can also use the visualized forecasts to inspect the calibration — if the 0.01 and 0.99 level quantile forecasts are calibrated, we should see that the true value (black line) falls in the lightest opacity band 98% of the time. Zooming in on the raw forecasts, we see that this is not the case for many of the forecasters initially, but after applying MultiQT the coverage of the extreme quantiles is much improved.

E.3 Additional energy forecasting results

To complement Figure 6 in the main paper, which shows calibration curves for daily energy forecasts at 10:00 a.m. CST, we provide the same plots for 2:00 a.m., 6:00 a.m., 2:00 p.m., 6:00 p.m., and 10:00 p.m. in Figure 19 (wind energy) and Figure 20 (solar energy). MultiQT produces near-perfect calibration for all hours. We remark that, in practice, it is unnecessary to generate solar energy forecasts for 2:00 a.m. and 10:00 p.m. At these nighttime hours, the solar energy production is always zero, and the raw quantile forecasts are also zero for all levels. Forecasting is not necessary when the outcomes are deterministic, and domain knowledge can be used to identify such cases. Figures 21 and 22 visualize the forecasts before and after applying MultiQT for 10:00 a.m. CST for eight randomly sampled wind and solar farm sites.

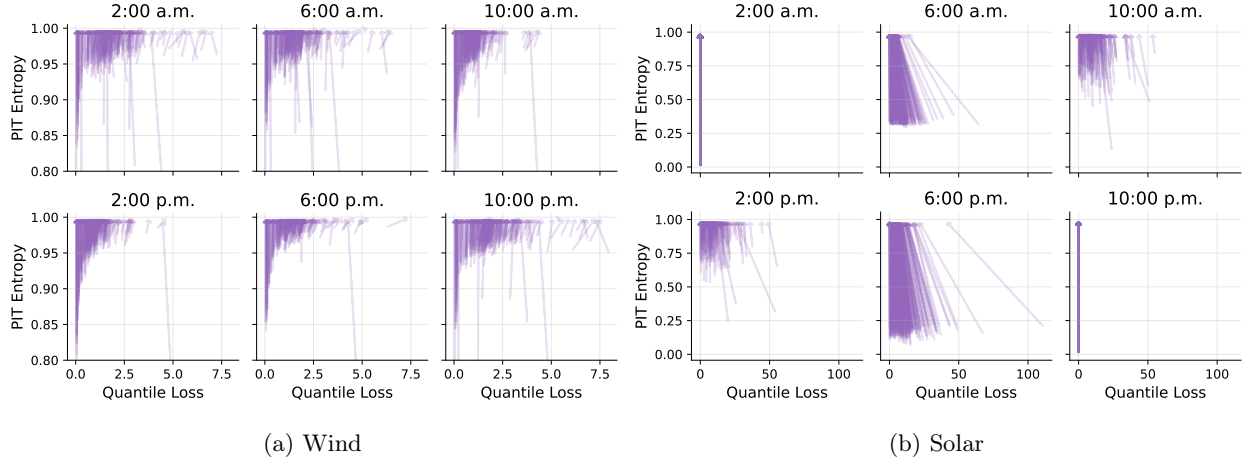


Figure 13: Average quantile score and PIT entropy for raw forecasts (**tail** of arrow) and MultiQT forecasts (**head** of arrow) for day-ahead wind and solar energy production at 2:00 a.m., 6:00 a.m., 10:00 a.m., 2:00 p.m., 6:00 p.m., and 10:00 p.m. CST. Each arrow corresponds to a wind or solar energy site. For average quantile score, lower is better. For PIT entropy, higher is better.

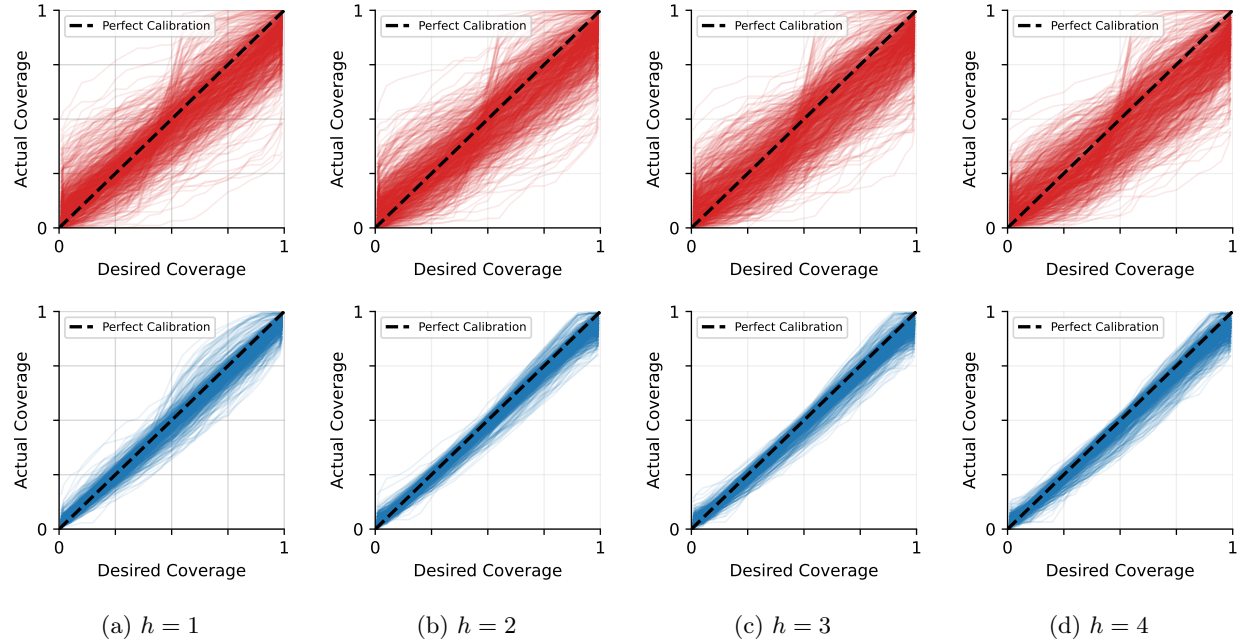


Figure 14: Actual coverage vs. desired coverage at each quantile level for h -week-ahead COVID-19 death forecasts before (red) and after (blue) applying MultiQT, where $h \in \{1, 2, 3, 4\}$. Each forecaster \times state combination is a line.

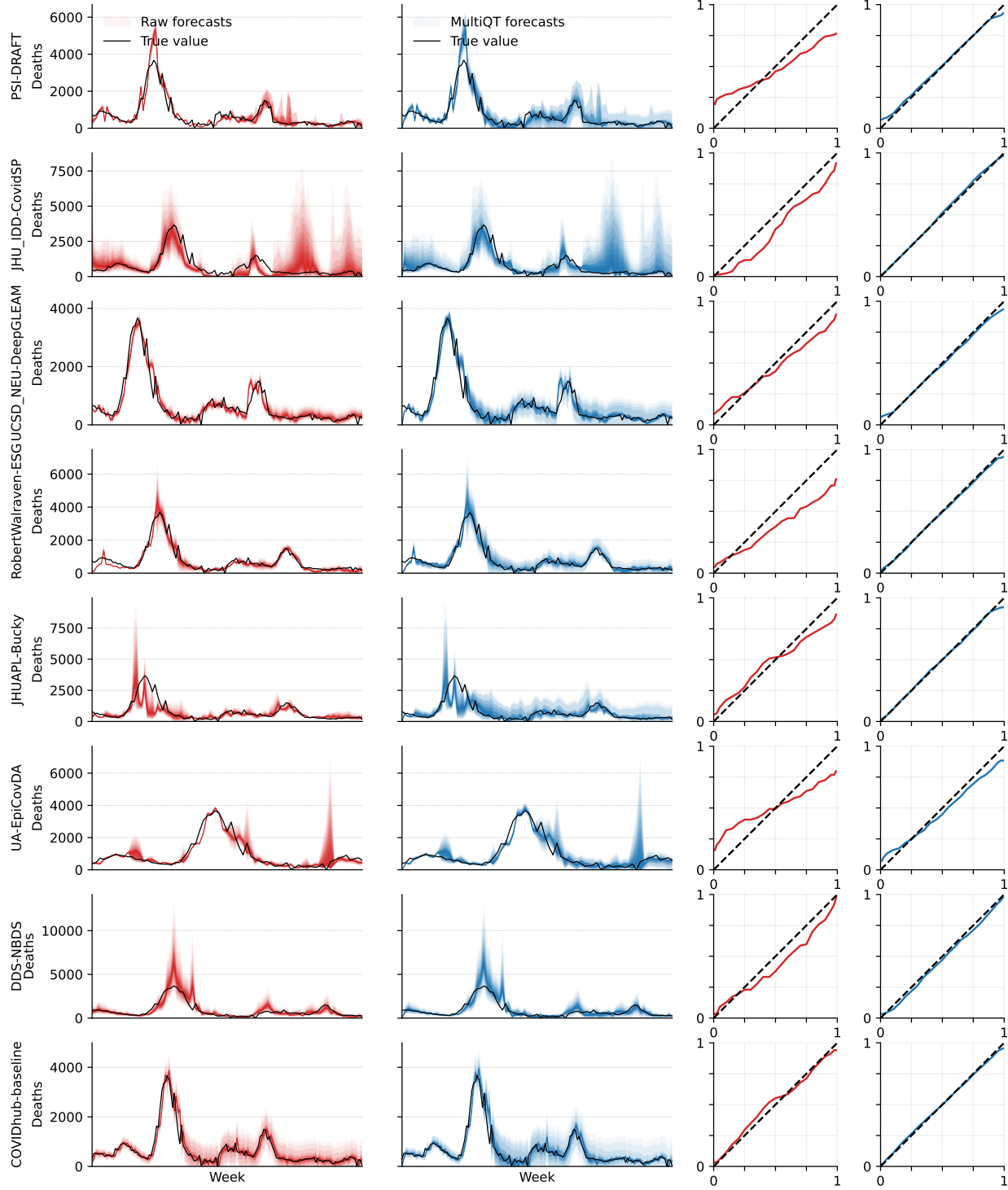


Figure 15: **(Part 1 of 2)** One-week-ahead forecasts of weekly COVID-19 deaths in **California** by each forecaster for the weeks for which forecasts are submitted by the forecaster. Note that the date range varies for each forecaster. The name of the forecaster is provided on the left side of each row. The first column shows the raw forecasts, the second column shows the forecasts after applying MultiQT, the third column shows actual coverage vs. desired coverage of the raw forecasts, and the fourth column shows the same for the MultiQT forecasts.

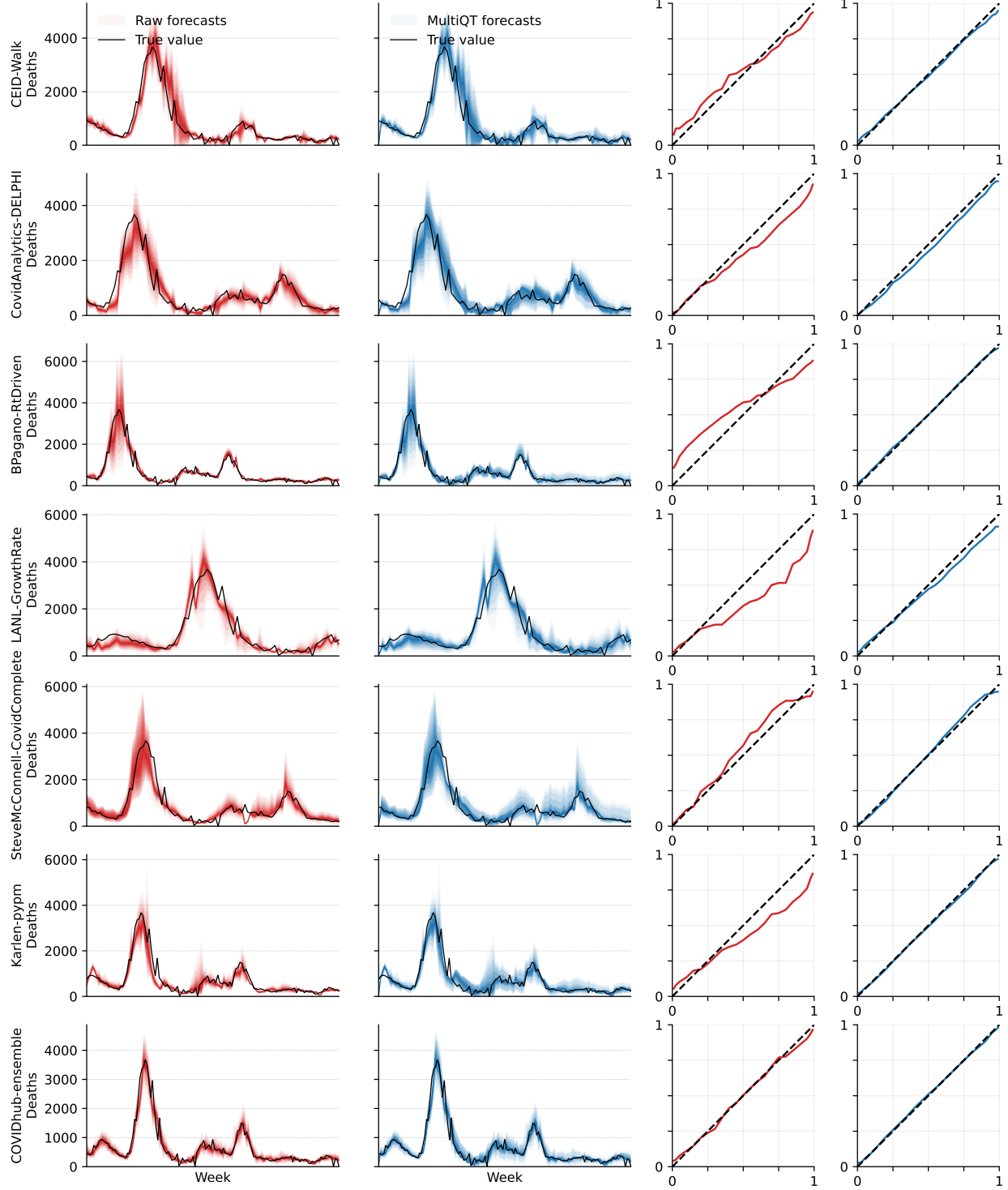


Figure 16: **(Part 2 of 2)** One-week ahead forecasts of weekly COVID-19 deaths in **California** for the weeks for which forecasts are submitted by the forecaster. Note that the date range varies for each forecaster. The name of the forecaster is provided on the left side of each row. The first column shows the raw forecasts, the second column shows the forecasts after applying MultiQT, the third column shows actual coverage vs. desired coverage of the raw forecasts, and the fourth column shows the same for the MultiQT forecasts.

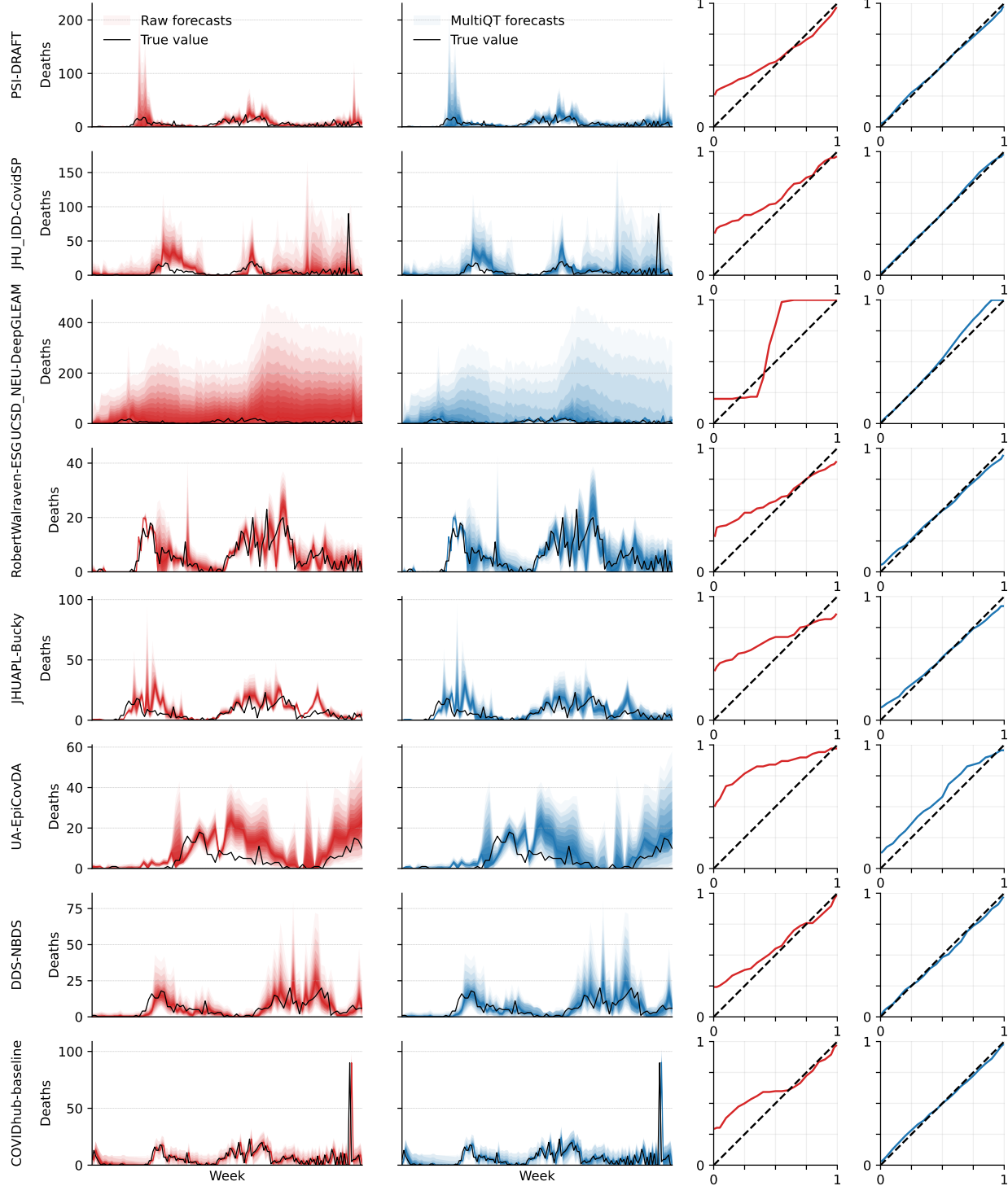


Figure 17: **(Part 1 of 2)** One-week ahead forecasts of weekly COVID-19 deaths in **Vermont** for the weeks for which forecasts are submitted by the forecaster. Note that the date range varies for each forecaster. The name of the forecaster is provided on the left side of each row. The first column shows the raw forecasts, the second column shows the forecasts after applying MultiQT, the third column shows actual coverage vs. desired coverage of the raw forecasts, and the fourth column shows the same for the MultiQT forecasts.

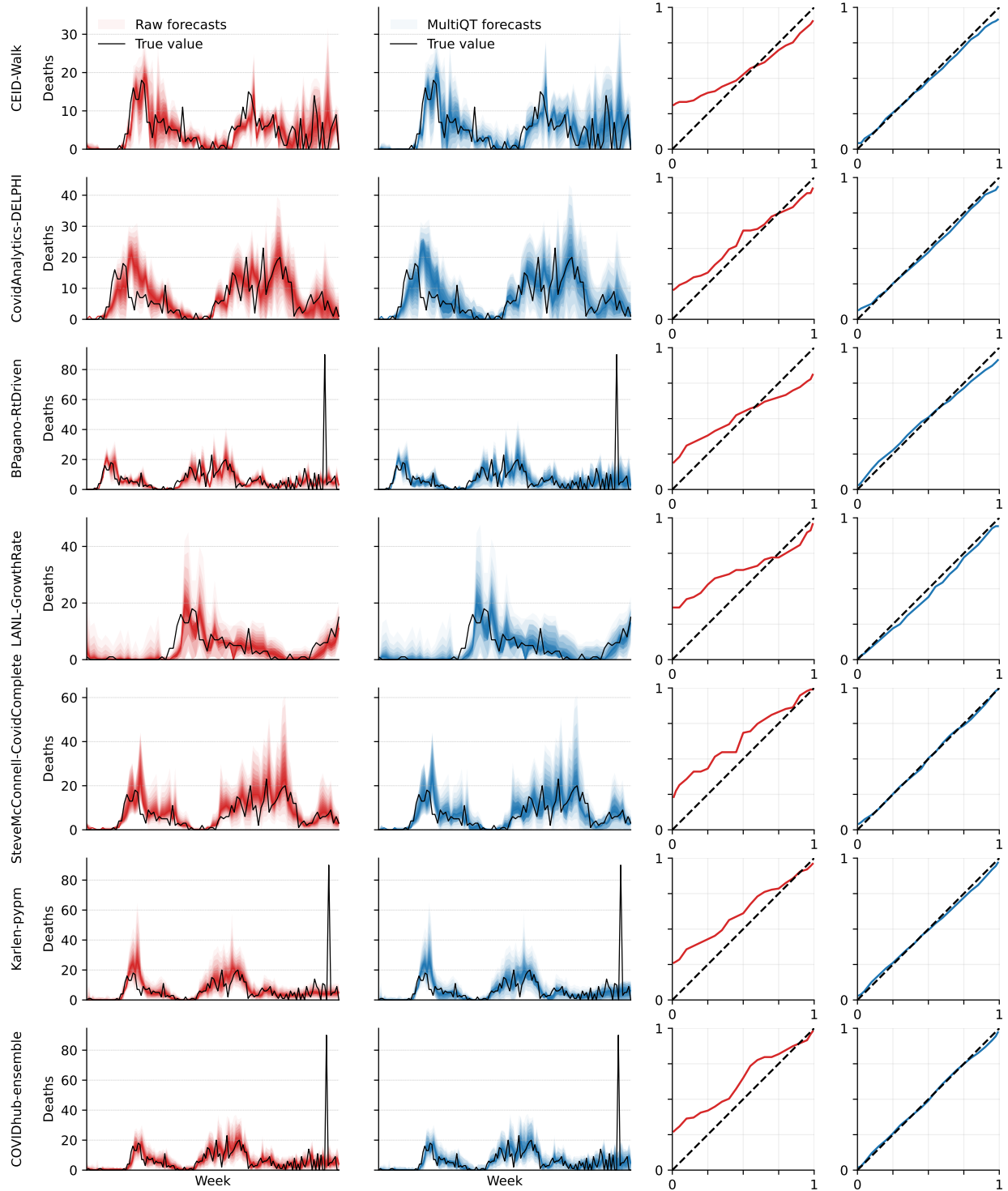


Figure 18: **(Part 2 of 2)** One-week ahead forecasts of weekly COVID-19 deaths in **Vermont** for the weeks for which forecasts are submitted by the forecaster. Note that the date range varies for each forecaster. The name of the forecaster is provided on the left side of each row. The first column shows the raw forecasts, the second column shows the forecasts after applying MultiQT, the third column shows actual coverage vs. desired coverage of the raw forecasts, and the fourth column shows the same for the MultiQT forecasts.

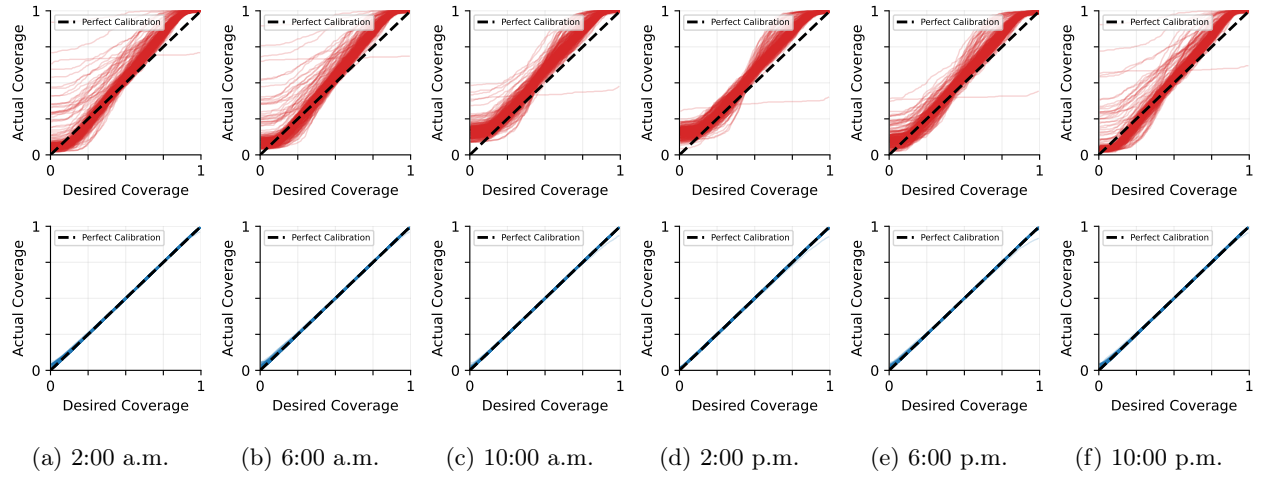


Figure 19: Actual coverage vs. desired coverage at each quantile level of day-ahead raw forecasts (red) and MultiQT-calibrated forecasts (blue) for **wind** energy production at 2:00 a.m., 6:00 a.m., 10:00 a.m., 2:00 p.m., 6:00 p.m., and 10:00 p.m.

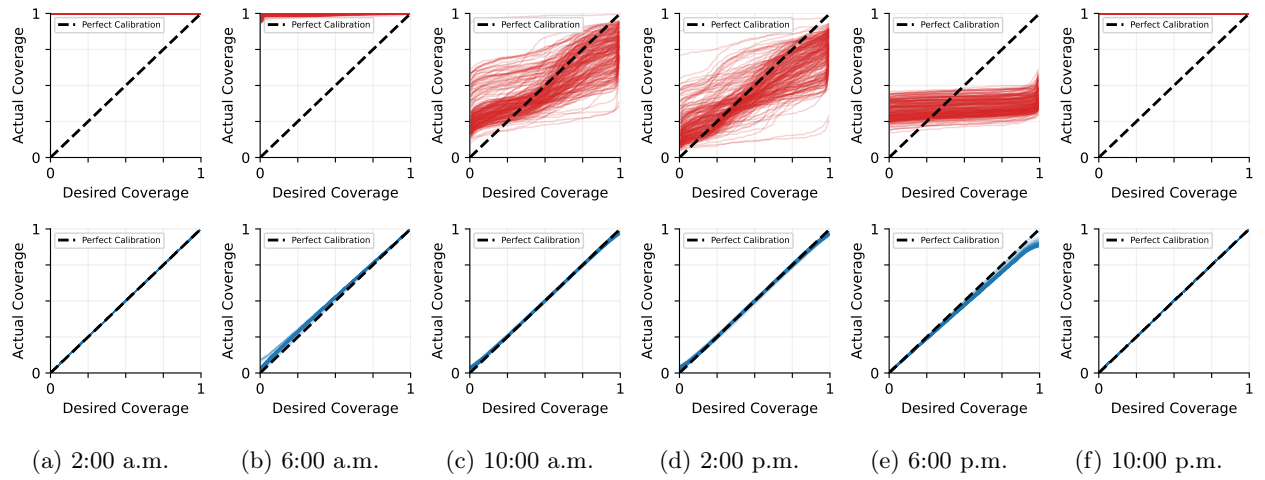


Figure 20: Actual coverage vs. desired coverage at each quantile level of day-ahead raw forecasts (red) and MultiQT-calibrated forecasts (blue) for **solar** energy production at 2:00 a.m., 6:00 a.m., 10:00 a.m., 2:00 p.m., 6:00 p.m., and 10:00 p.m.

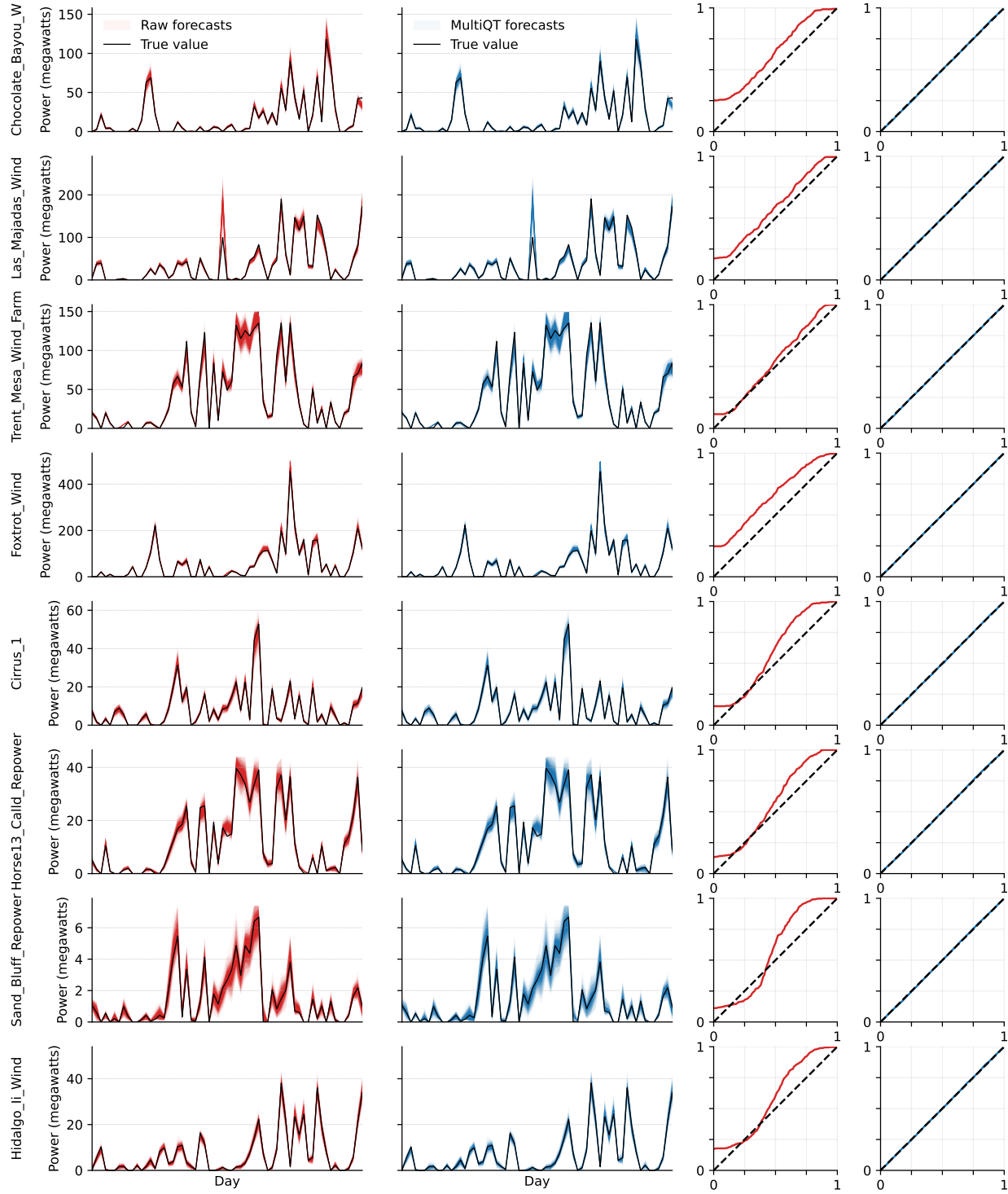


Figure 21: Day-ahead **wind** energy forecasts for 10:00 a.m. CST at eight randomly sampled wind farm sites. The name of the site is provided on the left side of each row. The first column shows the raw forecasts, the second column shows the forecasts after applying MultiQT, the third column shows actual coverage vs. desired coverage of the raw forecasts, and the fourth column shows the same for the MultiQT forecasts. For viewability, forecasts are shown only for September 1, 2018 to October 31, 2018, but calibration is computed using forecasts for every day in 2018.

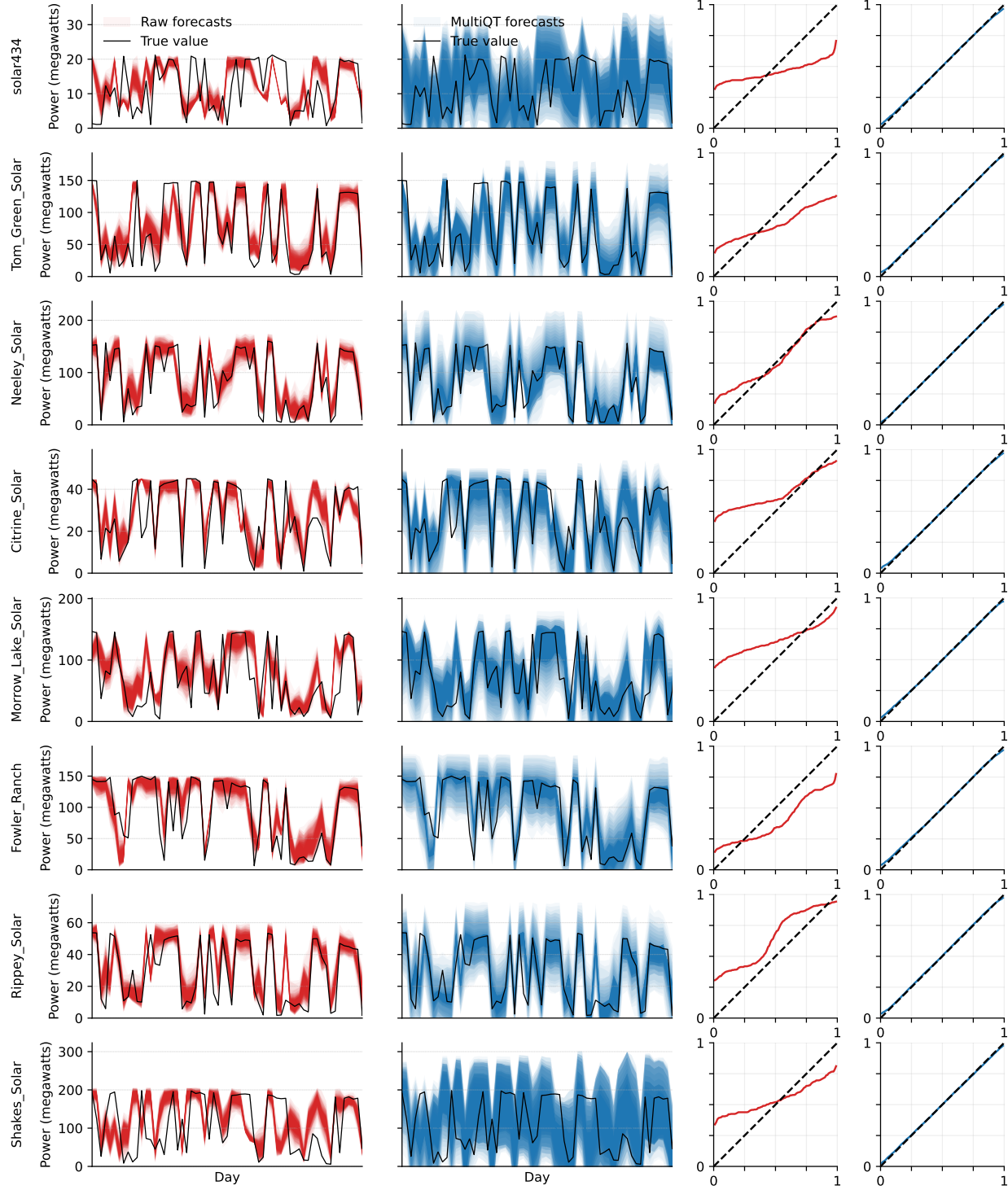


Figure 22: Day-ahead **solar** energy forecasts for 10:00 a.m. CST at eight randomly sampled solar farm sites. The name of the site is provided on the left side of each row. The first column shows the raw forecasts, the second column shows the forecasts after applying MultiQT, the third column shows actual coverage vs. desired coverage of the raw forecasts, and the fourth column shows the same for the MultiQT forecasts. For viewability, forecasts are shown only for September 1, 2018 to October 31, 2018, but calibration is computed using forecasts for every day in 2018.